Surface Acoustic Wave Controlled Semiconductor Optical Source

Meng, Qingbin

Award date:
2009

Awarding institution:
University of Bath

University of Bath

Department of Electronic and Electrical Engineering

Surface Acoustic Wave Controlled Semiconductor Optical Source

by

MENG Qingbin

Thesis for the degree of Doctor of Philosophy

October 2009

Acknowledgements

I would like to express my sincere gratitude to my advisor Dr J. Sarma and Dr F. Causa for the continuous support of my PhD study and research, for their patience, motivation, enthusiasm, and immense knowledge. Their guidance helped me in all the time of research and writing of this thesis. I could not have imagined having a better advisor and mentor for my PhD study.

I thank all my officemates, for their kind help, warm support, and valuable discussion in life and in academic. I will never forget in those days and nights, the sleepless nights we were working together, the stories we share with each other and the fun we have had.

I have also benefited a lot from my colleague Mr Wu. I would like to thank him for his heuristic discussion with me about grating optics. Without his help it would last long before I could have a feeling about my project.

I thank my love, my wife Ms YU Shunda. Without her encouragement, her care of our life and her talent of time managements, it was impossible for me to finish my study.

I thank my family: my parents Mr Meng Yantang and Mrs Lu Lianfeng for giving birth to me and supporting me spiritually throughout my life, and my sister Meng Jing, for understanding and sharing with her heart.

Abstract

A semiconductor optical source monolithically integrated with a surface acoustic wave (SAW) Bragg-cell to operate as a functional device is proposed in this thesis. The practical structure of such an integrated device is demonstrated and design guidelines are presented. Compared with conventional optical beam processed devices, this functional integrated semiconductor optical source (FISOS) is revised to be compact in size, flexible in function and potentially robust in performance.

The FISOS is analyzed as two sub-divisions, optical source and acoustic processor, which have the common substrate structure. The optical beams excited from the optical source part of the device undergoes a scattering in the Bragg grating formed by SAWs that are generated by an IDT positioned on top of the acoustic processing part of device. By altering the property (power, frequency, etc.) of the SAW, versatile functionalities such as modulation, filtering, beam steering and so on of the optical beams can be realized in this optical source device.

A multilayer structure based on GaN/InGaN MQWs grown on sapphire is designed for the FISOS to be blue light emitting and efficiently launching SAWs. An etch-down technique employed in the SAW processing part is taken to improve the overlap between the optical and acoustic waves and then the interaction efficiency. Optimizations to the geometrical dimensions of the FISOS, such the width of the ridge waveguide, the position of the IDT and the etching depth, etc., are discussed in the given structure.

Numerical models are investigated to access the operational characteristics and then to provide design guidelines for the proposed integrated device. The Bragg diffraction of optical waves occurring within the acoustic waves in the proposed structure are simulated as a two-dimensional interaction between two guided optical modes and an acoustic surface wave.

The modal distributions and propagation velocities of SAWs in a multilayer system are calculated using Adler's matrix method. The electrical characteristics of an IDT, such as impedance, insertion loss, electromechanical constant and so on are also discussed.

Transverse and lateral optical modes in the given multilayer structure are analyzed by the transfer matrix method. The interaction of optical waves and acoustic waves are modeled using the rigorous grating diffraction theory. Starting from Floquet's theory, the well-known coupled-wave method and modal method can both be derived from the rigorous grating diffraction theory. Discussions of some useful approximate methods are also presented. In this thesis, the simulations of the acoustooptic interaction are performed using the coupled-wave method.

From the simulation results, the angular distribution profile and spatial profile of the output of the FISOS are evaluated. An improvement to the expression of the diffraction efficiency in such an integrated device is proposed. The so-called beam diffraction efficiency gives a more complete measure to the acoustooptic diffraction and is used to investigate the features of FISOS different from conventional acoustooptic devices. Contour plots of the beam efficiency varying with acoustic frequency and power in a FISOS is demonstrated to be a convenient and powerful approach in the device design.

The operational performances of an integrated deflector and a modulator in FISOS are analyzed to investigate the feasibility of FISOS. The trade-off of the efficiency-resolution in an integrated deflector design is discussed. Short interaction length, high acoustic frequency and narrow ridge are proved to be helpful for a larger number of resolvable spots with a fairly high efficiency. In the case of the integrated modulator, given that the figure of merit Q is fixed, it is demonstrated that the smaller the Q, the longer the interaction length, larger ridge width and lower acoustic frequency will give rise to a larger bandwidth, though the highest efficiency might appear at a higher frequency.

Some practical issues such as the misalignment of planar elements on the device and the incoherence of the integrated optical source are also discussed. A modified working frequency can be used to compensate the efficiency loss in the former case; in the latter case, it is demonstrated that a distortion of beam diffraction efficiency versus acoustic power with an incoherent optical source arises due to the wide spectrum of the incident optical waves.

Contents

List of Figures

List of Tables

Chapter 1

Introduction

Although there are always advances and improvements to be made, it is perhaps not unreasonable to say that the design and fabrication procedures for conventional semiconductor optical sources such as LED (Light Emitting Diode) and laser have been well established. Indeed, it is for just that reason that attention has now been directed to designing semiconductor sources with functional properties such as modulation, switching, routing, filtering and beam scanning etc. The objectives of investigations of this project are to develop the theoretical bases and technical procedures for designing one such function integrated semiconductor optical source (FISOS).

One of the basic requirements for FISOS devices is to be able to alter the material properties, for instance, the permittivity. Predominantly, it is the change in permittivity of the material that is used to desirably affect the optical characteristics. A traditional mechanism for achieving that is to inject carriers into the material. Whereas this is quite an effective method it tends to be relatively slow (governed largely by spontaneous recombination rates) and spatial definitions limited by diffusion coefficients. Also, the fabricated structure determines and fixes the limited range of the functional operation so that tunability may not be readily possible. Whereas electrooptic control of the material may provide somewhat better prospects the general limitations still persist.

The mechanism of acoustooptic (AO) interaction is considered in this project as an alternative procedure which, in principle, provides for faster operation, finer spatial delineation and the capacity to alter controlling dimensions. The AO interaction for altering the material characteristic has been utilized by other researchers

as a separate discrete device to operate on optical signals. Particularly, as a part of hybrid active devices, it has been used as deflector, modulator, tunable filter, Q-switch and mode-locker, etc. The main interest in this project, however, is to monolithically integrate the optical source and the optical functional element. In this context, a common material structure will be utilized for both the semiconductor optical source and the AO functional processor. The design considerations are to be proposed and the feasibility of the integrated device is to be evaluated. Compared with a conventional optical source, the FISOS is expected to achieve an enhancement of robustness, an expansion of function and a simplification of assembly and packaging.

1.1 Integrated Device

An optical integrated circuit (OIC) is a thin-film-type optical circuit, in which the signal is carried by means of a beam of light rather than by an electrical current, and the various circuit elements, such as a laser LED or laser, some functional components like switches or modulators, and photo diodes as detectors, are interconnected on the substrate wafer by optical waveguides.

History of OIC The concept of an OIC emerged in 1960s when the development of the laser first provided a stable source of coherent light for such device, and was firstly proposed by Miller in Bell Laboratory, [1]. During the later years in 1970s, several factors combined to bring integrated optics out of the laboratory and into practical applications, such as the low-loss optical fibers [2], the creation of reliable CW GaAs laser diodes [3], and the realization of photolithographic microfabrication techniques capable of submicron linewidth. In the 1980s, optical fibers largely replaced metallic wires in telecommunications such as PC networks, [4][5]. Since 1990s, the incorporation of optical fibers and OIC into telecommunications, data-storage and data-transmission networks has been extended in many systems [6]∼[8].

In fact, the history of OIC can be divided into three generations. The first generation is concerned with conventional optics, in which optical systems are set up by arranging bulk-type optical components on large optical benches. The second generation is called microoptics and microoptical components such as LED, laser,

fiber and rod lenses are introduced into the system and assembled. Although performance of those discrete systems can be satisfactory, problems occur in the assembly and optical alignment of the components. OICs are optical devices in the third generation with features as followed:

- Features based on wave optics. Devices consist mainly of single-mode waveguides. That is, optical devices of the first and second generations can be treated by ray optics, but the device of the third generation has to be treated by wave optics.

- Stable alignment by integration. No assembly problem exists for OIC since the discrete elements have been integrated on a single substrate. The device can therefore withstand vibration and temperature changes.

- Low operating voltage and short interaction length. Benefited by the reduced size of the system, low operating voltage is possible. Also interaction increases and the interaction length becomes shorter.

- Larger optical power density. Optical power density is extremely large in waveguides compared with that of optical beams in a free space. Optical nonlinear effects therefore can be utilized.

- Low price. The development of integration techniques has made mass production possible, and has reduced the amount of materials needed.

Types of OICs: hybrid and monolithic system There are two forms of optical integrated circuits. One of them is called monolithic OIC, in which a single substrate is used for all involved elements, such as sources, waveguides and detectors. The other is called hybrid OIC, in which somehow two or more substrate materials are bonded together to optimize performance for different elements, such as GaAs for a laser and Si for circuitry.

The major advantage of the hybrid approach is that the OIC can be fabricated using existing technology, piecing together devices which have been substantially optimized in a given material. The most appropriate materials and processing techniques currently available can be utilized. The design and fabrication is thus relatively easy.

Although the monolithic system is ideal as an OIC, since a source of light is required, it can only be fabricated in optically active materials, of which the choices are quite limited. Besides, for hybrid circuits the bonds holding the various elements together are subject to misalignment, or even failure due to vibration and thermal expansion. In addition the monolithic approach is ultimately cheaper if mass production of the circuit is desired, because automated batch processing can be used. For these reasons monolithic OIC is likely to become the most common type in use once the technology has matured.

Materials For hybrid OIC, $LiNbO_3$ is a typical material used even in commercial areas. A variety of OICs have been investigated, such as electrooptic modulators, Mach-Zehnder interferometric modulators, acoustooptic filters and optical amplifiers, [9][10]. These OICs take the advantage of the wide wavelength range of transparency and large electrooptic and photoelastic coefficients. Nevertheless, recently the potential of $LiNbO_3$ used in monolithic device has been investigated by doping erbium into it to make $LiNbO_3$ capable of being light emitting, [11].

Most research in monolithic OICs use gallium arsenide and its alloys, of which the emitted wavelength can be altered from 650nm (AlAs) to 1.7μm (GaInAsP) by changing the fractional atomic concentration of the constituents. GaAs has relatively large electrooptic and acoustooptic figure of merit and some other desirable properties making them useful for modulators and switches, [12]$\sim$[14].

1.2 Concepts in Acoustooptic Integration

The acoustooptic interaction between elastic waves in solid and optical waves was firstly reported in 1922 by Brillouin [15]. The first acoustooptic device was demonstrated in 1932 by Lucas and Biquard in France [16], and Debye and Sears in the United States [17]. Then further work was proposed and the mechanism of the AO interaction was explained by Raman and Nath in 1935 in India [18], and one regime of acoustooptic effect was named after their important work. The acoustooptic interaction arises because of the periodic changes in the dielectric permittivity of a medium due to the elastic wave. Hence the optical fields going through the acoustic wave can be deflected, diffracted and modulated.

Using acoustooptic effect, acoustic waves could be utilized to constitute a simple

means for rapidly changing the parameters of an optical beam, for instance, intensity, direction, and frequency, [19]. Conversely, an optical beam is an ideal probe for measuring certain characteristics of an elastic wave beam within a solid, for instance, attenuation and propagation pattern, [20] . A number of applications concerned with acoustooptic interaction have been developed, such as modulators [21], deflectors [22], variable delay lines [23], spectrum analyzers [24] and tunable optical filters [25]. Those devices have been widely used in many areas, such as in laser printers and optical interferometers, [26] etc.

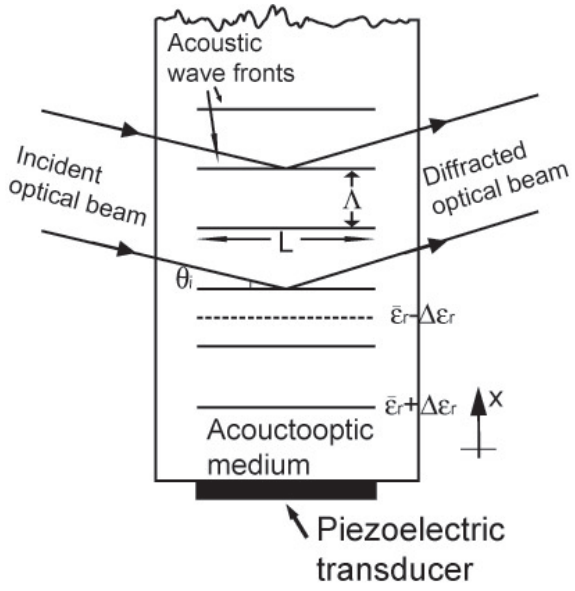

Figure 1.1: Schematic of the interaction between an incident light beam and an acoustic beam. On the wavefronts of the acoustic wave, the permittivity $\bar{\epsilon}$ is perturbed to $\bar{\epsilon} + \Delta\epsilon$ and $\bar{\epsilon} - \Delta\epsilon$ on peaks and valleys of the wave. The optical beam can be normal incidence or oblique and the diffracted beam can be a single or multiple beams.

A typical set-up of an incident optical beam diffracted by an acoustic beam is illustrated in figure 1.1. The bulk acoustic wave is generated by a transducer, of which the function is to transform radio frequency (rf) signal to acoustic waves in an piezoelectric material (see section 2.1.4). The optical beam of frequency ω and incident angle θ_i is diffracted to another direction(s) after going through the acoustic beam of width L.

Simply saying, it is the refractive index grating formed by the propagating acoustic wave, that induces the diffraction of the incident light. Supposing the relative permittivity ($\epsilon_r = \epsilon/\epsilon_0$, ϵ_0 the permittivity in free space) of the material with the acoustic wave absent is $\bar{\epsilon}$, the perturbation from the acoustic wave gives

$$\epsilon_r(x,t) = \bar{\epsilon}_r + \Delta\epsilon_r \cos(\Omega t - Kx) \tag{1.1}$$

with $\Delta\epsilon_r$ being the amplitude of the perturbation and Ω and K being the angular frequency and propagation constant of the acoustic wave, separately. The grating expressed by equation (1.1) has a period $\Lambda = 2\pi v/\Omega$ traveling along x direction at velocity v. Given that v is much smaller than the light speed, the grating can be considered stationary relative to the incident light, thus the effect of the wave is only denoted by a change of optical frequency from the Doppler effect.

It will be shown that the proportion of light diffracted by such a grating is related to the parameter Ψ, [27]

$$\Psi = k_0 \Delta n L \tag{1.2}$$

known as the modulation index. Δn is the associated index perturbation ($n^2 = \epsilon_r$, see Appendix D), L is the interaction length as seen in figure 1.1 and $k_0 = 2\pi/\lambda_0$ is the wave number of the light beam with λ_0 being the light wavelength in vacuum

To characterize the types of diffraction, the figure of merit Q is defined [27]

$$Q = \frac{2\pi\lambda_0 L}{\Lambda^2} \tag{1.3}$$

There exist two extreme cases in which analytical solutions to the problem of light diffraction by acoustic waves are given by

$$Q < 1; \qquad \text{and} \qquad Q > 2\pi \tag{1.4}$$

The first is the Raman-Nath and second is Bragg regime. The intermediary region where $1 < Q < 2\pi$, gives a mixture of the extreme characteristics.

Description on the two regimes follows on the assumption that the incident light is a plane wave, i.e. a well-collimated beam.

Raman-Nath regime This case corresponds to the zone of $Q < 1$. It is used with normal or quasi-normal incidence. The initial light beam, of angular frequency ω and of amplitude 1, is split, after interacting with the acoustic wave, into several beams corresponding to different orders of diffraction and distinguished by $0, \pm 1, \pm 2, \cdots \pm N$, respectively of angular frequency $\omega, \omega \pm \Omega, \cdots \omega \pm 2\Omega, \cdots \omega \pm N\Omega$, of direction $n\boldsymbol{k}, n\boldsymbol{k} \pm \boldsymbol{K}, n\boldsymbol{k} \pm 2\boldsymbol{K}, \cdots n\boldsymbol{k} \pm N\boldsymbol{K}$ and of amplitudes $J_0(\Psi), J_{\pm 1}(\Psi), J_{\pm 2}(\Psi)$,

$\cdots J_{\pm N}(\Psi)$. The zero order is the extension of the direct beam, the beam $+N$ corresponds to the annihilation of N phonons in the crystal, while $-N$ corresponds to the creation of N phonons.

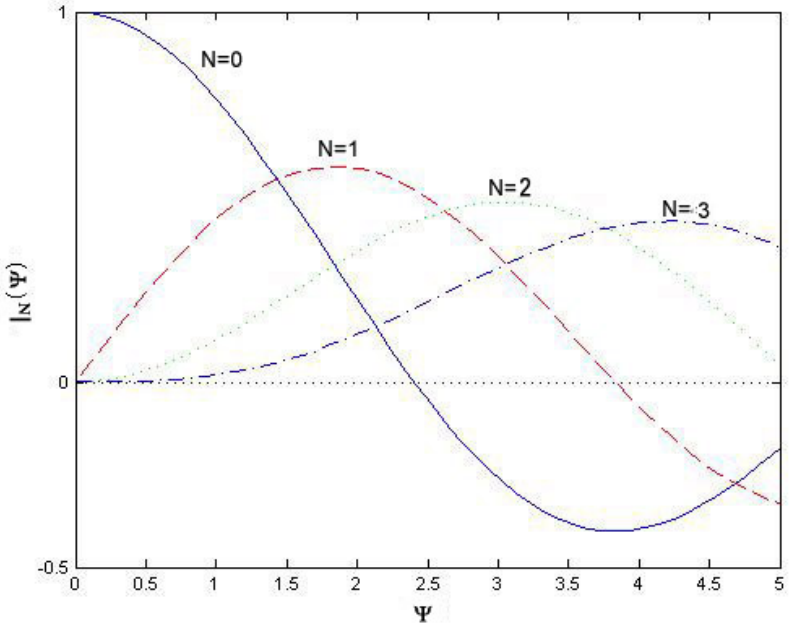

Figure 1.2: Intensity of different orders of diffracted beams as a function of the modulation index Ψ in Raman-Nath regime.

The $J_N(\Psi)$ are Bessel functions of order N of the variable Ψ. The light intensities of light I_N which are equal to J_N^2 (the equality of $J_{+N}^2 = J_{-N}^2$ results from the properties of Bessel functions), are shown in figure 1.2. For the smallest modulation indices Ψ, only the $+1$ and -1 orders appear, symmetrical to the central beam. with Ψ increases, $+2$ and -2 orders appear then $+3$ and -3 and so forth.

Bragg regime In the zone of $Q > 2\pi$, Bragg regime works. In this case there is only a single diffracted beam. The phenomenon only involves one phonon per photon, absorption and emission cannot occur simultaneously, contrary to what happens in Raman-Nath regime.

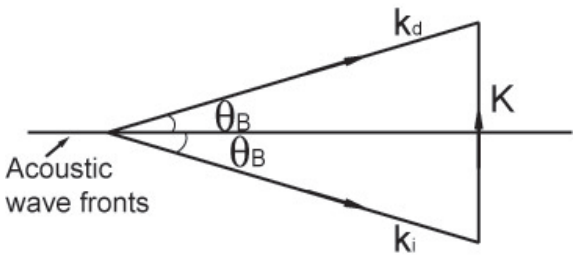

Figure 1.3: Bragg diffraction in the case of absorption of a phonon in a medium where the refractive index is the same for incident and diffracted optical wave.

Momentum conservation between associated quantities between interacting phonons and photons, and Doppler shift gives

$$\begin{aligned} \boldsymbol{k}_d &= \boldsymbol{k}_i \pm \boldsymbol{K} \\ \omega_d &= \omega_i \pm \Omega \end{aligned} \tag{1.5}$$

where the subscripts donates the incident or diffracted photon and $\pm$ corresponds to the annihilation and creation of a phonon. The case of an absorption of a phonon is shown in figure 1.3.

Given that $\Omega << \omega$, $\omega_i \approx \omega_d$ and $\boldsymbol{k}_i \approx \boldsymbol{k}_d$, equation (1.5) gives the expression of the incident angle θ_B

$$\theta_B = \sin^{-1} \frac{\lambda_0}{2n\Lambda} \tag{1.6}$$

and θ_B is called Bragg angle. When the condition of equation (1.6), also called Bragg condition, is satisfied, the proportion η of diffracted light is at a maximum and equal to [27]

$$\eta = \sin^2 \frac{\Psi}{2} \tag{1.7}$$

In Bragg regime, the acoustic plane wavefronts act like partially reflecting mirrors, of which the reflective power can be varied by varying the acoustic power (and hence $\Delta\epsilon$). The efficiency η of AO interactions with different acoustic frequencies as a function of acoustic power is shown in figure 1.4.

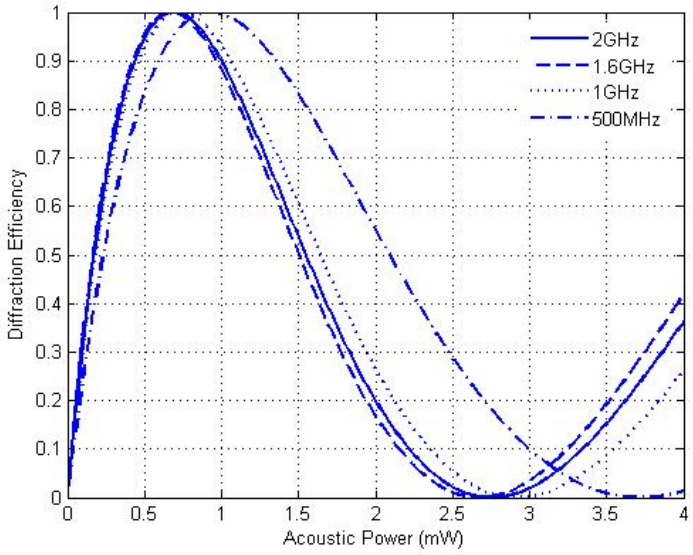

Figure 1.4: Diffraction efficiences of acoustooptic diffraction in Bragg regime. The incident light is of wavelength in vacuum $\lambda_0 = 405$nm. The intraction length is 100μm.

As opposed to the Raman-Nath regime, the Bragg regime makes it possible for a suitable value of Ψ to deflect all the incident light power into a single direction (situation corresponding to $\Psi = \pi, 3\pi, 5\pi, \cdots$). This feature brings more applications of Bragg diffraction in practical devices than Raman-Nath diffraction.

Acoustooptic interaction with surface acoustic wave As shown in figure 1.1, the interaction with optical beams is operated with acoustic bulk waves, which is the case that was firstly used in the early age of AO devices. However, cases with surface acoustic waves are also possible. Surface acoustic wave (SAW) is such a type of wave that the acoustic wave is decaying along the depth normal to the surface of the device and thus the acoustic power is mainly confined in a layer close to the surface of a thickness in the order of one acoustic wavelength. Such acoustooptic devices have several advantages over the bulk wave device, which will be discussed later.

There are several possible configurations of this type of interaction: top reflection, shown in figure 1.5a; top transmission, shown in figure 1.5b; back reflection, shown in figure 1.5c; and side entry, shown in figure 1.5d.

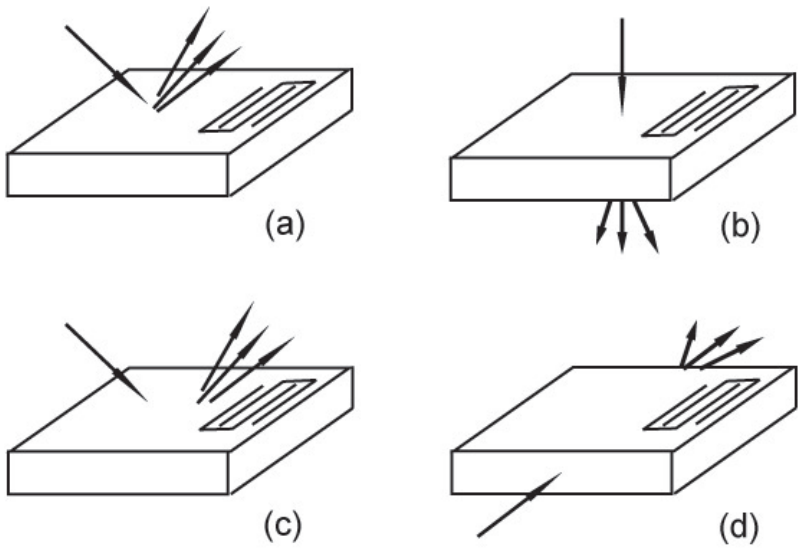

Figure 1.5: Surface acoustic wave involved AO interaction geometries: (a) top reflection; (b) top transmission; (c) back reflection; (d) side entry.

In the top-reflection configuration, light is incident from above the device and reflects from the surface on which the SAW propagates. Diffraction occurs because the propagating SAW produces small corrugations in the device surface. Although the interaction is weakest in this configuration, it is a useful arrangement for non-contact probing of surface waves using light, [28]. Because the light interaction is relatively weak compared with other device geometries, this configuration is seldom used in optical signal processing applications, [29].

In the top transmission geometry, the incident light is directed nearly normal to the surface on which the acoustic wave propagates, passes through the SAW and diffracted into multiple orders at the bottom of the surface. Since the interaction length, which is the penetration depth of the SAW, is quite short, Raman-Nath diffraction occurs. Although this interaction is somewhat stronger than the top reflection, it still is very weak due to the short interaction length. An improvement in the interaction length is possible using the configuration of back reflection in figure 1.5c. In this case, the light is incident as the top transmission case, while after passing through the material, it is reflected by a mirror back through the acoustic wave. In addition to the diffraction caused by transmission through the SAW, the periodic corrugation of the surface contributes to the overall diffraction effect.

All of the techniques described above produce rather weak AO interactions, but the side-entry configuration shown in figure 1.5d provides a vast improvement in

interaction length and hence higher diffraction efficiency. Incident light enters from the side of the device, just beneath the top surface, and propagates parallel to the surface on which the SAW is propagating. Both the light and SAW therefore are in the same plane. The interaction length of this case is given not by the SAW penetration depth but rather by the acoustic beam width, which depends on the length of the transducer and can be arbitrarily long. Therefore the Bragg regime applies and the enhancement to the diffraction efficiency can be sufficiently large with lower power. The side-entry geometry is thus the main type of surface wave AO devices used at present.

1.3 Acoustooptic Devices

Acoustooptic devices, either Raman-Nath or Bragg regime utilized, provide a simple and efficient mean for deflecting and modulating light beams. A lot of applications have been realized in industry till now, like optical signal processing [30], optical computing [13] and optical beam steering [31]. Typical AO devices are introduced in this section.

Modulator The acoustooptic interaction can be used to construct a variety of light modulators, which can operate in either Raman-Nath regime [19] or the Bragg regime [32]. In the case of Raman-Nath modulator, the requirement of $Q < 1$ indicates the limit of low optical frequency operation. Thus AO modulators based on Bragg regime attracts more interest of researchers nowadays due to its potential in high efficiency, larger dynamic range and wider bandwidth.

When the AO effect is very weak or very small power level, the diffraction efficiency defined in equation (1.7) becomes increasingly linear with the acoustic intensity

$$\eta = \frac{\pi^2 L^2 M_2 I_a}{2\lambda_0^2} \tag{1.8}$$

where I_a is the power density of the acoustic wave and M_2 is the figure of merit of the associated material for which the larger the better. Therefore, if the acoustic intensity is modulated, so is the diffracted optical beam intensity. Thus acoustooptic Bragg diffraction offers a way of imprinting information on the optical beam. The

attainable modulation bandwidth for a incident Gaussian beam is given

$$\Delta f \approx \frac{v \cos \theta_i}{w_0} \tag{1.9}$$

with v being the acoustic velocity, θ_i being the incident angle and w_0 is the spot size of the Gaussian beam at the waist. The bandwidth is thus inversely proportional to the beam diameter of the light and proportional to the acoustic wave velocity. A larger modulation bandwidth can be obtained by using optical beams with small width and higher acoustic velocity.

Deflector Basically acoustooptic deflectors operate in the same way as Bragg diffraction modulators, the only difference being that the frequency rather than the amplitude of the acoustic wave is varied. The use of acoustooptic interaction offers the possibility of high resolution beam deflection, [33]. The change of the deflection angle (the angle between the diffracted and the incident optical beam) with the change of acoustic frequency is

$$\Delta\theta_d = \frac{\lambda_0}{\bar{n}v}\Delta f \tag{1.10}$$

The angle of deflection is thus proportional to the change in the acoustic frequency. The key parameter for an acoustooptic deflector is the number of resolvable spots given by

$$N \approx \frac{w_0}{v}\Delta f \tag{1.11}$$

Therefore a wider Gaussian beam leads to a larger resolution for a deflector.

Spectrum Analyser Acoustooptic Bragg diffraction can also be used to analyze the power spectrum of an rf signal [34]. If the acoustic wave consists of many frequency components, each of them will deflect the optical beam to a unique direction. The diffracted light thus consists of an angular distribution. By using a group of lens, each direction of the directed light will correspond to a spot in the focal plane. Since the diffraction efficiency is proportional to the power of the acoustic wave at each frequency, the optical intensity distribution in the focal plane is proportional to the power spectrum of the RF signal. The optical intensity in the focal plane is usually sensed by a photodetctor array. Since the acoustooptic spectrum analyzer

is based on a simultaneous deflection of a laser beam into many directions, its operation characteristics, such as the rf signal bandwidth and the number of resolvable spots, are similar to those of beam deflectors.

1.4 Organization of this Report

This report is planned to review the useful and necessary background knowledge and propose the investigation to the characteristics and feasibility of a monolithic FISOS. Hence a logic structure, or a design tree for such an integrated device, is illustrated in figure 1.6.

In this figure, elements are classified into two classes. Ones surrounded by rectangles are units of initial parameters of the proposed device. Apart from the injected rf power supply, IDT (interdigital transducer, to generate acoustic waves) is the key design consideration in acoustic wave generation and propagation; while in optical source the transverse and lateral structure plays important roles in optical gains and optical modes confinement. Not all parameters are shown in the figure, such as the associated materials, the injected current and the etch depth of the ridge waveguide, but the dominant ones which can readily affect the performance of the device are exhibited. The dashed lines connect an element and its parameters, such as the IDT and its location, length or spacing. This class of elements can be treated as the 'input' of the comprehensive modeling of the integrated device.

The other elements, which are surrounded by ellipsse, are the resultant features of interest or associated performance of particular applications. For example, optical modes, solely depending on the transverse and lateral structure, provides an evaluation to the optical property of the optical source; the diffraction efficiency and bandwidth are key characteristics of AO modulators and deflectors. Those elements are all involved in the modelling of investigation into the FISOS. The solid lines connect the features and the parameters which contribute those features. Lines with overlaps indicate they work together, but it is not the case where there are arch intersections. This class of elements can be treated as the 'output' of the modeling of the integrated device.

This graph gives a clear idea about the logic structure of the design guideline of the FISOS. For example, one can find the rf frequency (acoustic frequency) is involved in all output characteristics except optical modes, and rf power only affects

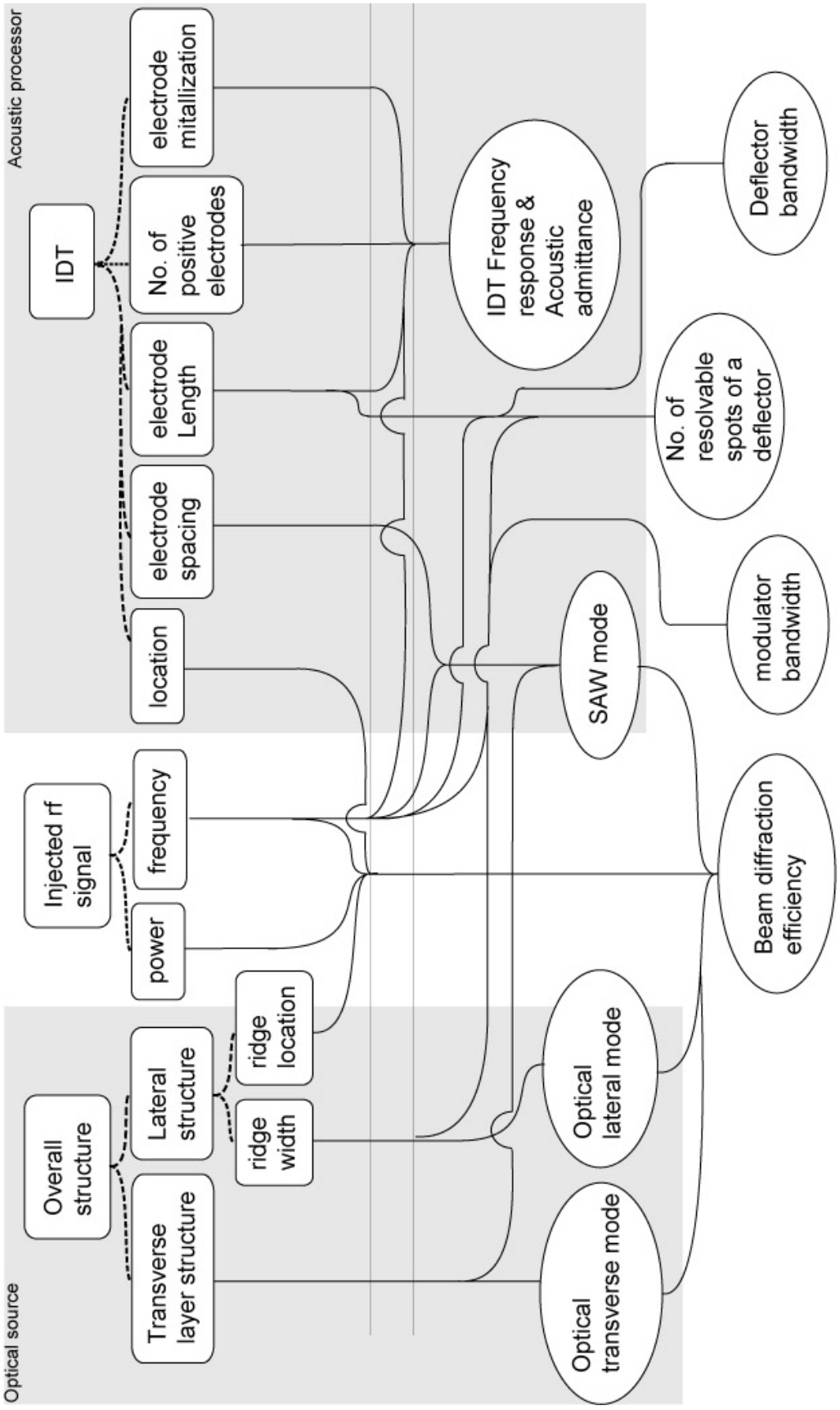

Figure 1.6: Schematics of the logic structure of FISOS's design.

the diffraction efficiency but has nothing to do with the bandwidth and resolution of a deflector. It must be pointed out that this graph is so concise that only a brief idea, rather precise, can be obtained, and the logic links (solid line) might work only in most general cases, if not all, because there are many assumptions associated in specific cases.

The structure of this report is thus organized following this graph. In Chapter 2, the elasticity of solid is reviewed; the excitation (piezoelectricity of material) and propagation of acoustic waves, particularly surface acoustic waves are introduced. Transfer matrix method is demonstrated for the simulation of SAW in multilayer medium. The concept of the IDT is given and the transmission line model is utilized to achieve the electrical features such as the admittance of an IDT.

Given the fact that the acoustooptic interaction is actually the alteration of optical characteristics by a traveling grating generated by the acoustic wave, a rigorous grating diffraction theory is demonstrated in Chapter 3. Starting from the Maxwell's equations, the electric fields associated in the grating can be represented by Floquet's theory. Two fundamental diffraction approaches, coupled-wave method and modal method are discussed. They are actually two different expressions of fields in the rigorous grating diffraction theory. Generally used approximate methods, such as two-wave-first-order method (usually called couple-mode method) and Raman-Nath approximation, can both be derived from the rigorous theory.

Before the coherent light source was invented bulk wave acoustooptic diffraction worked dominantly in AO device. Since the proposition of OIC the traditional AO device was improved by using surface acoustic waves instead of bulk waves and guided optical waves instead of light of radiation mode. The new features and characteristics of those guided wave AO interactions, as well as a brief review on dielectric waveguide theory, are introduced in Chapter 4. The nonuniformity of both optical and acoustic waves in their interaction region gives rise to an extra complexity, that the diffraction efficiency strongly depends on the associated optical and acoustic mode apart from acoustic power and frequency, as indicated in figure 1.6.

With all the background knowledge prepared, the task of the integration of an optical source and an planar AO device is ready to be proceeded. In Chapter 5, a guideline about the material selection is represented firstly. The structure of the associated semiconductor optical source is then discussed. The overall device design

guideline and considerations are represented at the end of chapter.

The parameters used in the modeling and the device configuration are illustrated in Chapter 6. The optimization of the associated parameters of FISOS (the first class elements in figure 1.6) are investigated and discussed. An improvement to the expression of acoustooptic diffraction efficiency is proposed and used for analysis. As an example, the characteristics of an integrated modulator and a deflector are discussed, and suggestions about the optimization to their performances are given. Some issues about the tolerance of the system are also discussed at the end of this chapter, such as misalignments and the incoherent optical source.

Conclusions and Future work are represented in Chapter 7.

Chapter 2

Acoustic Waves in Elastic Material

Acoustic waves have played an important role in electronics for many years. Utilizing their capability of coupling with electrical signals and much lower velocities compared with electromagnetic waves, acoustic waves were widely used in resonators [35], convolvers [36], delay lines [37] and filters [38], etc. It was mainly bulk acoustic waves employed in those devices before the invention of the interdigital transducer (IDT) by White and Voltmer in 1965 [39], which made it possible to efficiently launch a surface acoustic wave (SAW). The main advantage of surface wave devices is that they are smaller than the bulk wave devices. Lower rf power is required because the SAW is concentrated inside a layer of thickness about a wavelength and thus its power density can be extremely high. Moreover, the beam of a surface wave is accessible at every point of the free surface and can thus be modified at will. It can be deflected, amplified, attenuated, detected all along its length. It can propagate in a thin layer deposited on the substrate, which can serve as a optical waveguide at the same time. Under certain conditions, there is an interaction of two types of waves, which has been introduced in the previous chapter.

This chapter presents the transmission of bulk acoustic waves in homogeneous medium and surface acoustic wave in multilayer structure system. Basic concepts of strain and stress in an elastic medium, the acoustic waves, and the dynamic equation are introduced in section 2.1. The propagation and characteristics of surface acoustic waves in a semi-infinite medium are discussed in section 2.2. The simulation of SAW in layered medium using the transfer matrix method is represented in section 2.3. Section 2.4 discusses the conventional technique to launch acoustic surface waves by utilizing the interdigital transducer (IDT) and demonstrates how to calculate

its admittance and frequency response numerically. Finally, an example of SAW generation and propagation in a given multilayer structure is demonstrated and its mechanical and electrical characteristics are analyzed.

2.1 Elasticity Theory

In the following content the concepts in elasticity theory and the behaviour of elastic waves are discussed in solid. Liquid is out of the interest of the author. The solid body is also considered to be a homogeneous continuum disregarding the fact that matter consists of discrete atoms or molecules. Under the influence of external forces, the distances separating the different material points in a medium become modified. It is then said that it has undergone a 'deformation'. This is obviously not the case with displacements such as translation or rigid-body rotation, where the separation distance is unchanged.

Internal forces known as stresses will develop opposing the deformation of the solid body, and will tend to make it return to its initial shape and volume. A material is said to be elastic when, as the stresses reduce to zero, so does the deformation, which in this case, constitutes a reversible state in the solid body.

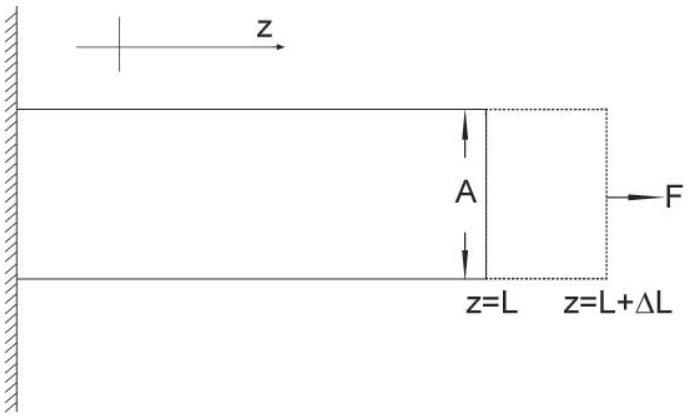

Figure 2.1: Uniform dilation of a rod by an applied force.

A material can be elastic up to a certain limit value of strain, and cease to be so beyond that point. Consider a rod of length L and cross-sectional area A fixed at one end on a static wall with an external force F exerted uniformly over its cross section, as shown in figure 2.1. The rod is thus stretched and the internal force exists because of the deformation of the rod. When the stretch is weak enough, the relationship between the internal force and the rod's extension in length ΔL can be

described by Hooke's law,

$$\frac{F}{A} = c\frac{\Delta L}{L} \tag{2.1}$$

where c is a constant depending on materials, called modulus of elasticity. What is shown in figure 2.1 is a simple case in one dimension with the deformation along z-axis only. In this case the internal force and the stretched length are expressed as scalars. In order to describe situations with deformation in three dimensions, both the internal forces (stress T) and the deformation (strain S) must be represented by second rank tensors and the elastic modulus is rewritten as a tensor of rank 4 known as a stiffness tensor.

The use of tensor representation is hardly avoidable because of the anisotropy of materials. For example in electromagnetics the dielectric constant ϵ and dielectric susceptibility χ can be represented in second rank tensor in uniaxial or biaxial crystal. Whilst in elastics not just second rank tensor such as strain and stress, tensors of third rank such as piezoelectric constant and fourth rank such as stiffness constant may also be employed in elastically anisotropic crystal. Therefore, the mathematical formalism associated with elastic waves becomes more complicated compared with electromagnetic waves.

2.1.1 Elastic Deformation

Consider a small volume element surrounding a point M of coordinates x_M of components x_i (i=1, 2, 3, i.e. x, y and z-axis in Cartesian coordinates) referenced to the origin O in a deformed rigid solid, as shown in figure 2.2. As a result of an infinitesimal displacement $\boldsymbol{u}_M$ (quantity in bold indicates it is a vector), also known as an elongation, of components u_i, the point M moves to M' with its new coordinates

$$x'_M = x_M + \boldsymbol{u}_M = x_i + u_i \tag{2.2}$$

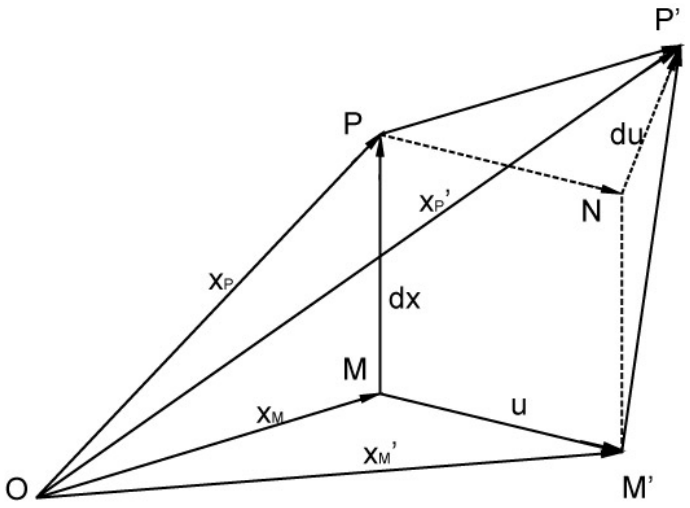

Figure 2.2: Two neighbouring point M and P in a deformed solid are displaced by different amounts in different directions.

The displacement vector $\boldsymbol{u}_M$ is defined as a continuous function of the coordinates x_i. The position of its neighbouring point P, a distance of $d\boldsymbol{x}$ away, become modified through continuity from x_P to x'_P by a displacement $\boldsymbol{u}_P$ composed of a translation $\boldsymbol{u}_i$ and a rigid body rotation, as well as the deformation which alters the inter-particle distance. Going to first order, it is found that the vector $\overrightarrow{MP}$ has become $\overrightarrow{M'P'}$, the summation of $\overrightarrow{MP}$ and the vector $d\boldsymbol{u}$ ($\overrightarrow{NP'}$ in figure 2.2) of components

$$du_i = \frac{\partial u_i}{\partial x_j} dx_j \tag{2.3}$$

and thus the point P is displaced to P' of coordinates,

$$x'_P = x_P + \boldsymbol{u}_p x_P + \boldsymbol{u}_i + d\boldsymbol{u} x_i + dx_i + u_i + \frac{\partial u_i}{\partial x_j} dx_j, \quad i,j = 1,2,3 \tag{2.4}$$

where the summation from 1 to 3 over the index j is applied. The partial derivatives $\partial u_i/\partial x_j$, i.e. the gradient of displacements, are in general functions of the coordinates x_i of the point M. It will be supposed that the distance variation between particles is small as compared with the distances themselves, and this leads to $\frac{\partial u_i}{\partial x_j} << 1$.

The solid is deformed only if different material points are displaced relative each other, i.e. $\partial u_i/\partial x_j$ is non-zero. But this is not the case when there is just a simple local rotation occurs with the gradient of displacements still non-zero; the distances between material points are not affected and therefore the internal state of the solid

is left unchanged. Hence simply using $\partial u_i/\partial x_j$ is not appropriate to express the solid deformation. In fact, it is found that the gradient of displacements can be written in the form of a matrix summation

$$\frac{\partial u_i}{\partial x_j} = S_{ij} + \omega_{ij} \tag{2.5}$$

and

$$S_{ij} = \frac{1}{2}\left(\frac{\partial u_i}{\partial x_j} + \frac{\partial u_j}{\partial x_i}\right) \tag{2.6}$$

$$\omega_{ij} = \frac{1}{2}\left(\frac{\partial u_i}{\partial x_j} - \frac{\partial u_j}{\partial x_i}\right) \tag{2.7}$$

The symmetric part S_{ij}, called strain, which is zero for any overall movement, a translation or rotation, therefore express the deformation when internal forces occurs. The antisymmetrical part ω_{ij}, which is nonzero when only a local rotation occurs, does not contribute to the deformation of solid. Taking into account this decomposition, the following is therefore obtained for the components of $d\boldsymbol{u}$

$$du_i = S_{ij}dx_j + \omega_{ij}dx_j \tag{2.8}$$

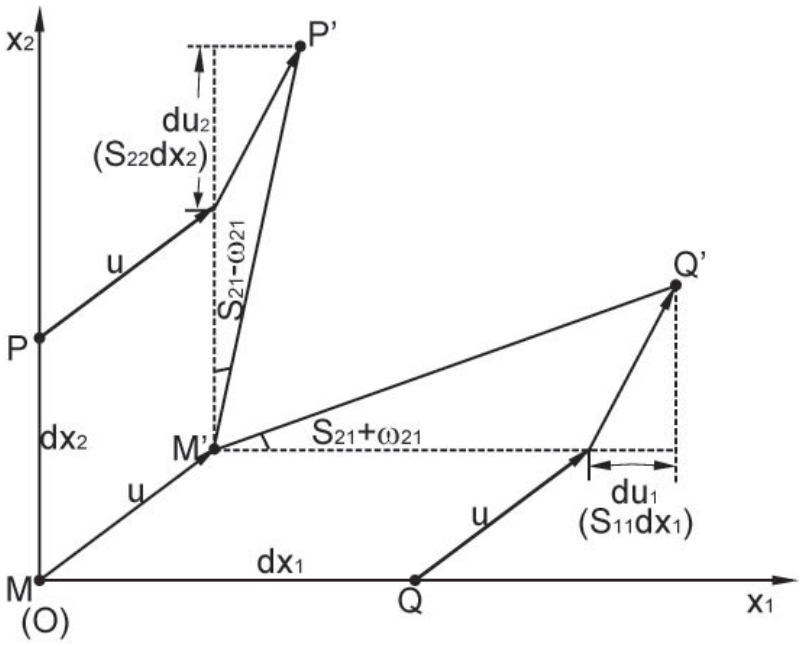

Figure 2.3: Schematics of the strain tensor component S_{ij}. The vectors $\overline{MQ}$ and $\overline{MP}$ parallel to the axes Ox_1 and Ox_2 are approximated to $2S_{12}$ after deformation.

In order to understand the matrix elements of S_{ij} and ω_{ij}, a geometric schematic is illustrated in figure 2.3. The S_{ij}, a second rank tensor, is used to express the

elongation per unit length of a neighbour point situated inside the volume element surrounding the point M. The vector $\overrightarrow{MP}$ is supposed to be parallel to the axis Ox_1, of length dx_1, equation (2.8) thus gives for $d\boldsymbol{u}$

$$du_1 = S_{11}dx_1; \quad du_2 = (S_{21} + \omega_{21})dx_1 \tag{2.9}$$

If Q', M' are the displaced locations of Q and M respectively, it can be seen that $S_{21} + \omega_{21}$ is the angle turned by $\overrightarrow{MQ}$ in the direction Ox_1 towards Ox_2 and S_{11} is the elongation per unit length of the element MQ in the direction Ox_1.

Meanwhile, let MP be an element of length parallel to Ox_2. The S_{22} gives the elongation per unit length in the direction Ox_2. The angle turned by MP in the Ox_2 direction towards Ox_1 is $S_{12} + \omega_{12}$. Considering the symmetry of S_{ij} and ω_{ij} described in equation 2.6 and 2.7, this angle is equal to $S_{21} - \omega_{21}$. Hence the magnitude of ω_{21} describes a local rotation of vector $\overrightarrow{M'Q'}$ and $\overrightarrow{M'P'}$ by the point M and during the rotation the angle between the vectors $\overrightarrow{M'P'}$ and $\overrightarrow{M'Q'}$ holds, equal to $\frac{\pi}{2} - 2S_{12}$. Other elements of S are understood in an analogous manner.

The S_{ii} are known as the longitudinal strain components while the $S_{ij}(i \neq j)$ are the shear components. The longitudinal components give rise to the elongation of stretch and compression, like along the direction of vector $\overrightarrow{MQ}$. The shear components contribute the elongation of distortion associated with sliding of material, like perpendicular $\overrightarrow{MQ}$. The term ω_{ij}, the antisymmetric part of the gradient of displacements, describes a local rotation which may vary with position in the solid. It plays no role in the propagation of elastic waves because it only causes a small inertial term, negligible in comparison with other terms in the dynamical equations and will not be considered in the following discussion.

2.1.2 Stress Tensor

In a deformed body there originate forces known as internal stresses. They tend to restore it to the state of equilibrium before deformation, and, in an elastic body, they tend to zero in the same way as the strain.

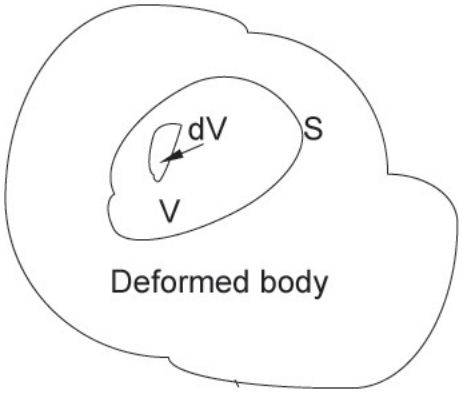

Figure 2.4: Deformed body in which a volume V bounded by the surface S is isolated; dV is the volume element inside S.

Consider a volume V within the deformed body bounded by a closed surface S and carry out the summation $\iiint F dV$ of all applied forces, dV being the volume element contained inside S, as shown in figure 2.4. First of all there are internal forces which act upon one another. The resultant of this action and reaction is zero, there remain the forces due to the material outside the volume under consideration. The forces at work in elasticity are of very limited range, of the order of the distance between adjacent molecules. But, in this particular approximation where the solid is considered as a continuum, the dimensions concerned are very great compared with interatomic distances. The range of these forces will therefore be considered as zero.

Thus only adjacent parts act upon the envisaged volume and will be distributed over the surface S by which it is bounded. The resultant $\iiint F dV$ is thus equal to an integral taken over S. Consequently, F must be equal to the divergence of a second rank tensor. The components F_i are therefore written

$$F_i = \frac{\partial T_{ij}}{\partial x_j} \tag{2.10}$$

where T_{ij} is known as the stress tensor.

In relating the volume integral of F_i to the surface integral, taking into account the previous equation,

$$\iiint_V \frac{\partial T_{ij}}{\partial x_j} dV = \iint_S T_{ij} dS_j \tag{2.11}$$

where dS is the vector of surface element taken normal to S and pointing towards the outside. Note that $\iint T_{ij} dS_j$ is the resultant of forces exerted on the volume

bounded by S. In equilibrium the volume in question exerts inversely a force equal to the former but of opposite sign on the remainder of the body and across the surface of separation S.

It is easily understood that the stress tensor T_{ij} is symmetric in the same way as the strain

$$T_{ij} = T_{ji} \tag{2.12}$$

The T_{ii} is interpreted as the force which acts normally on the unit surface element, while the $T_{ij}(i \neq j)$ are the forces tangential to this surface, i.e., the T_{ii} are the normal components of the stress tensor and the $T_{ij}(i \neq j)$ are the shear components.

2.1.3 Stiffness Tensor

In a deformed elastic body internal stress occurs. It is supposed that each component of a stress tensor is a linear and homogeneous function of all the components of the strain tensor. The set of all these relations

$$T_{ij} = c_{ijkl} S_{kl}; \quad i, j, k, l = 1, 2, 3 \tag{2.13}$$

constitutes what is known as the generalized Hooke's law, which is an extension of the simple Hooke's law (2.1) relating to isotropic elastic bodies. The set c_{ijkl} constitutes a tensor of rank 4 known as the stiffness tensor. The S_{kl} and T_{ij} components can vary from one point to another. On the other hand, in elastic media considered to be homogeneous, the c_{ijkl} are independent of spatial coordinates, once the reference trihedron is fixed.

Given the symmetry of stress ($S_{ij} = S_{ji}$) and strain ($T_{ij} = T_{ji}$), the stiffness tensor is symmetrical as regards to the suffixes i and j, k and l, and ij and kl. It can be proved that the number of independent elements of the stiffness tensor is reduced from 81 to 21. Depending on symmetry from a specific crystalline system, the number of independent elements can be further reduced. An isotropic medium (like fused silica), for example, has only two independent elements while the 6mm material (like GaN) has five when the crystal internal coordinates system is used.

Moreover, the notation of tensors can be simplified taking the symmetries into account. The i and j suffixes will be grouped into one to be designated by m

($m = 1, 2, \cdots 6$) while the k and l suffixes will be replaced by the single suffix n ($n = 1, 2, \cdots 6$), by letting $m = i$ ($i = j$) or $m = 9 - i - j$ ($i \neq j$).

For example

$$S_1 = S_{11}; S_3 = S_{33}; S_4 = S_{23} = S_{32}; T_5 = T_{13} = T_3 1; c_{14} = c_{1123} = c_{1132}$$

With this notation the tensorial relation (2.13) can be rewritten in the form

$$T_m = c_{mn} S_n \tag{2.14}$$

T_m and S_n are then matrices with 6 rows and 1 column, and c_{mn} is a 6×6 square matrix. It is obvious that $c_{mn} = c_{nm}$. Taking GaN as an example, there are five independent elements of stiffness tensor, c_{11}, c_{12}, c_{13}, c_{33} and c_{44}. The stiffness tensor is in the form of

$$\begin{pmatrix} c_{11} & c_{12} & c_{13} & 0 & 0 & 0 \\ c_{12} & c_{11} & c_{13} & 0 & 0 & 0 \\ c_{13} & c_{13} & c_{33} & 0 & 0 & 0 \\ 0 & 0 & 0 & c_{44} & 0 & 0 \\ 0 & 0 & 0 & 0 & c_{44} & 0 \\ 0 & 0 & 0 & 0 & 0 & \frac{1}{2}(c_{11} - c_{12}) \end{pmatrix} \tag{2.15}$$

2.1.4 Piezoelectricity

In a non-piezoelectric medium the stress only depends on the strain through the elastic tensor. In the same way, electric displacement D is uniquely related to the electric field E through the permittivity tensor ϵ. In piezoelectric medium, because of the coupling between electric and mechanical parameters, the application of an electric field stimulus will give rise to mechanical deformation and vice versa. Thus the stresses, as well as electric displacement, are functions of both strains and electric field, and the constitutive equations of piezoelectricity are written

$$\begin{aligned} T_{ij} &= c^E_{ijkl} S_{kl} - e_{kij} E_k \\ D_i &= e_{ikl} S_{kl} + \epsilon^S_{ik} E_k \end{aligned} \tag{2.16}$$

where c^E is the elastic tensor in zero electric field and ϵ^S the permittivity tensor at zero strain. The superscripts will be omitted in c^E_{ijkl} and ϵ^S_{ik} to simplify the notation but they must be always understood. The piezoelelctric tensor e is introduced in

equation (2.16) to link the electric field and mechanical quantities. The fact that e_{kij} and e_{ikl} are components of the same tensor follows the thermodynamic relations, [40].

Because of the proper symmetry of the stress and strain tensors the piezoelectric tensor is symmetrical in j and k, i.e. $e_{ijk} = e_{ikj}$ $(i, j, k = 1, 2, 3)$. It is sometimes more convenient to use the reduced notation analogue which was presented in the previous section,

$$e_{im} = e_{ijk}; \quad i, j, k = 1, 2, 3; m = 1, 2, \quad \cdots 6$$

in which the first suffix of e stays but the other two j and k are grouped together and reduced to a single m. The piezoelectric tensor is thus expressed as a 3×6 or 6×3 matrix, and the constitutive equation (2.16) can be rewritten

$$\begin{aligned} T_m &= c^E_{mn} S_n - e_{km} E_k \\ D_i &= e_{in} S_n + \epsilon^S_{ik} E_k \end{aligned} \tag{2.17}$$

The piezoelectric tensor for a 6mm crystal, such as GaN, has three independent elements, e_{15}, e_{31} and e_{33} when the internal crystal coordinates system is used. It is in the form

$$\begin{pmatrix} 0 & 0 & 0 & 0 & e_{15} & 0 \\ 0 & 0 & 0 & e_{15} & 0 & 0 \\ e_{31} & e_{31} & e_{33} & 0 & 0 & 0 \end{pmatrix} \tag{2.18}$$

2.1.5 Equation of Motion

Consider a volume element dV surrounding the point M of coordinates x_i. According to the equation (2.10) the components along the i axis of the force acting upon dV is equal to $\frac{\partial T_{ij}}{\partial x_j} dV$. If $\boldsymbol{u}$ is the infinitesimal displacement from the point M, the fundamental equations of dynamics can be written

$$\frac{\partial T_{ij}}{\partial x_j} = \rho \frac{\partial^2 u_i}{\partial t^2} \tag{2.19}$$

with ρ being the mass density of medium at the point M.

2.2 Propagation of Surface Acoustic Wave

In 1885, Lord Rayleigh predicted that acoustic waves can propagate over a plane boundary between semi-infinite solid and a vacuum when he attempted to describe the effects of earthquakes, and hence the wave is often called a Rayleigh wave, [41]. In such a wave the amplitude decays rapidly in the direction perpendicular to the boundary surface, and thus the wave is confined close to the surface with depth in the order of one wavelength. Rayleigh wave is the basic type of surface acoustic wave and higher mode of SAW could be excited at higher frequency, [42].

Before the discussion on surface waves, it might be useful to discuss the propagation of a bulk wave in solid firstly. In fact there is no fundamental difference between surface and bulk acoustic waves since they both must satisfy the dynamic equation (2.19). It will be demonstrated that until combining with particular boundary conditions, solving surface acoustic wave problems has the same procedure as solving the bulk waves.

Bulk waves The dynamic motion equation (2.19) and equation (2.13) and again given below for convenience

$$\begin{aligned} T_{ij} &= c_{ijkl} S_{kl} \\ \frac{\partial T_{ij}}{\partial x_j} &= \rho \frac{\partial^2 u_i}{\partial t^2} \end{aligned} \tag{2.20}$$

By substituting T_{ij} into the motion equation, taking into account the expression S_{kl} and its symmetry in k and l, the set of equations (2.20) yields

$$\rho \frac{\partial^2 u_i}{\partial t^2} = c_{ijkl} \frac{\partial^2 u_k}{\partial x_l \partial x_j} \tag{2.21}$$

Thus a set of differential equations is obtained. It only involves the derivatives and governs the propagation of elastic waves, i.e. acoustic waves.

The solution of equation (2.21) completely defines the mechanical state of the crystal, since both the strains and stresses can be expressed (equation (2.6) and (2.13)) as a function of displacements. The set of equation (2.21) is, for acoustic waves, comparable to Maxwell's equations for light waves. The electric displacement vector $\boldsymbol{D}$ can be considered analogous to $\boldsymbol{u}$. Every electromagnetic quantity such as electric field, magnetic field, etc., is defined beginning with $\boldsymbol{D}$. When the solution of Maxwell's equations is found to be in the form of plane waves of the type $\boldsymbol{D} =$

$\boldsymbol{D}_0 e^{j(\omega t - \boldsymbol{k}\cdot r)}$ ($\boldsymbol{D}_0$ being the wave amplitude, ω being the angular frequency and $\boldsymbol{k}$ being the wave number), it is found that there are two allowed directions for $\boldsymbol{D}$ which are normal to $\boldsymbol{k}$ and perpendicular to each other. Their phase velocity is equal to ω/k and in general varies from one direction to another in optically anisotropic media.

In an infinite medium, there is no need to consider boundary conditions. For the displacement $\boldsymbol{u}$ at a point $\boldsymbol{r}$ the solution of plane wave which propagates in a lossless medium is supposed in the form

$$\boldsymbol{u} = \boldsymbol{U} e^{j\Omega(t - \boldsymbol{s}\cdot\boldsymbol{r})} \tag{2.22}$$

where Ω is the angular frequency of the wave and $\boldsymbol{s}$ is known as slowness, of which the direction indicates the wave propagation direction and the modulus is the reciprocal of speed. One must bear in mind that the quantity j appearing in the phase factor denotes the imaginary unit while as a suffix it means an integer 1, 2 or 3. Substituting equation (2.22) into the wave equation (2.21) yields

$$(c_{ijkl} s_j s_l - \rho\delta_{ik}) U_k = 0 \tag{2.23}$$

with $\delta_{ik} = 0$ when $i \neq k$. For nontrivial solutions of A_k the associated determinant must be equivalent to zero.

$$\det(c_{ijkl} s_j s_l - \rho\delta_{ik}) = 0 \tag{2.24}$$

The solution of equation (2.24) gives the velocities in the direction of propagation, which is independent of the frequency Ω. The medium is thus said to be nondispersive.

When considering an arbitrary direction of propagation there exist 3 possible directions for displacement $\boldsymbol{u}$ of the form (2.22), each characterized by a phase velocity v. When one of the directions is parallel to $\boldsymbol{s}$, the acoustic wave corresponding to it is said to be longitudinal, or compressive. The two other directions are automatically perpendicular to $\boldsymbol{s}$ and acoustic waves associated with them are said to be shear, or transverse. Alternately, there possibly exists in generally a direction for the vibration $\boldsymbol{u}$ close to the direction of propagation $\boldsymbol{s}$. The associated wave is then quasi-longitudinal, while the two other directions give quasi-transverse waves.

Taking the elastic wave propagating along x_1-axis in GaN (6mm structure) as an example, the magnitude of the longitudinal velocity is found to be $\sqrt{c_{11}/\rho}$ and shear ones are $\sqrt{(c_{11}-c_{12})/2\rho}$ and $\sqrt{c_{44}/\rho}$, details given in Appendix A.

Surface wave A surface acoustic wave is such a wave in which propagation is confined close to the surface of a medium and attenuates along the depth. The velocity of the SAW is always less than that of bulk waves in a given material. The fact remains that the particles found at the free surface only exert forces of elastic cohesion on one side, whereas bulk waves affect particles which are surrounded on all sides within the medium.

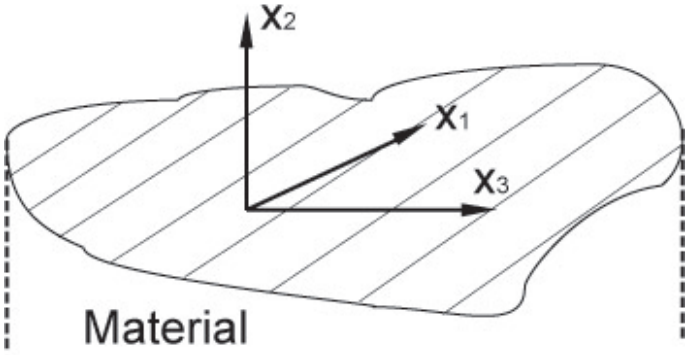

Figure 2.5: Material medium bound by a free, infinite surface defined by the plane x_1-x_3.

Consider a material bound on one side by a plane free surface normal to the axis x_2. The task is to find a solution to equation (2.21) in the form of a traveling wave of displacement $\boldsymbol{u}$ without attenuation in the direction (s_1,0,s_3) from the plane of the free surface and whose amplitude decreases exponentially as a function of x_2 in the material, that is

$$u_i = U_i e^{-(\alpha+j\gamma)x_2} e^{j\Omega(t-s_1x_1-s_3x_3)} \tag{2.25}$$

with α positive in the region $x_2 \leq 0$. In order to be consistent with expressions in bulk wave, equation (2.25) can be rewritten in the form

$$u_i = U_i e^{j\Omega(t-\frac{\hat{s}\cdot\boldsymbol{r}}{v})} \tag{2.26}$$

where $\hat{s}$ is the unit vector indicating the direction of $\boldsymbol{s}$ and v is the acoustic velocity. And $\hat{s}_2$ in the expansion of the scalar products $\hat{s}\cdot\boldsymbol{r}$ no longer contribute the propagation direction but takes

$$\hat{s}_2 = \frac{\gamma - j\alpha}{v\Omega} \tag{2.27}$$

The solution of the fundamental equation (2.21) is identical in form to that of the corresponding equation for bulk waves in an infinite medium and leads to the scalar equation

$$\det(c_{ijkl}\hat{s}_j\hat{s}_l - v\rho\delta_{ik}) = 0 \tag{2.28}$$

Given the direction of propagation of SAW defined by $\hat{s}_1$ and $\hat{s}_3$ and the value of v being fixed to begin with, from equation (2.28) is obtained a six degree equation of $\hat{s}_2$ for real coefficients. For each value of v, generally, 3 pairs of conjugated numbers is achieved. Only those solutions which have positive imaginary parts can make it possible for SAW propagation.

Therefore, for a SAW propagating along direction ($\hat{s}_1$, 0, $\hat{s}_3$) and a particular phase velocity v, the general solution is a linear combination of the type

$$u_i = \sum_{p=1}^{3} a_p U_i^{(p)} e^{j\Omega(t - \frac{\hat{s}_1 x_1 - \hat{s}_2^{(p)} x_2 - \hat{s}_3 x_3}{v})} \tag{2.29}$$

where a_p are the weights of the three SAW partial solution which is still unknown. Equation (2.29) must satisfy the boundary conditions on the free surface of the material at $x_2 = 0$. Since there is no material in the region $x_2 > 0$, the stresses must vanish in the plane x_1x_3

$$T_{3j} = \frac{1}{2} c_{3jkl} \left(\frac{\partial u_k}{\partial x_l} + \frac{\partial u_l}{\partial x_k} \right) = 0 \tag{2.30}$$

Substituting equation (2.30) into equation (2.29) yields three linear equations for a_p which is to be determined. In order to arrive at non-trivial solutions the associated determinant must be zero, which can be satisfied with proper values of acoustic velocity v. The searching of the magnitudes of v can be proceeded by a computer programme. After the acoustic velocity is found out, a proper set of a_p can then be obtained.

2.3 SAW in Multilayer Piezoelectric Medium

With the increasing interest in mobile telecommunication systems, the demands for higher frequency SAW devices require utilization of materials with higher acoustic velocities. Unfortunately, a material of high acoustic velocity may not be proper for acoustic wave excitation, i.e. nonpiezoelectric. But one can realize this hybrid purpose by grow piezoelectric thin films on high velocity nonpiezoelectric substrate to launch efficiently high speed SAW. This is one reason for the motivation of investigations of multilayer acoustic structure. The simulation of SAW properties of the layered system will be demonstrated in this section using the transfer matrix method, developed by Adler and Fahmy in 1973, [43].

Semi-infinite medium Consider the coordinated system illustrate in figure 2.5. The propagation direction of the SAW can be chosen arbitrarily in the x_1-x_3 plane and in this section it is supposed to be along x_1-axis, i.e. $(s_1, 0, 0)$. Compared with the discussion presented in the previous section, the difference in this case is the material is piezoelectric. Hence the constitutive relationship is in the form of equation (2.16) instead of (2.13).

$$\begin{aligned} T_{ij} &= c_{ijkl} S_{kl} - e_{kij} E_k \\ D_i &= e_{ikl} S_{kl} + \epsilon_{ik} E_k \end{aligned} \tag{2.31}$$

The coupling between the elastic fields and electric fields in piezoelectric material causes the appearance of $\boldsymbol{E}$ and $\boldsymbol{D}$. Given the fact that the acoustic velocities are much slower than the velocity of electromagnetic waves, the quasi-static approximation may be used. In this case the electric field is taken to be

$$E_i = -\frac{dV}{dx_i}; \quad i = 1, 2, 3 \tag{2.32}$$

and V is the electronic potential varying in the same form as mechanical elongation when the elastic waves propagate

$$\begin{aligned} \boldsymbol{u} &= \boldsymbol{U} e^{j\Omega(t - \boldsymbol{s}\cdot\boldsymbol{r})} \\ V &= V_0 e^{j\Omega(t - \boldsymbol{s}\cdot\boldsymbol{r})} \end{aligned} \tag{2.33}$$

Following the conventional approach, as presented in the previous section, one can solve the acoustic propagation problem by taking the electronic potential V and the particle displacement $\boldsymbol{u}$ of components u_1, u_2 and u_3 as unknown variables. This

is the smallest number of variables one can choose in a piezoelectric material and a set of second-order derivative equations are to be solved. Substituting equation (2.33) into the motion dynamic equation (2.21) and the constitutive equation (2.31) results in an equation like (2.28), for a chosen direction of propagation, leading to the three acoustic velocities, the corresponding particle displacements and the electronic potential. In half-spaces, plates and layer structures, the continuity of particle displacements (or velocities) and normal stresses are boundary conditions that must be satisfied at each interface. As a result, even for a nonpiezoelectric material, six additional constraints must be satisfied for each additional layer and the computational complexity of a problem becomes prohibitive for even a modest number of layers.

Alternately, the approach in this section is to have a first-order derivative equation and to have as variables those field quantities that must be continuous at interfaces. In this case the interfacial boundary conditions can be satisfied in an extremely simple way. Instead of four variables of electronic potential and mechanical displacements, choose eight independent variables of which the quantities must be continuous at material interfaces:

$$\boldsymbol{\tau} = [T_{12}\ T_{22}\ T_{32}\ D_2\ v_1\ v_2\ v_3\ \phi]^t \tag{2.34}$$

and similarly with equation (2.33), each of them are supposed in the form of

$$F(\boldsymbol{r}, t) = C_i e^{-(\alpha+j\gamma)x_2} e^{j\Omega(t-s_1 x_1)} \tag{2.35}$$

where s_2 still takes the form of $s_2 = (\alpha + j\gamma)\Omega$, $s_1 = 1/v_R$ and v_R is the velocity of SAW propagating along x_1-axis. For convenience, the column vector τ is written as transposes of row vectors.

In equation (2.34) $\mathbf{T}_{i2}$ is the stress normal to the boundary plane, D_2 is the normal electrical displacement, v_i is the partial velocity

$$v_i = \frac{du_i}{dt} = j\Omega u_i \tag{2.36}$$

and

$$\phi = \frac{dV}{dt} = j\Omega V \tag{2.37}$$

This set of 8 variables is sufficient independent ones and all other variables can be expressed in terms of them by solving the motion dynamic equation and the

constitute equation of a material.

For the coordinate system given in figure 2.5 and the propagation direction chosen along x_1-axis, the problem is two-dimensional since there are no variations in the x_3-axis and $d/dx_3 = 0$ $d/dx_2 = -j\Omega s_2$ and $d/dx_1 = -j\Omega s_1$. The differential equation achieved from the motion dynamic equation and constitute equation at angular frequency Ω using the eight-component vector $\boldsymbol{\tau}$ can be written (See Appendix B)

$$\frac{d\boldsymbol{\tau}}{dx_2} = j\Omega A\boldsymbol{\tau} \tag{2.38}$$

where A is a 8×8 matrix, a function of the slowness component s_1, which is to be determined, and the material constants rotated to the coordinate system of figure 2.5. No matter in half-space or multilayer structure equation (2.38) must be satisfied in each material and $\boldsymbol{\tau}$ must be continuous at each interface. To obtain the nontrivial solution the associated determinant must be zero, that is

$$\det(A + s_2 I) = 0 \tag{2.39}$$

with I being a unit matrix.

For a given s_1 satisfying equation (2.39), eight eigenvalues of s_2 for the matrix A can be obtained, of which four have positive imaginary part and are the proper solution for the SAW. The general solution is thus the linear combination of the four partial waves

$$\boldsymbol{\tau} = QP(x_2)\boldsymbol{a}e^{j\Omega(t-s_1x_1)} \tag{2.40}$$

and

$$P \equiv e^{-j\Omega s_2 x_2} \tag{2.41}$$

where P is the matrix transition (a 4×4 diagonal matrix) corresponding to the four eigenvalues of s_2 having positive imaginary part, and Q is an 8×4 matrix, each column is the associated eigenvector for each eigenvalue; $\boldsymbol{a}$ is a 4 element column vector being the weights of each eigenmodes (partial waves). The solving of appropriate weights $\boldsymbol{a}$ requires the boundary conditions to be matched at the interface.

Two classes of conditions are considered: metalized surface, and free space (in contact with air). In either case the normal stress T_{i2} must vanish at the surface, i.e.

$$T_{i2} = 0 \tag{2.42}$$

Besides, the electric potential φ vanishes too in the first case

$$V = 0 \tag{2.43}$$

For convenience, rewrite the state variable $\boldsymbol{\tau}$ in the form of

$$\tau' = [T_{12}\ T_{22}\ T_{32}\ \phi\ v_1\ v_2\ v_3\ D_2]^t$$

and the boundary condition with metallized surface indicates

$$\boldsymbol{\tau}'(1:4) = 0 \tag{2.44}$$

where the colon means the first four elements of the column vector $\boldsymbol{\tau}$. In order to find proper values of s_1, which can make this equation satisfied, the determinant of Q'_u, the upper half of the matrix Q', of which the $4th$ row and $8th$ row have been swapped, must be zero:

$$\det Q'_u = 0 \tag{2.45}$$

In the second case, the absence of free charges in the region $x_2 > 0$ (air) leads to a distribution of nonzero electronic potential, which satisfies Laplace equation

$$\frac{\partial^2 V}{dx_1^2} + \frac{\partial^2 V}{dx_2^2} = 0 \tag{2.46}$$

This gives the potential in the form

$$V^{(air)} = V_0 e^{\Omega s_1 x_2} e^{j\Omega(t - s_1 x_1)} \tag{2.47}$$

with V_0 being the potential amplitude. From equation (2.47) combined with equation (2.32) is obtained the expression of the normal electrical displacement in air

$$D_2^{(air)} = -\Omega \epsilon_0 s_1 V \tag{2.48}$$

or

$$D_2^{(air)} = j s_1 \epsilon_0 \phi \tag{2.49}$$

In equation (2.49) the definition of $\phi = j\Omega V$ has been used. Since there is no free charges at the surface $x_2 = 0$, the continuity of normal electrical displacement leads to

$$D_2 = D_2^{(air)} \tag{2.50}$$

Rewrite state variable $\boldsymbol{\tau}$ in the form of $\tau'' = [T_{12}\ T_{22}\ T_{32}\ D_2 - D_2^{(air)}\ v_1\ v_2\ v_3\ \phi]^t$, and the boundary condition with free surface indicates

$$\boldsymbol{\tau}''(1:4) = 0 \tag{2.51}$$

Satisfying equation (2.51) requires the determinant of the upper half of Q'' being zero, that is

$$\det Q_u'' = 0 \tag{2.52}$$

and Q'' is defined as a matrix with the same elements as Q except its $4th$ row replaced by the original $4th$ row minus its $8row$ times $js_1\epsilon_0$ (equation (2.49)).

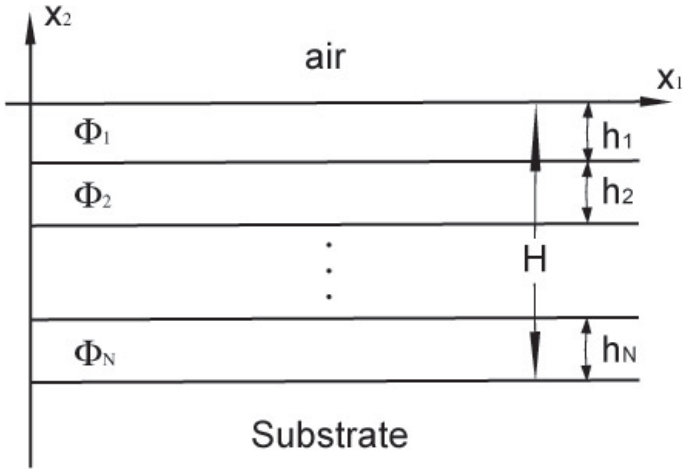

Figure 2.6: Multilayer system of N layers of films of thickness $h_1, h_2, \cdots h_N$ on the substrate.

Multilayer structure Consider the coordinate system and the multilayer structure illustrated in Fig. 2.6, still taking x_1-axis as the propagating direction of SAW. Each layer is homogeneous characterized by the material stiffness c, piezoelectric constant e and permittivity ϵ with respect to this coordinates system. From linear system theory the solution $\boldsymbol{\tau}$ to equation (2.38) satisfies, [44]

$$\begin{aligned} \boldsymbol{\tau}(x_2 + h) &= e^{j\Omega A h}\boldsymbol{\tau}(x_2) \\ &= \Phi(h)\boldsymbol{\tau}(x_2) \end{aligned} \tag{2.53}$$

where $\Phi(h)$, the matrix exponential, is the transfer matrix from an arbitrary depth to a distance h away along the y-axis in the same material. For a layered structure, each layer has its own system matrix A and satisfies the same type of state function and hence has an associated transfer matrix Φ. Since the elements of the vector $\boldsymbol{\tau}$ are chosen to be continuous across interfaces, the boundary conditions are satisfied naturally at each interface and hence $\boldsymbol{\tau}$ at the uppermost interface ($\boldsymbol{\tau}_u$) can be linked to the one at the lowest interface ($\boldsymbol{\tau}_l$) by the matrix product of the layer transfer matrices. With a structure of N layers, the total transfer matrix is given by

$$M = \Phi_1(h_1)\Phi_2(h_2)\cdots\Phi_{N-1}(h_{N-1})\Phi_N(h_N) \tag{2.54}$$

and naturally

$$\boldsymbol{\tau}_u = M\boldsymbol{\tau}_l \tag{2.55}$$

where $h_1 \cdots h_N$ is the thickness for each layer, as shown in figure 2.6, and $\Phi_1 \cdots \Phi_N$ are the transfer matrices characterized by the system matrix A of each layer.

It is noted that in constructing equation (2.55) all interfacial boundary conditions are satisfied and the interface $\boldsymbol{\tau}$ variables have been eliminated. The entire layered structure thus can be treated as an equivalent single layer with M as defined above, the matrix that relates the two terminal τ across the entire multilayer.

To obtain the total system solution requires satisfying the appropriate boundary condition at the remaining two interference $x_2 = 0$ and $x_2 = H$. Satisfying the condition at the interface with the substrate, the state variable $\boldsymbol{\tau}$ at $x_2 = H$ is expressed

$$\tau_l = MQP(x_2)\boldsymbol{a}e^{j\Omega(t - s_1 x_1)} \tag{2.56}$$

At the uppermost interface, if the surface is metallized, the boundary condition (2.45) needs to be rewritten

$$\det(MQ')_u = 0 \tag{2.57}$$

and if the surface is free space, the boundary condition (2.52) is written as

$$\det(MQ'')_u = 0 \tag{2.58}$$

In equation (2.57) and (2.58) the definition of Q' and Q'' stays the same as the semi-infinite case and the suffix u means the upper half of the 8×4 matrix MQ' or MQ''.

A computer programme has been built to proceed a search for proper values of s_1 (reciprocal of the acoustic velocity) to satisfy the associated boundary conditions. The particle displacement polarization and the electronic potential distribution can thus be obtained at the same time. The most attractive advantage of Adler's transfer matrix method is the boundary condition at interfaces of a multilayer system can be taken into account in an extremely simple way. The calculation complexity does not increase remarkably as the layer number increases. An example of SAW propagation in a multilayer structure of GaN/Sapphire system will be demonstrated in section 2.5.

2.4 Electrical Excitation of SAW: IDT

A transducer is an important component in acoustic devices as it interfaces between the electrical circuit and the acoustic waves both as a transmitter (electrical $\rightarrow$ acoustic) and as a receiver (acoustic $\rightarrow$ electrical). The planar transducer, so called Interdigital Transducer (IDT) is a set of parallel metal fingers with particular electrical connection designed to excite a surface acoustic wave in a substrate. IDT was firstly invented by White and Voltmer [46] in 1965. Before that, the bulk wave was the main way people designed acoustic filters and resonators, etc., using a metal plate as a transducer bounded with a piezoelectric crystal, for example, [45]. There are in fact many other types of transducers for surface waves, [39], but most of them are not compatible with planar technology, and are not used in devices for electronics application.

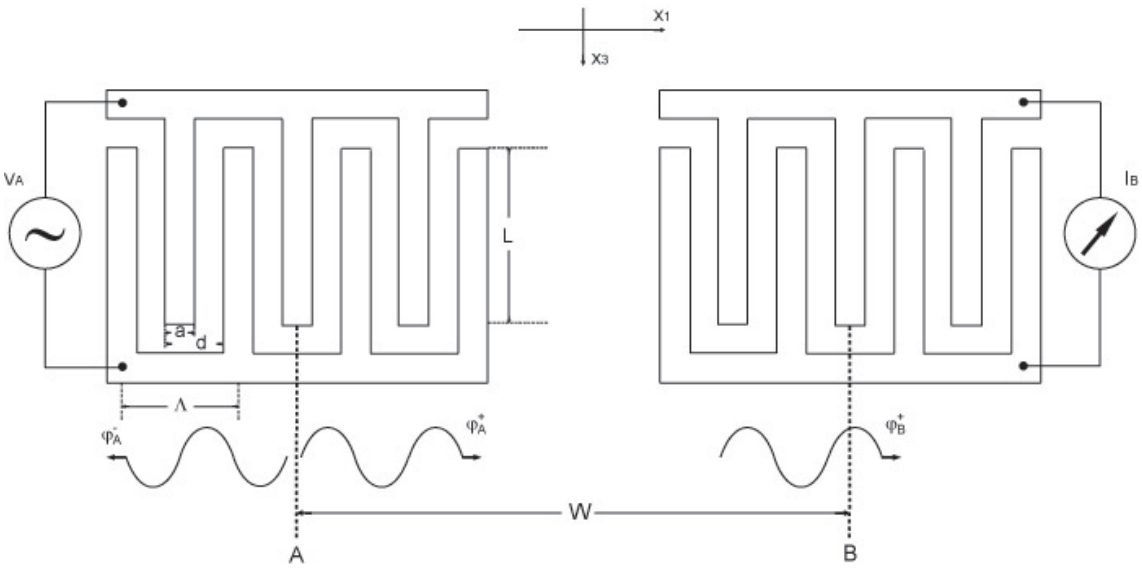

Figure 2.7: Schematics of a interdigital transducer transmitter and receiver.

A typical connection type of IDT is illustrated in figure 2.7. The parallel electrodes are of uniform length connected alternately to two metal bus-bars, half of them positively connected to the power source and the other half grounded. More complex designs of IDT have been developed enabling the device to process an applied electrical signal in a prescribed manner, for example, to reject unwanted frequency components, which is very useful in signal processing devices. The electrode lengths and pitches can be varied, as shown in figure 2.8a, to alter the frequency response of the IDT. Different connections of electrodes can also be applied to reduce the internal reflection when SAW propagates through the electrodes, as shown in figure 2.8b. These IDT designs can referenced in the literature, for instance, [47]∼[49], but they will not be considered in this monograph.

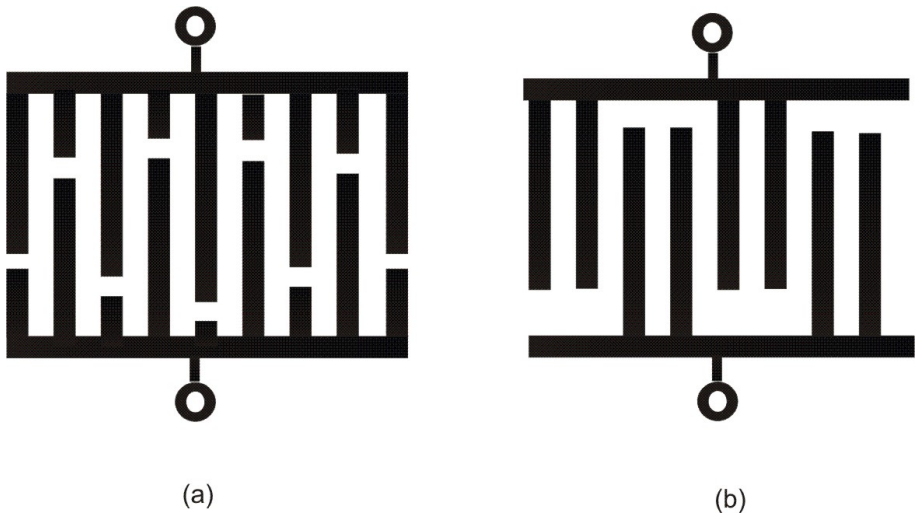

Figure 2.8: a) IDT electrodes of varied length; b), IDT electrodes splited into two parts to reduce reflection effects.

Mechanism of SAW generation by an IDT The simplest type of surface wave device is a delay line employing a transmitter IDT and a receiver IDT, one to generate the waves and one to receive them, as shown in figure 2.7. An electrical signal (V) applied to the transmitter transducer A is converted to a surface acoustic wave. A short-circuit current I is generated when the propagating acoustic wave reaches the receiver after a delay. While a SAW is generated, its particle displacement $\boldsymbol{u}$ and the electronic potential at the surface are coupled through the constitutive equation. Given a material and structure, the elastic displacements and surface potential of SAW at a particular frequency can be determined using Adler's method presented in the previous section. In this section the surface potential will be used as a measure of the amplitude of the SAW. The displacement $\boldsymbol{u}$, of course, can be used with equal justification. However, since the interaction of surface waves with electrical circuits will be discussed, choosing the surface potential as the amplitude eliminates repeated interaction between mechanical and electric quantities. Besides, in order to avoid confusion, the surface potential is denoted by φ instead of V (which is the electrical voltage applied across the IDT here).

It is the piezoelectric effect that converts an electrical signal to an acoustic wave, or vice versa. With an oscillatory voltage applied between the two metal bars, the transducer generates an electric field which is spatially periodic, with its period Λ, equal to the spacing of the electrodes connected to one of the bus-bars. A corresponding alternating strain pattern via the piezoelectric effect is thus ex-

cited. Efficient coupling to surface waves occurs, i.e., the mechanical vibrations add constructively only if the transducer period Λ equals the elastic wavelength.

Indeed, any strain produced at time t by a pair of fingers, for a given polarity of the voltage, travels the distance during the half period $T/2$ at the speed v_R of the Rayleigh wave. At time $t + T/2$, the strain arrives under the neighbouring pair of electrodes, just when the voltage, which has changed sign, produces strain with the same phase. The strain due to the second pair of electrodes adds constructively to the first. The frequency of the vibrations is obtained by $f_0 = v_R/\Lambda$ (central frequency). If this frequency shifts away from this value, interference between elastic waves generated by the various pairs of fingers is not totally constructive and the resulting signals will be reduced.

Owing to the symmetry, the transducer generates surface waves equally in two opposite directions, which gives 3dB insertion loss of each IDT (transmitter or receiver). Usually, the waves in one direction are not needed and are eliminated by an absorber made by a lossy material applied to the surface. Unidirectional IDT have been developed to minimize losses, for instance, [50].

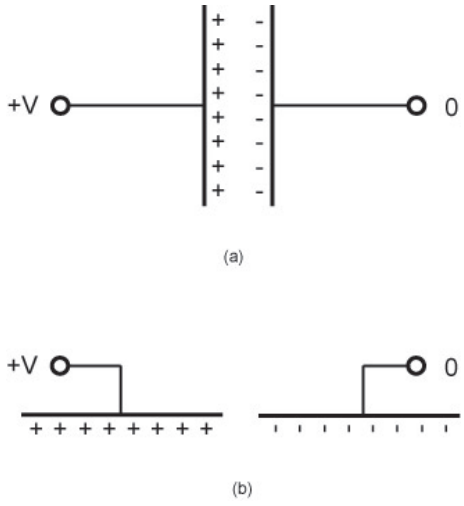

Figure 2.9: Surface charges distribution in a). parallel-plate capacitor and b) two adjacent electrodes of an IDT.

IDT static capacitance An IDT is basically a capacitor and charges appear on its electrodes when a voltage is applied to its terminals. The IDT can be derived from from the familiar parallel-plate capacitor by rotating the plates away from the each other until they are horizontal, figure 2.9. The value of the IDT's static capacitance C_0 depends on the particular type of connection of the electrodes and

and the metallization ratio η, defined as $\eta = a/d$. Notice that the capacitance does not depend on the the absolute value of the electrode spacing d or the electrode width a, but on the metallization ratio. Analogous with the parallel-plate capacitor, although the plate area depends on a and the plate separation depends on d, if doubling both a and d the capacitance does not change.

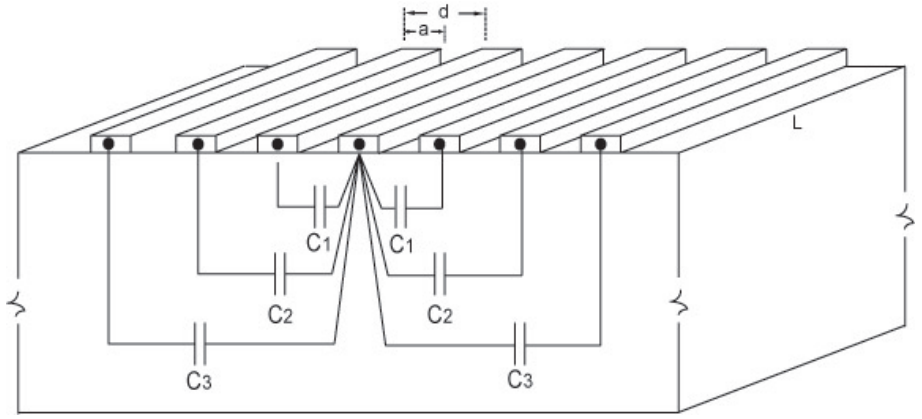

Figure 2.10: Capacitors connecting one electrode to its neighbours.

A schematic of the IDT in terms of capacitors C_1, C_2, $\cdots$, C_n connecting each electrode to its 1st, 2nd, $\cdots$, nth neighbour, figure 2.10. A simple result for the capacitances at $\eta = 0.5$ is given here without derivation, [51]:

$$C_n = \frac{4}{\pi} C_s L \frac{1}{4n^2 - 1} \tag{2.59}$$

with $C_s = \epsilon_p + \epsilon_0$, L being the width of electrodes, ϵ_p and ϵ_0 being the permittivity of the substrate and of air, respectively.

Consider a positively connected electrode in an IDT. It is connected through capacitors C_1, C_3, C_5, $\cdots$ to electrodes of the opposite polarity. The even capacitors connect it to an electrode with the same voltage and can be disregarded. So the capacitance for each positive electrode is the sum of all the odd capacitors. If N is the total number of positive electrodes,

$$C_0 = N \sum_{\text{odd } n} 2C_n = NC_sL \tag{2.60}$$

and the factor 2 accounts for the two capacitors, one on each side.

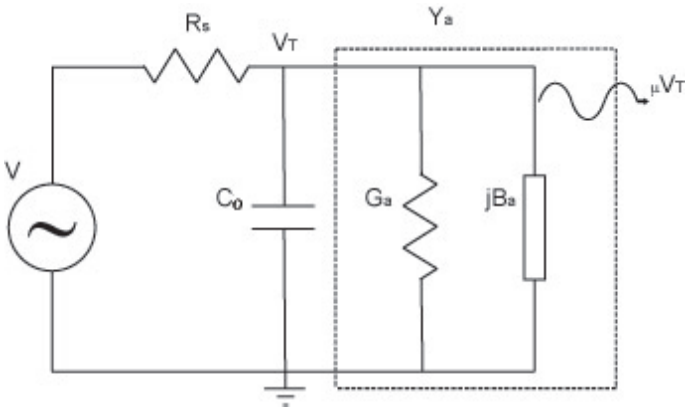

Figure 2.11: Circuit representation of an IDT.

IDT admittance The admittance of an IDT consists of two parts: the ordinary capacitive part, which has nothing to do with surface waves, $j2\pi fC_0$(f, acoustic frequency), and the acoustic admittance, $Y_a(f) = G_a(f) + jB_a(f)$, which arises from the interaction of the IDT with the waves generated by it, that is

$$Y(f) = j2\pi fC_0 + Y_a(f) \tag{2.61}$$

The real part of acoustic admittance $G_a(f)$ is called radiation conductance and the imaginary part $B_a(f)$ is called radiation susceptance. There is a simple circuit representation of the IDT, that can be used to describe the interaction with external circuit elements, as shown in figure 2.11. The voltage source has a source resistance R_s. The acoustic admittance occurs along with the generation of acoustic wave as a load. The relationship between the load voltage V_T and the SAW amplitude φ will be discussed next.

IDT frequency response The radiation conductance could be derived directly from the equivalent circuit method, [52]. However, it might be clearer for physical concepts involved, to define a transmitter response function $\mu(f)$ and a receiver response function $g(f)$ firstly:

$$\varphi_A^+ = \mu_A(f)V \tag{2.62}$$

$$I = g_B(f)\varphi_B^+ \tag{2.63}$$

Equation (2.62) describes the transmitting characteristics of the IDT at a frequency f, as shown in figure 2.7, that a voltage V applied to a transducer generates

a surface wave with an amplitude φ_A^+. A SAW beam is also generated to the left with amplitude φ_A^-, which is neglected for the present discussion. The suffix A indicates the potential φ_A is referenced to the centre of the IDT A. When the acoustic wave arrives at the receiver IDT B, the SAW beam generates a short-circuit current I which can be related to φ_B^+ through a receiver response function $g(f)$ describing the receiving characteristics at frequency f in equation (2.63). Again the subscript B is used to indicate the acoustic wave amplitude is now referenced to the centre of the transducer B. The wave amplitude at A and B are related by the propagation delay from A to B.

$$\varphi_B^+ = \varphi_A^+ e^{-j\Omega L/v_R} \tag{2.64}$$

where v_R is the SAW velocity along x_1-axis. Combining equation (2.62) to (2.64) yields the transconductance tansfer function G_{AB} of the delay line from transducer (port) A to B

$$G_{AB} = \frac{I_B}{V_A} = \mu_A(f) g_B(f) e^{-j\Omega L/v_R} \tag{2.65}$$

If now the roles of transducer A and B as transmitter and receiver are reversed, the transconductance transfer function from transducer (port) B to A is given

$$G_{BA} = \mu_B(f) g_A(f) e^{-j\Omega L/v_R} \tag{2.66}$$

where $\mu_B(A)$ is the transmitter response function of transducer B and $g_A(f)$ is the receiver response function of transducer B. By the principle of reciprocity,

$$G_{AB} = G_{BA} \tag{2.67}$$

Hence from equation (2.65) and (2.66),

$$\frac{g_A(f)}{\mu_A(f)} = \frac{g_B(f)}{\mu_B(f)} \tag{2.68}$$

Since the structures and frequency responses can be totally different for transducer A and B, this means that the $g(f)/\mu(f)$ is independent of the nature of the transducer. In fact, for any transducer, the receiver response is related to the transmitter response function by, [53]

$$g(f) = 2\mu(f) Y_0 \tag{2.69}$$

where Y_0 is the characteristic admittance of a SAW, a constant depending on materials with the SAW, beam width and the frequency given. The definition of Y_0 is given in Appendix C.

In the practical case, as shown in figure 2.11 for a transmitter IDT, the actual voltage V_T appears at the IDT terminals must be used, rather than the total voltage V when the voltage source has a source resistance R_s. The surface wave amplitude is given by μV_T rather than μV. As the surface waves propagate away from the IDT, power is transferred from the voltage source to the SAW and this is reflected as an admittance Y_a at the electrical terminals in parallel with the static capacitance C_0.

To describe an IDT one needs to know the function $\mu(f)$, the admittance $Y_a(f)$ and the insertion loss, etc., can all be derived therefrom. In order to compute this function of an IDT, however, the knowledge of a single electrode response function is useful.

To find the the single electrode response function μ_s, an analytic discussion can be done but the mathematics is somewhat complicated, [53]. Therefore just the approximated result is given here. It is found that μ_s does not only rely on frequency, but varies with the metalization ratio η as well. It is of the form

$$\mu_s(f,\eta) \simeq \mu_s(f_0,\eta)\sin\frac{\pi f}{2f_0}P_n(\cos\eta\pi) \tag{2.70}$$
$$n = \text{Integer}(f/2f_0)$$

where f_0 is the central frequency of an IDT, P_n is the n^{th} Legendre polynomial, n is defined as the integer part of $f/2f_0$ and the peak value $\mu_s(f_0,\eta)$ depends on the metallization η. The magnitude of $\mu_s(f_0,\eta)$ with different values of η is shown in figure 2.12. Particularly, for the metallization ratio of 0.5, it is noticed that $\mu_s(f_0)$ equals $0.85jK^2$ and this magnitude will be used in the example given in next section.

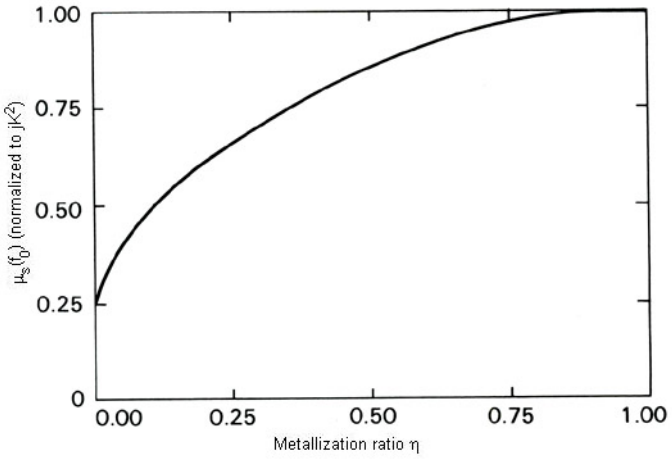

Figure 2.12: Variation of $\mu_s(f_0, \eta)$ with metallization ratio.

Transmission line modeling In order to find its frequency response function, the IDT can be modelled as a distributed current source of a surface charge density (see figure 2.9b) which is determined by solving the Poisson's equation, [53]. The amplitude of the SAW φ generated by IDT, is given by a summation of waves generated at different point along x_1-axis, figure 2.7. The frequency response function, therefore, can be obtained from its definition (2.62) and (2.63).

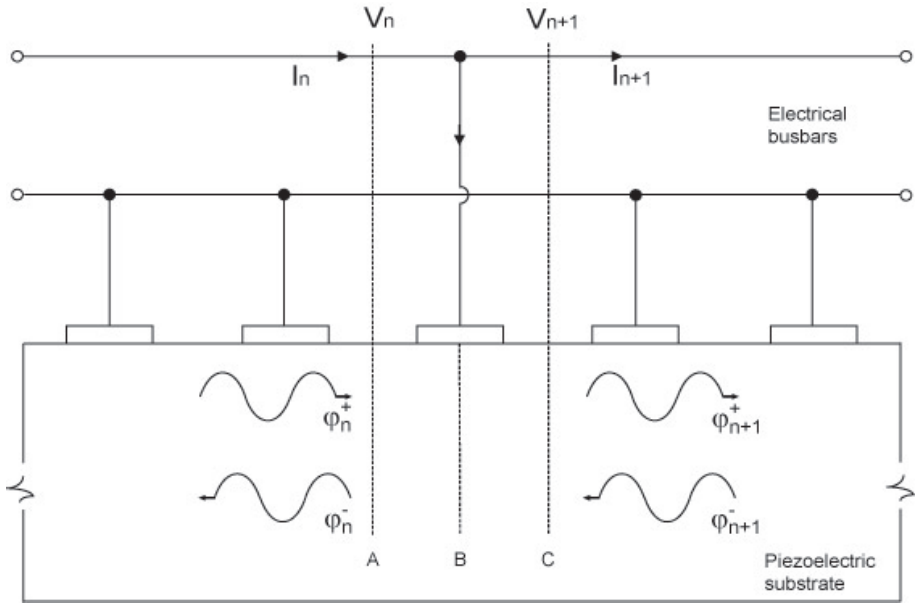

Figure 2.13: Modeling a single electrode in an IDT.

Alternatively, an IDT can also be analyzed numerically. A transmission line model has been developed to obtain the frequency response and the radiation admittance for a given IDT. There are two transmission lines in the modeling, one

acoustic transmission line and one electrical transmission line, illustrated in figure 2.13. Electric waves propagate along the two electrical busbars described by its voltage V and current I in the electrical transmission line, while the acoustic line is described by the wave amplitudes φ^+ and φ^- in the two directions. The electric waves and the acoustic waves have the same propagation velocity and the frequency response function given in equations (2.62) and (2.63) provide the linkage between the electrical and acoustic quantities.

In this model the electrodes are supposed to be periodically spaced and connected in the form in figure 2.7, but other electrical connection types (figure 2.8) can also be handled. Considering the nth electrode of the IDT, illustrated in figure 2.13, a transmission matrix $[T_n]$ connecting the field quantities at its output to those at its input can be defined

$$\begin{pmatrix} \varphi^+ \\ \varphi^- \\ V \\ rI \end{pmatrix}_{n+1} = T_n \begin{pmatrix} \varphi^+ \\ \varphi^- \\ V \\ I \end{pmatrix}_n \tag{2.71}$$

In order to obtain the transmission matrix T for the entire IDT, cascading the transmission matrices of all the N electrodes yields

$$T = T_1 T_2 \cdots T_{N-1} T_N \tag{2.72}$$

This T matrix relates the input quantities to the output quantities:

$$\begin{pmatrix} \varphi^+ \\ \varphi^- \\ V \\ I \end{pmatrix}_{N+1} = T \begin{pmatrix} \varphi^+ \\ \varphi^- \\ V \\ I \end{pmatrix}_1 \tag{2.73}$$

Once the transmission matrix is calculated numerically, all the desired terminal quantities for a transmitter driven from a voltage source V with a source impedance Z_g, can be obtained by applying the appropriate boundary conditions:

$$V_{N+1} = V_1 \tag{2.74}$$

$$I_{N+1} = 0 \tag{2.75}$$

$$\varphi^-_{N+1} = \varphi^+_1 = 0 \tag{2.76}$$

$$V = V_1 + I_1 Z_g \tag{2.77}$$

In order to find out the transmission matrix for a single electrode, one needs to study the relations among the field quantities of the electrode, V, I, φ^+ and φ^-, at its input and output port. This can readily be obtained using the parameters μ and g,

$$\varphi^+_{n+1} = \varphi^+_n P^2 + \mu_s V_n P \tag{2.78}$$

$$\varphi^-_{n+1} = \varphi^-_n P^{-2} + \mu_s V_n P^{-1} \tag{2.79}$$

$$V_{n+1} = V_n \tag{2.80}$$

$$I_{n+1} = I_n + g_s \varphi^+_n P + g_s \varphi^-_n P^{-1} \tag{2.81}$$

In this set of equations, P is a phase factor defined as

$$P = e^{-j\Omega s_1 \Lambda/4} \tag{2.82}$$

corresponding to acoustic propagation from A to B or B to C. This phase vector arises because μ and g are defined with the waves referenced to the electrode centre, as shown in figure 2.13 while the reference planes are shifted into the gap regions (plane A for φ_n's and plane B for φ_{n+1}'s).

With some algebraic manipulation, equation (2.78)$\sim$(2.81) can be rewritten in the form of a transmission matrix, equation (2.71), that is

$$\begin{pmatrix} \varphi^+ \\ \varphi^- \\ V \\ rI \end{pmatrix}_{n+1} = \begin{pmatrix} P^2 & 0 & \mu_s P & 0 \\ 0 & P^{-2} & -\mu_s P^{-1} & 0 \\ 0 & 0 & 1 & 0 \\ g_s P & g_s P^{-1} & 0 & 1 \end{pmatrix} \begin{pmatrix} \varphi^+ \\ \varphi^- \\ V \\ I \end{pmatrix}_n \tag{2.83}$$

μ_s and g_s are defined by equation (2.70) and (2.69) and are both positive for positive connecting electrodes, negative for negative connecting electrodes. Therefore the transmission matrix for a negative electrode is identical to the positive one but with opposite signs of μ_s and g_s. Using equation (2.72) the transmission matrix for an IDT is then achieved. The transmission function for this IDT can be rigidly solved with boundary conditions of equation (2.74)$\sim$(2.77):

$$\mu = \frac{\varphi^{+}_{N+1}}{V1} = -\frac{T_{23}}{T_{22}} \tag{2.84}$$

as well as the radiation admittance:

$$Y_a = \frac{I_1}{V_1} = -T_{43} + \frac{T_{42}T_{23}}{T_{22}} \tag{2.85}$$

Combined with the static capacitance of equation (2.60) the admittance of IDT, as defined in equation (2.61), is finally achieved.

Insertion loss Once the admittance of an IDT is derived, the insertion loss of these transducers can be derived. This is defined as the power delivered to the SAW as a fraction of the available power. The available power for a real source is the maximum power that can be drawn from it, that is, the power delivered to a load under matched condition:

$$P_{av} = \frac{V^2}{4Z_g} \tag{2.86}$$

The voltage across the IDT is thus less than V, as shown in figure 2.11:

$$V_T = \frac{V}{1 + Y(f)R_g} \tag{2.87}$$

and

$$Y(f) = j2\pi f C_0 + G_a(f) + jB_a(f) \tag{2.88}$$

can be attained from equation (2.85) and (2.60). Therefore the insertion loss for bidirectional transducers is:

$$\begin{aligned} \text{IL(in dB)} &= -10\lg \frac{\frac{1}{2}V_T^2 G_a}{V^2/4Z_g} \\ &= -10\lg \frac{2G_a Z_g}{(1+G_a Z_g)^2 + Z_g^2(2\pi f C_0 + B_a)^2} \end{aligned} \tag{2.89}$$

2.5 An Example of A Multilayer System of SAW

The simulation of excitation and propagation of a SAW in a multilayer system is demonstrated in this section. The formulas presented in the previous discussions of this chapter provides a theoretical evaluation to the characteristics of a given structure of a SAW device. Based on the consideration of the calculation consistence

for the FISOS, a system of GaN/AlGaN films on Sapphire substrate is taken as an example here (more discussions on acoustic and optical materials are available in Chapter 5). Some of the simulation results of this section, such as the acoustic velocity dispersion, are quite essential in the calculation of AO diffraction and thus used in Chapter 6, while the others are given here to be an estimation of the acoustic characteristics of the proposed structure.

Consider a layered structure composed of GaN/AlGaN films and sapphire substrate as illustrated in figure 2.14. Wurtzite GaN/AlGaN is considered grown on sapphire with its (001) plane parallel with sapphire's c plane, i.e. x_1-x_3 plane in the figure. An IDT with electrodes of uniform length deposited on the surface (x_1-x_3 plane) of the layers is used to excite SAWs. The IDT is chosen to be parallel with x_3 axis and hence the propagation direction of SAW is along x_1 axis. The detection of SAW is not considered in this case, therefore only a transmitter IDT is utilized.

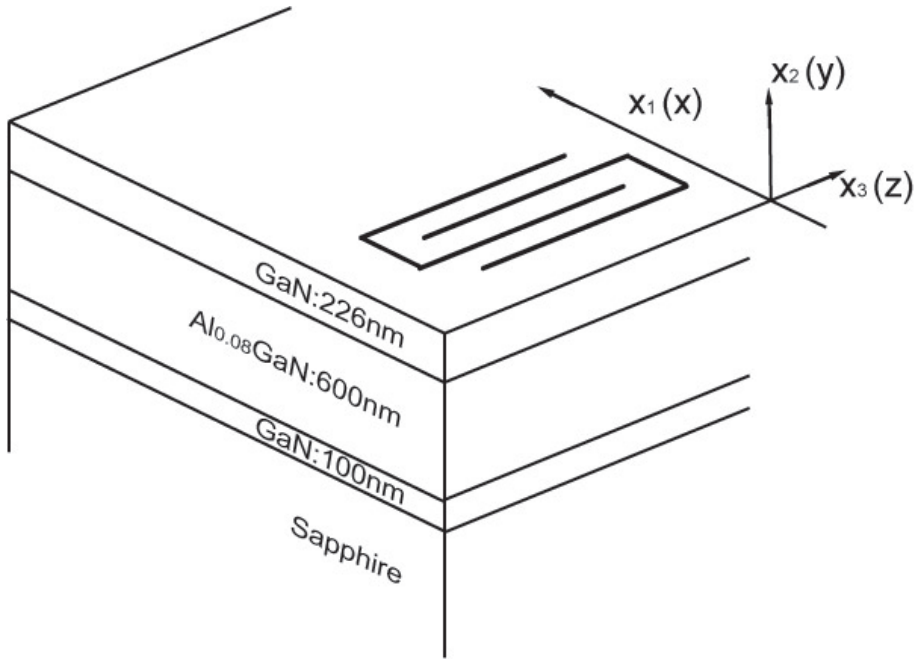

Figure 2.14: GaN multilayer system and deposited IDT. The layered material and thickness is as marked.

Elastic parameters of GaN and Sapphire can be found in table 5.2 in Chapter 5. Material constants for AlGaN film are approximated using Vegard's law through an interpolation between the corresponding values of the GaN and AlN materials. Matrix rotation is performed for tensor parameters before use to fit the coordinate system in figure 2.14.

The propagation velocity of SAW in the proposed structure can be investigated

using the transfer matrix method presented in section 2.3. Bulk acoustic wave or surface wave in a semi-infinite medium is nondispersive, as demonstrated in equation (2.24), because the velocity is independent of the frequency Ω. It is not the case, however, for SAW propagation in layered medium as revealed by equation (2.53), in which the phase term including acoustic frequency is concerned in each layer. The dispersive relation for the SAW velocity is illustrated in figure 2.15. The velocity of SAW in semi-infinite Sapphire (5557m/s) and GaN (3820m/s) are also shown for comparison. It is found the velocity tends to be close to the value in semi-infinite GaN when the frequency is higher. It is easily understood that the smaller wavelength implies the surface wave is much more confined inside the GaN film instead of penetrating into the substrate and hence the influence from the substrate of high acoustic speed is weaker. The dispersion relation presented here has a good agreement with the experimental data achieved by Deger (1998) in a Al_xGaN-on-sapphire system, [54].

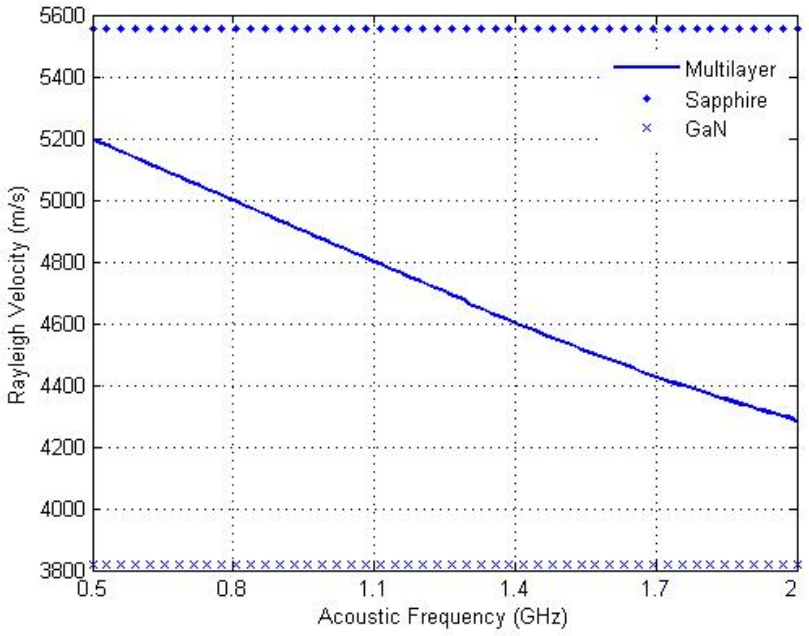

Figure 2.15: Dispersive velocity of SAW in multilayer medium

The electromechanical constant K^2 is also obtained for this structure using the same method. By solving the surface acoustic wave velocity at boundary conditions of metallized and free surface (see Appendix C), the electromechanical constant $K^2 = 6 \times 10^{-4}$ at frequency $f = 2GHz$.

The displacement of the SAW propagating at $f = 2GHz$ is also shown in figure

2.16. For a Rayleigh wave the displacement is polarized inside the x_1-x_2 plane and the oscillation along x_2 is found to lag the one along x_1 by $\pi/2$. It is noticed that the SAW is mostly confined inside the three-layer film and there is little motion at depth greater than that.

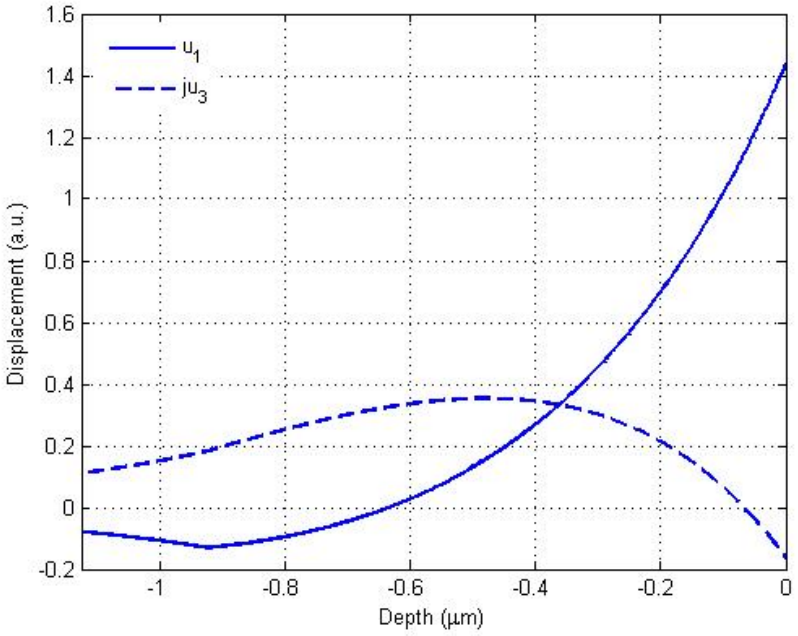

Figure 2.16: Displacements of SAW distribution along depth.

Using the transmission line model represented in section 2.4, one can achieve a variety of electrical properties of the IDT, of which the acoustic admittance and insertion loss are of interest. Given frequency $f_0 = 2$GHz, i.e. d=Λ=2.14μm, metallization ratio $\eta = 0.5$, IDT width $L = 100\mu$m and the number of positive electrodes $N = 100$, the radiation conductance varying with frequency is shown in figure 2.17 as well as the radiation susceptance in figure 2.18. It is useful to notice that the bandwidth of the used IDT is $2f_0/N = 40$MHz.

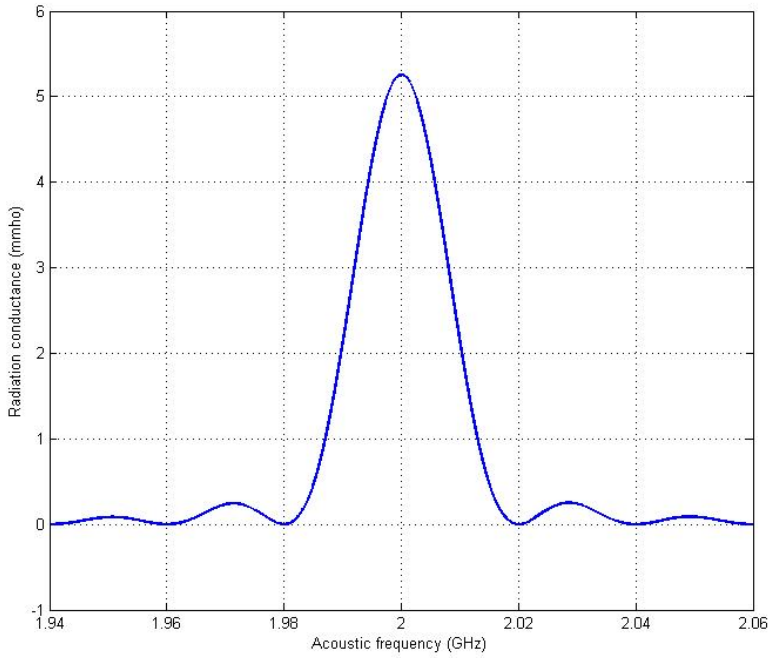

Figure 2.17: Radiation conductance of IDT varying with frequency.

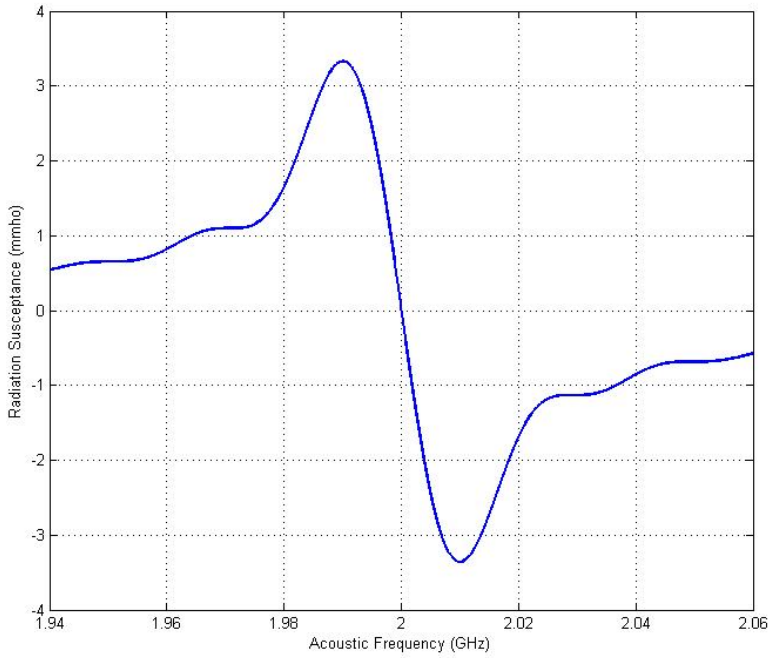

Figure 2.18: Radiation Susceptance of IDT varying with frequency.

The impedance of IDT can also be discussed. An IDT of a structure shown in figure 2.14 has an impedance $Z = 1/(G_a + j2\pi f_0 C_0)$. At the working frequency at 2GHz, the impedance of the IDT of width $L = 100\mu$m and $\eta = 0.5$ is evaluated

by varying with the number of pairs of electrodes. The real part and imaginal part of the impedance is illustrated in figure 2.19. When the number of electrode pairs rises, both the magnitudes of the real and imaginal parts of the impedance trend to zero. Since the magnitude of the IDT resistance is much smaller compared with the reactance, the blue curve in the figure shows a 30 times larger value for clarity. The very large capacitance of the IDT of a small number of electrode pairs will play a significant role when the impedance matching circuit is considered. As the electrode pairs are larger than 50, the magnitude of the IDT capacitance drops dramatically.

To match the impedance of the IDT to an electrical drive, inductive elements should be included in the design of impedance matching network. Conventionally, lumped elements are widely used to build the matching network, [56]. However, in high frequency SAW devices, it is difficult to realize the network design parameters because of the parasitic impedance of the inductor coil and the inductance of the capacitor leads. Alternatively, matching networks using planar microstrip technique with distributed elements has been proved to be capable to give better results, [57].

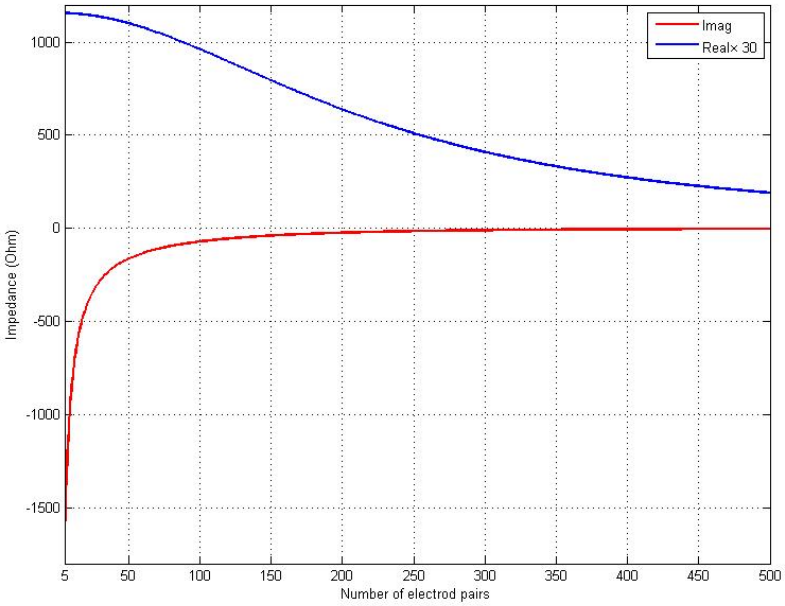

Figure 2.19: Impedance of IDT varying with the number of positive electrodes.

Finally, the insertion loss introduced into the device by an IDT is calculated by equation (2.89) again with the parameter configuration $f_0 = 2\text{GHz}$, $\eta = 0.5$, $L = 100\mu\text{m}$ and $N = 100$, figure 2.20. A minimal IL of 7.4dB is obtained of which 3dB comes from the nature of bidirection of IDT.

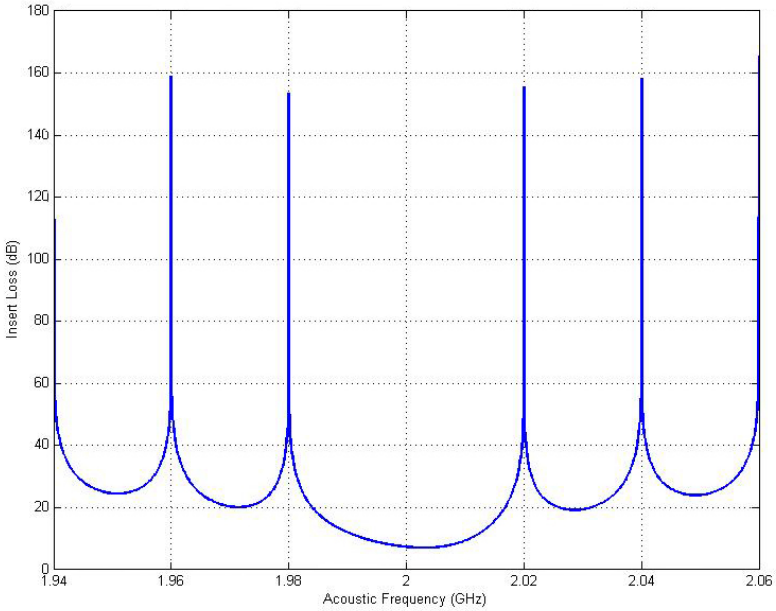

Figure 2.20: Insertion loss of IDT varying with acoustic working frequency.

Note that the reflections from the electrodes is not considered in the modeling of this section because of the lack of magnitude of the eflection coefficient for an IDT electrode.

Chapter 3

Electromagnetic Analysis with Grating

The periodic structure formed by acoustic wave described in section 1.2 is generalized to be a static grating since the acoustic velocity is quite slow compared with optical velocity. The acoustooptic effect is analyzed here as the interaction of an electromagnetic wave with an optical grating formed by the perturbed permittivity of material.

The material is assumed to be lossless. In other words, there are no free charges inside. The permittivity is assumed to be periodically perturbed along x-axis and stay uniform along y-axis with a grating vector $K = 2\pi/\Lambda$, as illustrated in figure 3.1. The profile of the permittivity in x-z plane is not necessarily sinusoidal. Other forms of profile of gratings can be made by different shapes of acoustic waves. TE polarized time-harmonic fields are employed since TM polarization will lead to similar results. The grating vector $\mathbf{K}$ is assumed to lie in the plane of optical incidence (x-z plane). If not, TE and TM polarizations will become coupled and can no longer be treated separately and independently but this case will not be considered in this monograph.

A rigorous analytic approach, developed by Gaylord and Moharam in 1985 [55], is discussed in this chapter to investigate the diffraction effect operated by a grating to an incident optical wave. Two extreme cases exist as shown in figure 3.2, with one quasi-normal incidence and one collinear interaction, of which both are broadly used in acoustooptic devices. As an example, the first case is analyzed in this chapter, but the second case can be readily analyzed through the same procedure.

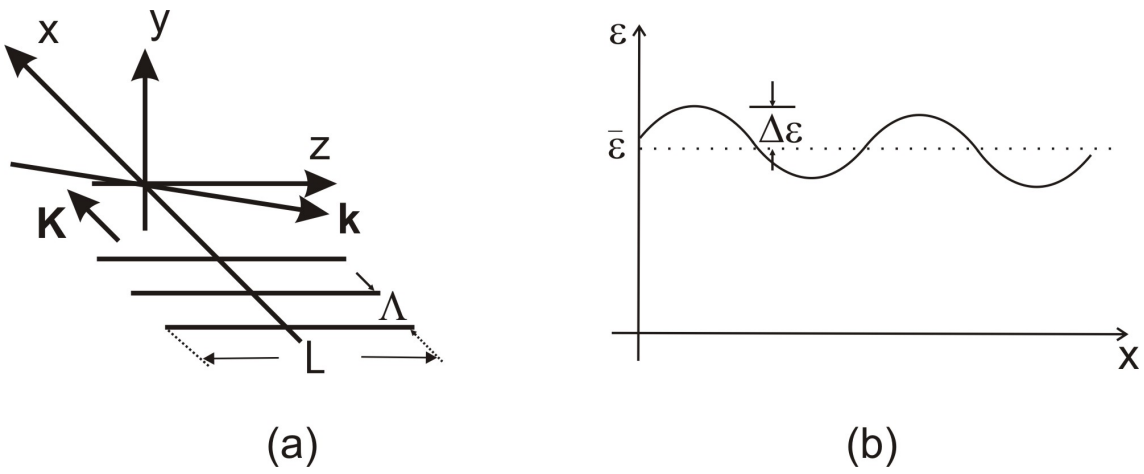

Figure 3.1: (a), schematics of interation between a electromagnetic field and a grating. **k**, electromagnetic wave vector; **K**, grating vector; Λ, grating period. (b) an example of perturbed permittivity profile.

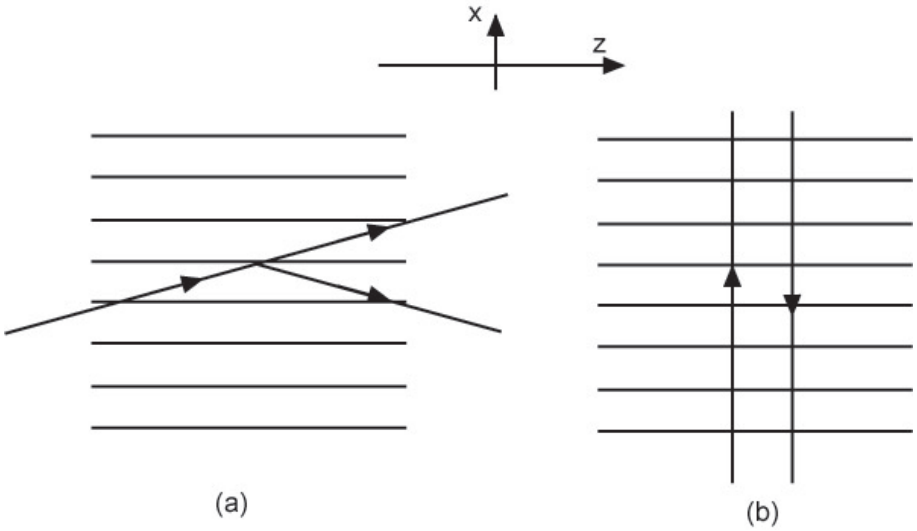

Figure 3.2: The optical waves inside a grating. (a), quasi-normal incidence; (b) collinear incidence.

Derived from this diffraction theory two methods can be employed corresponding to different expressions of the form of electric fields inside the grating. The coupled-wave method is demonstrated in section 3.2, in which the total field is considered to consist of infinite numbers of spatial harmonics each coupling with its adjacent neighbours. The well-known two-wave first-order coupled-wave theory (i.e. coupled-mode method used in Bragg regime) and the Raman-Nath theory (used in Raman-Nath regime) are demonstrated to be derived from the coupled-wave diffraction method. The modal method is discussed in section 3.3, in which the total field is treated as a summation of modes similar to what happens in a dielectric slab optical

waveguide. These two methods are in fact equivalent because they are just different expression of fields which satisfy the Maxwell's equations.

3.1 Electromagnetic Field Representation

A planar dielectric grating with a plane electromagnetic field going through is depicted in Figure 3.1. The permittivity stays a constant along y-axis, in x-z plane $\epsilon = \epsilon_r(x)\epsilon_0$ given by

$$\epsilon_r(x) = \begin{cases} \bar{\epsilon}_r & z < 0 \\ \bar{\epsilon}_r + \Delta\epsilon_r cosKx & 0 < z < L \\ \bar{\epsilon}_r & z > L \end{cases} \tag{3.1}$$

in the material, $\Delta\epsilon_r$ is the amplitude of the sinusoidal relative permittivity, and $\bar{\epsilon}_r$ is the original relative permittivity. For a electric field of TE polarization $E_y(x, z)$, following similar procedures described in Appendix D, the wave equation is

$$\nabla^2 E_y(x, z) + k_0^2 \epsilon_r(x) E_y(x, z) = 0 \tag{3.2}$$

where $k_0 = 2\pi/\lambda_0$ and λ_0 is the optical wavelength in vacuum. The electric field has no variation along the y-axis due to the assumption that the material is uniform in y direction.

Field representation inside the grating The electric field inside the grating may be expressed in terms of modes satisfying the wave equation (3.2). The total electric field may thus be written as

$$E_y(x, z) = \sum_{p=-\infty}^{+\infty} C_p E_p(x, z) \tag{3.3}$$

with p being the mode number and C_p being the mode weights, respectively. Each particular mode of the electric field, $E_p(x, z)$, may be assumed to be expressible as a product of two independent functions, i.e.,

$$E_p(x, z) = f_p(x) h_p(z) \tag{3.4}$$

where C_p is the mode amplitude. Upon substitution of the assumed solution (3.3) and (3.4) into the wave equation (3.2) and dividing by $E_p(x, z)$, separation of

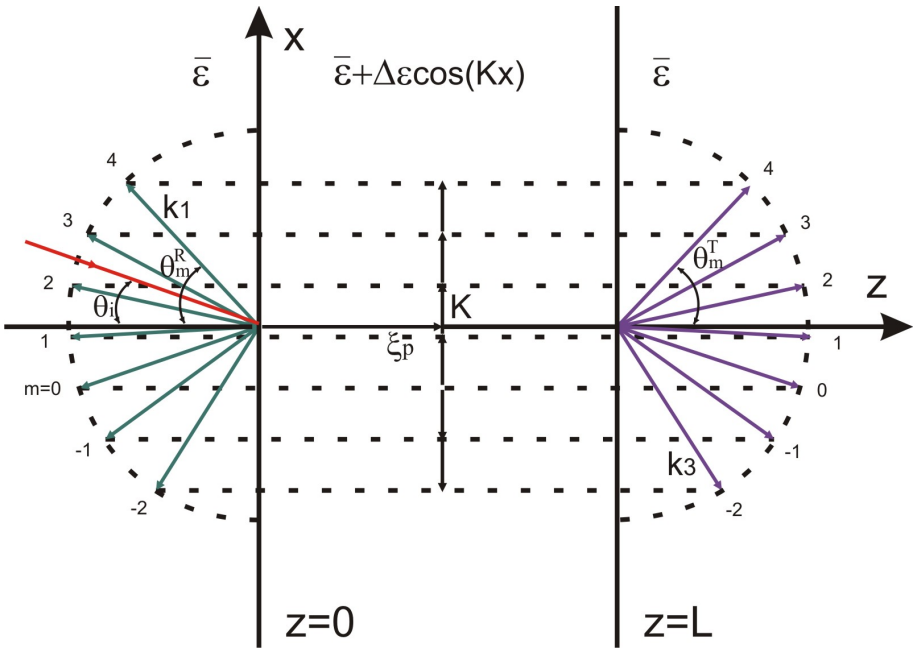

Figure 3.3: Schematics of wave vector diagram showing phase matching of subfield components of total field in the whole region. Red, incident field; green, reflected field; purple, transmitted field. For $-2 \leqslant m \leqslant 4$, propagating diffracted orders exist, whereas for $m \leqslant -3$ and $m \geqslant 5$, the subwaves are evanescent (cut off) outside the grating.

variables in the wave equation is achieved. Thus the x part and z part must be equal to a constant. Denote the constant as ξ_p^2 and thus the z variation involved parts become

$$\frac{d^2 h_p(z)}{dz^2} + \xi_p^2 h_p(z) = 0 \tag{3.5}$$

The form of the solution $h_p(z)$ is given

$$h_p(z) = e^{-j\xi z} \tag{3.6}$$

The x variation involved parts resulting from separation of variables are

$$\frac{d^2 f_p(x)}{dx^2} + (k_0^2 \epsilon_r(x) - \xi_p^2) f(x) = 0 \tag{3.7}$$

Since the perturbation of the permittivity in region $0 < z < d$ is periodic, the general solution was found using Floquet theory, [58],

$$f_p(x) = \Phi_p(x) e^{-j\beta_p x} \tag{3.8}$$

where β_p is a phase factor, a pure real number for loss-free medium, and $\Phi_p(x)$ is

periodic in x with period Λ, the same period as $\epsilon_r(x)$. Thus $\Phi_p(x)$ can be represented by a Fourier series

$$\Phi_p(x) = \sum_{m=-\infty}^{\infty} a_{mp} e^{-jmKx} \tag{3.9}$$

Consequently $f_p(x)$ may be written as

$$f_p(x) = \sum_{m=-\infty}^{\infty} a_{mp} e^{-j\beta_{mp}x} \tag{3.10}$$

where

$$\beta_{mp} = \beta_p + mK \tag{3.11}$$

Combining equation (3.4), equation (3.6) and equation (3.10), the electric field for each mode may thus be expressed as

$$E_p(x,z) = C_p e^{-j\xi_p z} \sum_{m=-\infty}^{\infty} a_{mp} e^{-j\beta_{mp}x} \tag{3.12}$$

Assuming the incident plane wave, with wave vector $\mathbf{k}_1$ and unit amplitude, is in the form of

$$E_i = e^{-j(\beta_0 x + k_{1z} z)} \tag{3.13}$$

where $\beta_0 = \sqrt{\bar{\epsilon}y} k_0 \sin\theta$ and $k_{1z} = \sqrt{\bar{\epsilon}_r} k_0 \cos\theta$. From the requirement of phase matching, tangential components of the electric fields on either side of the boundary $z = 0$ must be identical. The fact that the higher orders (i.e. $m \neq 0$) of the fields in the region $0 < z < L$ vanish in the absence of grating ($\Delta\epsilon y \to 0$), gives $\beta_p = \beta_0$. Therefore equation (3.11) is rewritten

$$\beta_m = \beta_0 + mK \tag{3.14}$$

Therefore the total field is

$$E(x,z) = \sum_{p=-\infty}^{\infty} A_p \sum_{m=-\infty}^{\infty} a_{mp} e^{-j\beta_m x} e^{-j\xi_p z} \tag{3.15}$$

This is a general form for the electric field inside the grating responding to a incident field in the form of equation (3.13).

Field Representation Outside the Grating Besides the incident plane wave as described in equation (3.13), the total field in the region $z < 0$ should include the consideration of the reflected field at the boundary. A decomposition of the reflected field can be achieved using Floquet theory again giving the total field

$$e^{-j\mathbf{k}_1\cdot\mathbf{r}} + \sum_{m=-\infty}^{\infty} R_m e^{-j\mathbf{k}_{1m}\cdot\mathbf{r}} \tag{3.16}$$

where $\mathbf{k}_{1m} = (k_{1x} + mK)\hat{x} + (\mathbf{k}_{1m}\cdot\hat{z})\hat{z}$ and R_m is the amplitude of the mth reflected field by boundary at $z = 0$ with wavevector $\mathbf{k}_{1m}$. Likewise, the total electric field in region $z > L$ is

$$\sum_{m=-\infty}^{\infty} T_m e^{-j\mathbf{k}_{3m}\cdot(\mathbf{r}-d\hat{z})} \tag{3.17}$$

where $\mathbf{k}_{3m} = (k_{3x} + mK)\hat{x} + (\mathbf{k}_{3m}\cdot\hat{z})\hat{z}$ and T_m is the amplitude of the mth transmitted field through the grating with wavevector $\mathbf{k}_{3m}$. Each mth subwave (order) inside the grating produces a corresponding mth field in the region outside the grating. The tangential components of wavevectors of each mth order in three regions must be equivalent separately for phase matching. That is

$$\mathbf{k}_{1m}\cdot\hat{x} = \mathbf{k}_{2m}\cdot\hat{x} = \mathbf{k}_{3m}\cdot\hat{x} \tag{3.18}$$

or

$$\beta_0 = k_{2x} = k_{3x} \tag{3.19}$$

The magnitudes of wavevectors outside the grating satisfy

$$\left|\mathbf{k}_1\right| = \left|\mathbf{k}_{1m}\right| = \left|\mathbf{k}_{3m}\right| \tag{3.20}$$

where $\left|\mathbf{k}_1\right| = \sqrt{\bar{\epsilon}}k_0$. Propagating directions of subwaves in either region can be achieved from equation (3.19) and 3.20 as shown in figure 3.3.

$$\sin\theta_m^T = \frac{\beta_0 + mK}{\sqrt{\bar{\epsilon}y}k_0} \tag{3.21}$$

$$\sin\left(\theta_m^R + \pi\right) = \frac{\beta_0 + mK}{\sqrt{\bar{\epsilon}_r}k_0} \tag{3.22}$$

The z components of wavevectors are given

$$\mathbf{k}_{1m} \cdot \hat{z} = -\sqrt{k_0^2 \bar{\epsilon}_r - \beta_m^2} \tag{3.23}$$

and

$$\mathbf{k}_{3m} \cdot \hat{z} = \sqrt{k_0^2 \bar{\epsilon}_r - \beta_m^2} \tag{3.24}$$

These quantities are either real (propagating wave) or imaginary (evanescent wave, cut-off). One example of propagating and cut-off waves in homogeneous media is shown in figure 3.3. The wavevectors have magnitudes $k_0\epsilon_r$, with which as radii two semicircles are shown in the figure. The allowed wavevectors in these regions must be phased matched to the boundary components of the space-harmonic component fields inside the grating, which is shown by the horizontal dashed lines in the figure. For the forward and backward fields and space harmonics inside the grating, the $m = -1$ to $+4$ fields exist as propagating diffracted orders in region 1 and 3. The $m \leq -2$ and $m \geq +5$ fields are evanescent.

So far the phase factors of electric field outside the grating have been analyzed above, leaving the amplitudes only unknown. Once fields inside the grating are solved R_m and T_m can be achieved rapidly by matching boundary conditions. In order to analyze the equation (3.15), two methods can be employed, coupled wave method and modal expansion method, which will be discussed in the following sections separately.

3.2 Coupled-wave Expansions

3.2.1 Rigorous Analysis

Interchanging the order of the summations in equation (3.15), the total field inside the grating may be rewritten

$$E(x,z) = \sum_{m=-\infty}^{\infty} e^{-j\beta_m x} \sum_{p=-\infty}^{\infty} A_p a_{mp} e^{-j\xi_p z} \tag{3.25}$$

Performing the summation over modes p, define the quantity $U_m(z)$

$$U_m(z) = \sum_{p=-\infty}^{\infty} A_p a_{mp} e^{-j\xi_p z} e^{jk_{1z}z} \tag{3.26}$$

which is a function of z only. the total field is therefore

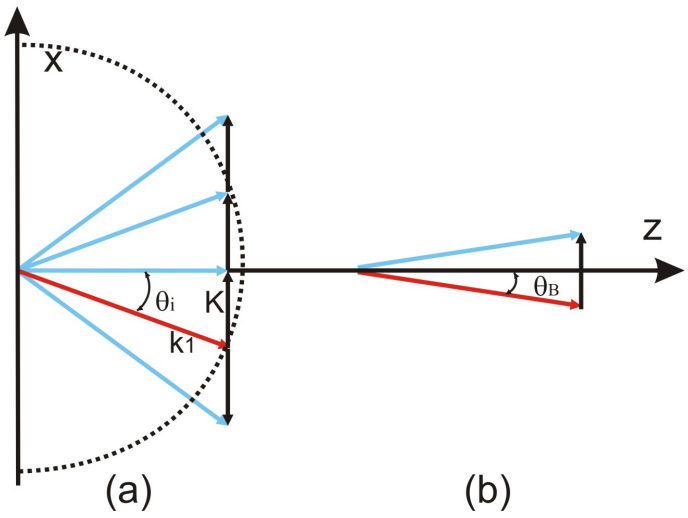

Figure 3.4: Illustration of wavevectors inside the grating for coupled-wave expansion. Red, incident field; blue, diffracted fields. (a), Multiple diffraction orders; (b), single diffraction order (Bragg regime).

$$E(x,z) = \sum_{m=-\infty}^{\infty} U_m(z) e^{-j\beta_m x} e^{-jk_{1z}z} \tag{3.27}$$

where the phase factor can be written in a compact vector form

$$-j(\beta_m x + k_{1z} z) = \beta_0 x + k_{1z} z + mKx = -j(\mathbf{k}_1 + m\mathbf{K}) \cdot \mathbf{r} \tag{3.28}$$

Equation (3.27) thus becomes

$$E(x,z) = \sum_{m=-\infty}^{\infty} U_m(z) e^{-j(\mathbf{k}_1 + m\mathbf{K}) \cdot \mathbf{r}} \tag{3.29}$$

where $\mathbf{k}_1$ is the wavevector of the incident wave in the region $z < 0$. From the viewpoint of equation (3.29), the presence of the grating imposes a decomposition of the incident field into an unlimited number of plane waves, namely space harmonics. The wave vector of each space harmonic is therefore the summation of wavevectors of the incident field and the grating. The amplitude of each space harmonic $U_m(z)$ is not constant but z dependent. One individual space harmonic does not satisfy the wave equation but the set of all harmonics does. Those harmonics are not independent and they cannot stand alone.

Substituting the field presentation (3.27) and the permittivity equation (3.1) into the wave equation equation (3.2) and performing the indicated differentiations gives

$$\sum_{m=-\infty}^{\infty} \{\frac{d^2U_m(z)}{dz^2} - 2jk_{1z}\frac{dU_m(z)}{dz} + \frac{1}{2}k_0^2\Delta\epsilon y(U_{m-1} + U_{m+1}) \\ -(m^2K^2 + 2m\beta_0K)U_m\}e^{-j\beta_m x}e^{-jk_{1z}z} = 0 \tag{3.30}$$

Notice the relationship $\cos Kx = \frac{1}{2}(e^{jKx} + e^{-jKx})$ is used in this derivation. Equation 3.30 represents an infinite series, the sum of which is zero. Each term in the series is an exponential multiplied by a coefficient. The coefficient is a function of z only. The x dependence is entirely in the exponential factor of each term. Since the exponentials are linearly independent, the coefficient of each exponential must individually be equal to zero. equation (3.30) therefore reduces to the set of coupled-wave equations

$$\frac{d^2U_m(z)}{dz^2} - 2jk_{1z}\frac{dU_m(z)}{dz} + \frac{1}{2}k_0^2\Delta\epsilon_r(U_{m-1}+U_{m+1}) - (m^2K^2+2m\beta_0K)U_m = 0 \tag{3.31}$$

This is an infinite set of second-order coupled difference-differential equations. By inspection, it is seen that the wave corresponding to each value of m (i.e. each space harmonic) is coupled to its adjacent ($m-1$ and $m+1$) space harmonics. There is no direct coupling between nonadjacent harmonics. Energy is coupled back and forth between each other in the grating. This property of coupling depends on the specific form of $\epsilon_r(x)$.

Those coupled-mode equations are constant-coefficient differential equations. Using state variable methods from linear systems analysis, a solution may be obtained in terms of the eigenvalues and eigenvectors of the coefficient matrix of the set of differential equations.

3.2.2 Approximate Theory

This section will deal with approximate grating diffraction theory. In order to simplify analyzes of the rigorous theory and obtain analytic formulas, a lot of possible approximations and assumptions can be made.

- neglect higher order waves
- neglect second derivatives of the field amplitudes
- neglect boundary effects

- small grating modulation approximation
- short wavelength approximation

These assumptions can be made based on either fixed gratings or gratings formed by an acoustic wave. One or a combination of several assumptions was used and many approximation theories have been built, like Two-wave Second-Order Coupled-wave Theory [59], Multiwave coupled-wave Theory [18][60], Two-wave First-order coupled-wave Theory [61], Optical Path Method [27], Raman-Nath Theory [18], etc.. In this section Two-wave first-order coupled-wave Theory (Bragg regime diffraction) and Raman-Nath theory (Raman-Nath regime diffraction) are demonstrated because of their wide applications. Both theories can be derived in physically intuitive methods separately, but it will be shown how they can be obtained from rigorous grating analysis.

Two-wave first-order coupled-wave Theory

This theory is called the coupled-mode theory in some texts (for example, Tsai, [62]). If only the zero- and first-order waves are retained ($m = 0, -1$ or $m = 0, +1$) , and all higher order waves and second derivatives of field amplitudes are both neglected, the coupled-wave equations (3.31) reduce to

$$\frac{dU_0(z)}{dz} = -j\kappa U_{-1}(z) \tag{3.32}$$

$$\frac{dU_{-1}(z)}{dz} - j\gamma U_{-1} = -j\kappa U_0(z) \tag{3.33}$$

where

$$\kappa = \frac{k_0^2 \Delta\epsilon_r}{4k_{1z}} \tag{3.34}$$

$$\gamma = \frac{K^2 - 2\beta_0 K}{2k_{1z}} \tag{3.35}$$

In this case the 0 order wave is the electric field in the original incident direction and the -1 order wave is the diffracted field. Those fields can be rewritten as

$$E_0(x, z) = U_0(z)e^{-j\mathbf{k}_1 \cdot \mathbf{r}} \tag{3.36}$$

$$E_{-1}(x,z) = U_{-1}(z)e^{-j(\mathbf{k}_1+\mathbf{K})\cdot\mathbf{r}} \tag{3.37}$$

The field amplitudes U_0 and U_{-1} are coupled though a quantity κ, the coupling coefficient. The solution to equation (3.32) and (3.33) are

$$U_0 = \frac{\kappa^2}{\kappa^2+\gamma_+^2}\left(e^{j\gamma_+ z} + \frac{\gamma_+^2}{\kappa^2}e^{j\gamma_- z}\right) \tag{3.38}$$

$$U_{-1} = -\frac{\kappa\gamma_+}{\kappa^2+\gamma_+^2}\left(e^{j\gamma_+ z} - e^{j\gamma_- z}\right) \tag{3.39}$$

where

$$\gamma_+ = \frac{\gamma}{2} + \sqrt{(\frac{\gamma}{2})^2+\kappa^2} \tag{3.40}$$

$$\gamma_- = \frac{\gamma}{2} - \sqrt{(\frac{\gamma}{2})^2+\kappa^2} \tag{3.41}$$

Solution (3.38) and (3.39) are obtained with boundary conditions $U_0(0) = 1$ and $U_{-1}(0) = 0$.

It is noticed that

$$U_0(z)U_0(z)^* + U_{-1}(z)U_{-1}(z)^* = 1 \tag{3.42}$$

so that the total optical power carried by both beams are conserved.

In this approximation (neglecting the higher order waves and second derivatives of field amplitudes), only two waves are considered, the incident wave ($U_0(z)$) and the diffracted wave ($U_{-1}(z)$), i.e., there are no reflected waves existing at $z = 0$. The absence of reflected waves implies the neglect of boundary effects, which transforms the problem to a filled-space problem (a grating filling the entire space). Consequently, the amplitude of the diffracted wave can be estimated through the quantity of the first order field amplitude (U_{-1}) calculated inside the grating region. The validity of this approximation is based on the fact that the reflected wave at at $z = 0$ is fairly weak since the grating caused by the acoustic wave is practically very weak, and that higher orders of diffracted waves are negligible in Bragg AO diffraction (section 1.2).

The diffraction efficiency is defined as the fraction of the power of the incident beam transferred in a distance L into the diffracted beam. Using equation (3.38) and (3.39) yields

$$\eta = \frac{I_d}{I_i} = \frac{U_{-1}(l)^2}{U_0(0)^2}$$
$$= \frac{4\kappa^2\gamma_+^2}{(\kappa^2+\gamma_+^2)^2}\sin^2(\sqrt{(\frac{\gamma}{2})^2+\kappa^2}L) \tag{3.43}$$

Particularly, when γ is set to be zero, i.e. $\beta_0 = K/2$ from equation (3.35), equation (3.43) could be significantly simplified. With this so-called Bragg condition, i.e. the field is incident in a precise angle (Bragg angle) defined as

$$\theta_B = \frac{K}{2k_1} = \frac{\lambda}{2\Lambda} \tag{3.44}$$

where λ is the optical wavelength in the region $z < 0$ (see figure 3.4), the diffraction efficiency reduces to

$$\eta = sin^2(\kappa L) \tag{3.45}$$

It can also be expressed in the form of acoustic power (see Appendix G)

$$\eta = \sin^2(\frac{\pi}{\lambda_0\cos\theta}\sqrt{\frac{M_2P_aL}{2H}}) \tag{3.46}$$

$$M_2 \equiv \frac{n^6p^2}{\rho v^3} \tag{3.47}$$

where P_a is the power carried by acoustic wave, L and H are the width and thickness of the acoustic wave, θ is the optical incidence angle, n is the average refractive index inside the grating, p is the photoelastic constant of the medium, ρ is the mass density, v is the acoustic velocity and M_2 is a figure merit measuring the Acoustooptic effect of materials, [32].

Although the two-wave first-order coupled-wave theory neglects higher order diffracted waves and second derivations of field amplitudes (and thus boundary effects), it nevertheless contains many of the basic features. When the incident angle is close to the Bragg angle, the AO diffraction problem can be described by this approximate model and the diffraction efficiency is estimated by equation (3.43). The oblique incidence is essential in Bragg diffraction whereas it is not in Raman-Nath regime diffraction described below.

Raman-Nath Theory

When an optical field goes though a grating, besides the single diffracted order (Bragg regime), the diffraction it undergoes may also be multiple orders, which was first reported by Raman and Nath in 1936 [18]. The Raman-Nath diffraction can be achieved from thin-phase-grating-approximation (see section 1.2) but the same conclusion can also be given directly from the grating theory.

If second derivatives of the field amplitudes are neglected but multiple order number m remains, the coupled-wave equation (3.31) reduce to the Raman-Nath diffraction equation

$$\frac{dU_m(z)}{dz} + j\frac{k_0^2\Delta\epsilon_r}{4k_{1z}}(U_{m-1} + U_{m+1}) - j\frac{m^2K^2 + 2m\beta_0 K}{2k_{1z}}U_m = 0 \tag{3.48}$$

The solution is

$$U_m(z) = e^{-j\frac{mKz\beta_0}{2k_{1z}}} J_m\big[\zeta\frac{\sin Kz\tan\theta_i/2}{KL\tan\theta_i/2}\big] \tag{3.49}$$

$$\zeta = -\frac{k_0^2\Delta\epsilon_r L}{2k_{1z}} \tag{3.50}$$

where θ_i is the incident angle.and J_m is the Bessel function of order m. The normalized intensity of the mth diffracted light at $z = L$ is given by

$$I_m = U_m(L)U_m^*(L) = J_m^2\big(\zeta\frac{\sin\chi}{\chi}\big) \tag{3.51}$$

$$\chi = KL\tan\theta/2 \tag{3.52}$$

where U_m^* is the complex conjugate of U_m.

3.3 Modal Expansion

Writing the total electric field (3.15) again here

$$E(x,z) = \sum_{p=-\infty}^{\infty} A_p \sum_{m=-\infty}^{\infty} a_{mp}e^{-j\beta_m x}e^{-j\xi_p z} \tag{3.53}$$

Using Fourier expansion (3.9), this equation can be written as

$$E(x,z) = \sum_{p=-\infty}^{\infty} A_p \Phi_p(x) e^{-j(\beta_0 x + \xi_p z)} \tag{3.54}$$

or in vector form

$$E(x,z) = \sum_{p=-\infty}^{\infty} A_p \Phi_p(x) e^{-j(\mathbf{k}_p \cdot \mathbf{r})} \tag{3.55}$$

where $\mathbf{k}_p = \beta_0 \hat{x} + \xi_p \hat{z}$. This expansion expresses the field inside the grating as a summation of modes, each of which satisfies the wave equation (3.2) and is independent from each other. Each mode is of the appearance of a traveling wave with a corresponding propagation constant $\mathbf{k}_p$ and amplitude $A_p \Phi_p(x)$ whose value varies along y periodically (note the term $\Phi_p(x)$ is periodic with the period Λ). Comparing with the set of inhomogeneous space harmonics stated in equation (3.27) one must note that the z component of propagation constant ξ_p is an unknown.

Substituting equation (3.54) into equation (3.2) and performing the indicated differentiations gives

$$\sum_{p=-\infty}^{\infty} A_p \frac{d^2 \Phi_p(x)}{dy^2} e^{-j(\mathbf{k}_p \cdot \mathbf{r})} + \sum_{p=-\infty}^{\infty} A_p (k_0^2 \epsilon_r(x) - \xi_p^2) \Phi_p(x) e^{-j(\mathbf{k}_p \cdot \mathbf{r})} = 0 \tag{3.56}$$

Considering the linear independence of the exponential terms $e^{-j(\mathbf{k}_p \cdot \mathbf{r})}$ and substituting equation (3.1) into this equation yields the term-by-term equation and then rewriting $f_p(x)$ in the form of infinite summation

$$\begin{aligned} -\sum_{m=-\infty}^{\infty} \Big\{ (\beta_m^2 + \xi_p^2) a_{mp} &- \frac{1}{2}\omega^2 \mu \Delta \epsilon_r a_{(m+1)p} \\ &- \omega^2 \mu \bar{\epsilon}_r a_{mp} \\ &- \frac{1}{2}\omega^2 \mu \Delta \epsilon_r a_{(m-1)p} \Big\} e^{-j\beta_m x} = 0 \end{aligned}$$

The linear independence of the exponentials ($e^{-j\beta_m x}$) is employed again and thus

$$\frac{1}{2}\Delta\epsilon_r \omega^2 \mu a_{(m-1)p} + (\omega^2 \mu \bar{\epsilon}_r - \beta_m^2 - \xi_p^2) a_{mp} + \frac{1}{2}\Delta\epsilon_r \omega^2 \mu a_{(m+1)p} = 0 \tag{3.57}$$

which can be rewritten

$$\frac{1}{2}\Delta\epsilon_r \omega^2 \mu a_{(m-1)p} + (\omega^2 \mu \bar{\epsilon}_r - \beta_m^2) a_{mp} + \frac{1}{2}\Delta\epsilon_r \omega^2 \mu a_{(m+1)p} = \xi_p^2 a_{mp} \tag{3.58}$$

The coefficients of the left hand side of equation (3.58) are constants and this equation can be solved in terms of eigenvalues (ξ_p^2) and eigenvectors (a_{mp}) of the coefficient matrix.

3.4 Summary

Starting from Floquet's theory, equation (3.15) was obtained though rigorous derivation representing the electromagnetic field inside a grating. Modal expansion and coupled-wave expansion offer two different views of the field and consequently lead to different wave equations and physical images. However, both views are also equivalent and each is just an alternative representation of the same total field.

In the coupled-wave representation (3.29), the field inside the modulated medium is expanded in terms of the space harmonic components of the field in the periodic structure. These space harmonics inside the grating are phase matched to diffracted orders outside of the grating. The individual space harmonic field does not satisfy the wave equation and thus does not exist alone but the summation of it does. The partial space harmonics are actually inhomogeneous plane waves with varying amplitudes along z. These inhomogeneous plane waves are not independent and they couple energy among themselves. In the special case of a sinusoidal grating, electromagnetic power is coupled by every single space harmonic field back and forth between each other. Many famous analytical results can be obtained from this coupled-wave representation, which will be demonstrated in the next chapter.

In the modal representation (3.55), the field inside the grating is expanded in terms of modes of the periodic medium. The total electric field is expressed as a weighted summation over all possible modes. Each individual mode p satisfies the wave equation and may be either evanescent or propagating. Each mode consists of an infinite number of space harmonics m and each mode propagates through the medium without change.

Both methods can be employed to analyze the interaction between an incident light wave and a propagating acoustic wave. Since there is an infinite number of components in the field expressions of both coupled-wave expansion and modal expansion, numerical methods with the aid of computer must be utilized.

Chapter 4

Guided Wave Acoustooptic Interaction

Since the first experimental demonstration of the acoustooptic interaction guided optical waves (GOW) and surface acoustic waves (SAW) in a glass film on a quartz substrate [63], various thin film acoustooptic devices have been proposed [64]∼[66]. Such thin-film guided-wave devices have the advantages of high-power densities, long interaction length, high efficiency, and controllable dispersion associated with the guided-wave characteristics of GOW and SAW. The planar structure, which can be fabricated using related techniques from semiconductor technology, may provide flexibility of device designs and affords the possibility of cost saving.

The AO interaction in such guided-wave acoustooptic device (GWAO) differs from that between bulk waves primarily because of the complicated strain distributions of the SAW and the properties of the GOW. The efficiency of such interaction relies not just on the interaction length and acoustic power, but also strongly depends on the overlap between the GOW and SAW since they are both confined in particular regions in the layered structure. The performance of such a device is more sensitive to the acoustic frequency because, apart from the dispersion of SAW velocity, the penetration depth of the SAW and consequently the overlap between the guided waves, is frequency-dependent. In this chapter, theoretical investigation of the diffraction efficiency of GWAO is demonstrated. Numerical results obtained from the modeling and the unique features will be discussed in Chapter 5 and 6.

The basic knowledge of optical waveguide is given in Appendix E. In section 4.3, an approximated coupled-wave method presented in the previous chapter is used to

describe the SAW induced diffraction from one optical mode to another with the overlap integral introduced into the expression of diffraction efficiency. In section 4.1, the different mechanism involved in the AO diffraction in GWAO is analyzed and the corresponding contributions are discussed.

4.1 Transverse Perturbation of index by SAW

Given a SAW propagating on the surface of a substrate, the refractive index (or permittivity) is perturbed periodically along the propagation direction of the beam (along x-axis, laterally) due to the traveling strain, as presented in equation (1.1). It will be just like that in the case of bulk acoustic wave which is generally supposed to be a plane wave. For the surface wave, however, the induced perturbation of index Δn is not uniform in the direction of depth of the substrate (along y-axis, transversely). This is because the SAW decays along the depth direction and penetrates only a couple of wavelengths in length and the index perturbation becomes weaker as the strength of the SAW reduces. The schematic of transverse index perturbation $\Delta n(y)$ is illustrated in figure 4.1.

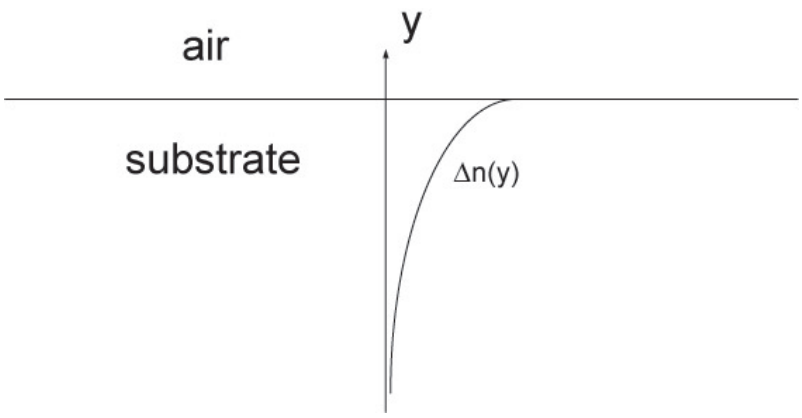

Figure 4.1: Schematic of the transverse index perturbation varying along depth of the substrate due to SAW.

In acoustooptic interaction, in general, there is more than one mechanism involved in the index perturbation, i.e., photoelastic effect, electrooptic effect and surface corrugation, [67]. The resultant index perturbation is the sum of all three effects.

Firstly in photoelastic effect, the induced index perturbation is a function of applied strains

$$\Delta\left(\frac{1}{n^2}\right)_{ij}^{\text{pe}} = p_{ijkl}S_{kl} \qquad i,j,k,l = 1,2,3 \tag{4.1}$$

with p_{ijkl} being the photoelastic constants of a particular crystal and S_{kl} being the acoustic strain components.

In a piezoelectric material, there exist induced electric fields associated with the propagating acoustic waves. The refractive index therefore can be changed via the electrooptic effect. The electrooptic effect of interest here is usually called the linear electrooptic effect (Pockels effect) while the quadratic electrooptic effect (Kerr effect) in which the index is changed as the square of the electric field, is out of this consideration. The refractive index is thus perturbed in the form of

$$\Delta\left(\frac{1}{n^2}\right)_{ij}^{\text{eo}} = r_{ijk}E_k \qquad i,j,k = 1,2,3 \tag{4.2}$$

where r_{ijk} are the electrooptic constants and E_k is the induced electric field component. Moreover, the surface ripple on the top layer created by the acoustic surface wave causes a periodic thickness variation in the waveguide. This movement of the dielectric boundary also produces a refractive index variation, which is

$$\Delta n^{\text{sur}} = \frac{1}{2}\delta_0 \frac{n_{\text{eff}}^2 - 1}{n_{\text{eff}}} \frac{|\nu(0)^2|}{\int \nu^2(y)dy} \tag{4.3}$$

where δ_0 is the amplitude of the ripple at the surface $y = 0$, $\nu(y)$ is the normalized transverse distribution of the incident and diffracted modes, and n_{eff} is the effective index of the given modes. Since the absolute value of the ripple amplitude is quite small the contribution from the surface corrugation is expected to be negligible.

The total magnitude of the index perturbation involved in the acoustooptic diffraction is thus in the form

$$\Delta n = \Delta n^{\text{pe}} + \Delta n^{\text{eo}} + \Delta n^{\text{sur}} \tag{4.4}$$

Combining equation (4.1)$\sim$(4.3) into equation (4.4) yields

$$\Delta n(y) = -\frac{n^3}{2}(pS(y) + rE(y)) + \frac{1}{2}\delta_0 \frac{n_{\text{eff}}^2 - 1}{n_{\text{eff}}} \frac{|\nu(0)^2|}{\int \nu^2(y)dy} \tag{4.5}$$

in which the suffix is omitted for convenience.

4.2 Multilayer Optical Waveguide with small perturbation

Consider a substrate of multilayer structure on which a SAW is produced. From the viewpoint of optical aspect, the effect of a traveling SAW beam is the modulation of the refractive index of the system, i.e.

$$n(x, y) = n(y) + \Delta n(y) \cos Kx \tag{4.6}$$

where $n(y)$ denotes the index profile of the multilayer structure and $\Delta n(y)$ takes the form of equation (4.5) of the previous section, as illustrated in figure 4.2. The transverse index perturbation can alternately be expressed in the form

$$\Delta n(y) = \Delta n_0 \nu_a(y) \tag{4.7}$$

where Δn_0 is the index changing at the surface and $\nu_a(y)$ is a normalized function with $\int |\nu(y)|^2 dy = 1$.

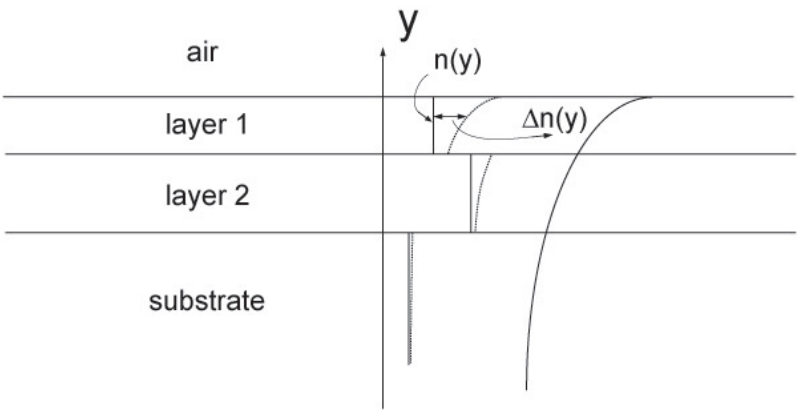

Figure 4.2: Schematic of the transverse distribution of refractive index in a multilayer structure with SAW present.

Substituting equation (4.6) into the wave equation (D.41) yields a second order differential equation with such solutions that variable separation cannot be done. Analytically solving this equation will be extremely complicated in mathematics. Alternately, using approximate approaches such as the effective index method and small perturbation method as presented in Appendix E.3 and F, the form of the solution can be simplified.

Considering TE polarized wave, the electric field of a particular mode supported by the layered structure with the absence of SAW is assumed to be in the form

$$\bar{E}_x(y,z) = \bar{C}_p \nu_p(y) e^{-j\bar{\xi}_p z} \tag{4.8}$$

where C_p are the mode weights and $\nu(y)$ is the normalized field distribution. The effective index of the system for this mode is thus

$$\bar{n}_{\text{eff}} = \frac{\xi_p}{k_0} \tag{4.9}$$

Once the SAW is generated and the index perturbation is produced, following the derivation given in Appendix F with the fact that the index change is usually weak ($\sim 0.1‰$), the perturbed electric field becomes

$$E_x(y,z) = C_p \nu_p(y) e^{-j(\bar{\xi}_p + \Delta\xi)z} \tag{4.10}$$

with

$$\Delta\xi_p = k_0 \Delta n_0 \Gamma_p \tag{4.11}$$

and

$$\Gamma_p = \frac{\int_{-\infty}^{\infty} \nu_p(y)\nu_a(y)\nu_p^*(y)}{\int_{-\infty}^{\infty} \nu_p(y)\nu_p^*(y)} \tag{4.12}$$

where Γ_p here is the overlap integral with refractive index concerned. In deriving equation (4.11) and (4.12) the relation $\Delta\epsilon \approx 2n\Delta n$ is used.

The new effective index is thus obtained

$$n_{\text{eff}} = \frac{\xi_p + \Delta\xi_p}{k_0} \tag{4.13}$$

or

$$n_{\text{eff}} = \bar{n}_{\text{eff}} + \Delta n_{\text{eff}} \tag{4.14}$$

and

$$\Delta n_{\text{eff}} = \Delta n_0 \Gamma \tag{4.15}$$

with the suffix of Γ_p omitted. Equation (4.14) indicates that in a multilayer system with small perturbation of index present, for a particular transverse optical

mode, the two dimensional varying index (4.6) can be simplified to one dimension, i.e.

$$n(x, y) \approx \bar{n}_{\text{eff}} + \Delta n_{\text{eff}} \cos Kx \tag{4.16}$$

Consequently, the simplified wave equation can be obtained. In order to be consistent with Chapter 3, the wave equation is expressed in permittivity again, that is

$$\nabla^2 E(x, z) + (\bar{\epsilon}_{\text{eff}} + \Delta\epsilon_{\text{eff}} \cos Kx) k_0^2 E(x, z) = 0 \tag{4.17}$$

where $\epsilon_{\text{eff}} = n_{\text{eff}}^2$ and $\Delta\epsilon_{\text{eff}} \approx 2n_{\text{eff}}\Delta n_{\text{eff}}$. Equation (4.17) indicates that by using the average value of permittivity along y direction, the problem of the interaction between a incident optical mode (transversely) and a SAW can be treated as a grating diffraction problem for a plane wave as presented in Chapter 3. The details of the AO interaction of guided waves will be discussed in the next section.

4.3 Interaction Between Guided Optical Waves and Acoustic Waves

In acoustooptic diffraction with Bragg condition satisfied, when the incident optical wave takes the form of a mode confined in a layered structure rather than a plane wave, the diffracted wave can still be a bounded mode, though it does not have to be of the same mode number. A schematic of such conversion between two optical modes is illustrated in figure 4.3a. The layer is of thickness H and the grating produced by the SAW is assumed to be along x-axis. The Bragg condition in the AO interaction, represented in equation (3.44) in the previous chapter, can be rewritten

$$\sin\theta_B = \frac{\lambda_0}{2n_{\text{eff}}\Lambda} \tag{4.18}$$

where λ_0 is the optical wavelength in free space, Λ is the acoustic wavelength and n_{eff} is the effective index of the optical mode in such layered structure. In fact, equation (4.18) has assumed that the incident and diffracted optical beams are confined in the same mode. In a general case, a diffraction including mode conversion, the wave vector relation illustrated in figure 4.3b holds

$$\boldsymbol{k}_n = \boldsymbol{k}_m + \boldsymbol{K} \tag{4.19}$$

with $\boldsymbol{K}$, $\boldsymbol{k}_m$ and $\boldsymbol{k}_n$ being the wave vector of SAW, incident and diffracted optical mode, respectively. The angles of incidence and diffraction, θ_m and θ_n, respectively, are obtained geometrically, [68].

$$\sin\theta_m = \frac{\lambda_0}{2n_m\Lambda}(1 + \frac{\Lambda^2}{\lambda_0^2}(n_m^2 - n_n^2)) \tag{4.20}$$

$$\sin\theta_n = \frac{\lambda_0}{2n_n\Lambda}(1 - \frac{\Lambda^2}{\lambda_0^2}(n_m^2 - n_n^2)) \tag{4.21}$$

where n_m and n_n are the effective refractive indices of these modes. When the mode conversion does not occur , i.e. $m = n$, equation (4.20) and (4.21) reduce to equation (4.18).

The electric fields concerned are assumed to be both TE polarization. Although TE-TM polarization conversion of AO interaction in anisotropic medium is achievable [69], it is not considered here. The x variation of the electric fields in figure 4.3a is very slow since the $\theta_{m,n}$ are both sufficiently small. Therefore, by adding z-dependency into the amplitudes, the field described in equation (E.2) is rewritten below

$$E_m(x,y,z) = \nu_m(y)E'_m(x,z) = \nu_m(y)U_m(z)e^{-j(k_{mx}x + k_{mz}z)} \tag{4.22}$$

$$E_n(x,y,z) = \nu_m(y)E'_n(x,z) = \nu_n(y)U_n(z)e^{-j(k_{nx}x + k_{nz}z)} \tag{4.23}$$

The factors $\nu_m(y)$ and $\nu_b(y)$ are the normalized field distributions of the optical waves of mode number m and n, respectively. The suffixes x and z represent the x and z components of the wave vectors k_m and k_n. $U(z)$ is the unknown separated amplitudes of the optical waves varying along the AO interaction length (z direction), which reflects the fact that the incident and diffracted waves are coupled.

Using the effective index technique presented in the previous section, the grating produced by the SAW is

$$n_{m,n}(x,y) \approx \bar{n}_{m,n} + \Delta n_{m,n}\cos Kx \tag{4.24}$$

and

$$\Delta n_{m,n} = \Delta n_0 \Gamma mn, nm \tag{4.25}$$

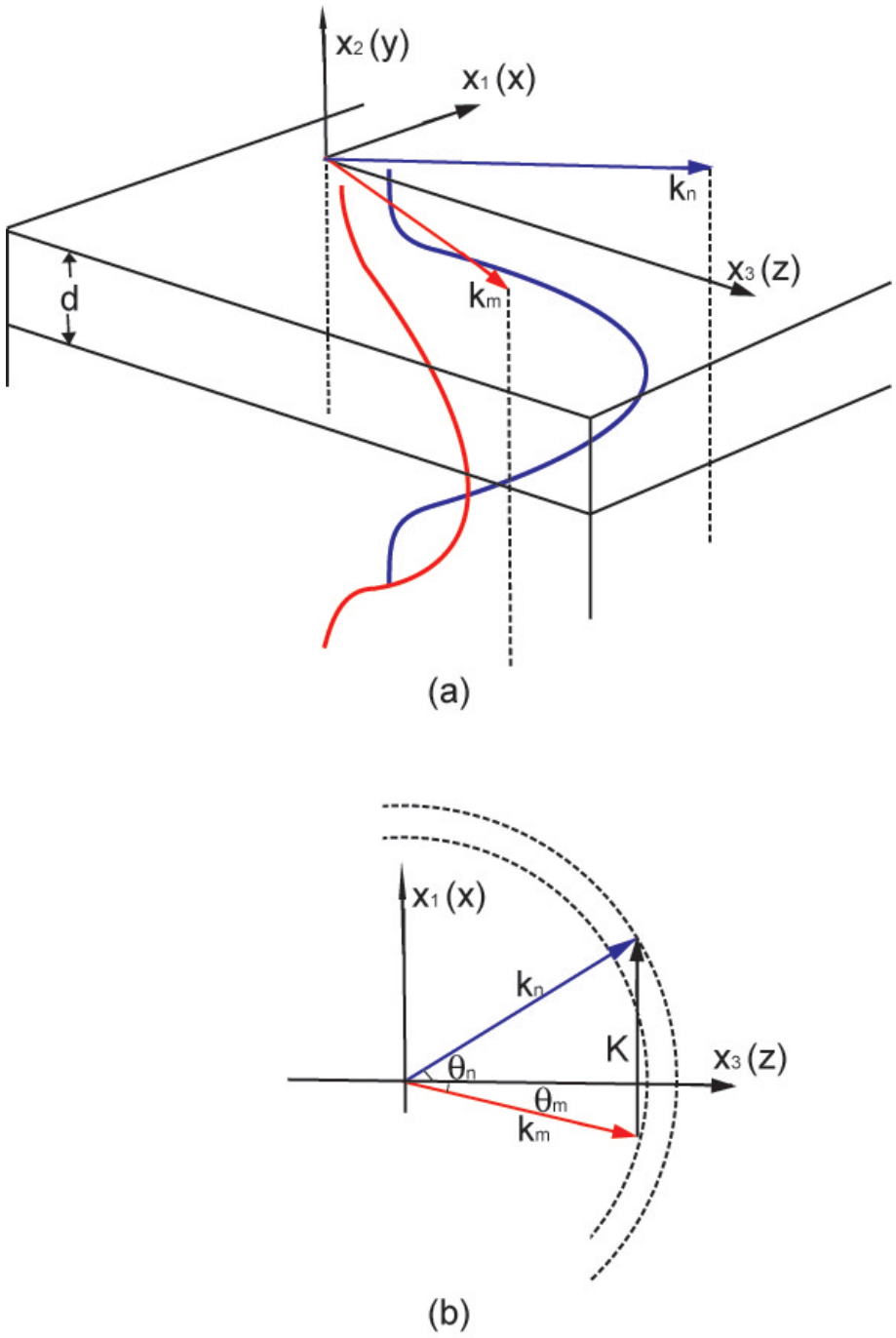

Figure 4.3: Schematics of interaction between guided optical modes and acoustic waves. (a), The incident and diffracted optical modes; (b), Momentum reservation relationship.

$$\Gamma_{mn} = \frac{\int_{-\infty}^{\infty} \nu_m(y)\nu_a(y)\nu_n^*(y)dy}{\int_{-\infty}^{\infty} \nu_m(y)\bar{f}_m^*(y)dy} \tag{4.26}$$

$$\Gamma_{nm} = \frac{\int_{-\infty}^{\infty} \nu_n(y)\nu_a(y)\nu_m^*(y)dy}{\int_{-\infty}^{\infty} \nu_n(y)\bar{f}_n^*(y)dy} \tag{4.27}$$

The y variation of optical modes in equation (4.22) and (4.23) can thus be omitted, and the the electric fields (4.22) and (4.23) can be understood as $E'_m(x,z)$ and $E'_n(x,z)$ propagating in a homogenous medium along the y-axis. Using the approximated couple-mode method presented in section 3.2.2 gives the coupled equations

$$\frac{dU_m(z)}{dz} = -j\kappa_m U_n(z) \tag{4.28}$$

$$\frac{dU_n(z)}{dz} - j\gamma U_n = -j\kappa_n U_m(z) \tag{4.29}$$

and

$$\kappa_m = \frac{k_0 \Delta n_m}{2\cos\theta_m}; \kappa_n = \frac{k_0 \Delta n_n}{2\cos\theta_n} \tag{4.30}$$

$$\gamma = \frac{K^2 - 2\beta_0 K}{2k_n \cos\theta_n} \tag{4.31}$$

The diffraction efficiency at the Bragg condition in this case is thus obtained

$$\eta = sin^2\left(\frac{\pi}{\lambda_0}\sqrt{\frac{M_2 L P_a \Gamma_{mn}\Gamma_{nm}}{2H_{\text{eff}}\cos\theta_m\cos\theta_n}}\right) \tag{4.32}$$

To be consistent with the expression of equation (3.46) for the plane wave case, the concept of effective thickness of SAW is introduced, i.e.

$$H_{\text{eff}} = \frac{H}{\int_0^H \nu_a(y)\nu_a^*(y)dy} \tag{4.33}$$

It can be understood as the thickness of an acoustic beam with the homogenous displacements and the power intensity P_a/LH_{eff}, equal to that of the surface acoustic wave.

If the incident and diffracted optical modes are identical TE modes, both of them will see the same index perturbation. The diffraction efficiency (4.32) becomes

$$\eta = sin^2\left(\frac{\pi\Gamma_{mm}}{\lambda_0\cos\theta}\sqrt{\frac{M_2 L P_a}{2H_{\text{eff}}}}\right) \tag{4.34}$$

$$\Gamma_{mm} = \frac{\int_{-\infty}^{\infty} \nu_m(y)\nu_a(y)\nu_m^*(y)dy}{\int_{-\infty}^{\infty} \nu_m(y)\bar{f}_m^*(y)dy} \tag{4.35}$$

Compared with the expression for the plane wave case of equation (3.46), the main difference with the efficiency of AO diffraction between GOW and SAW is the addition of the overlap integral Γ, which is a measure of the spatial field distribution of the waves. This integral occurs only for layered structures of AO devices having a value from 0 to 1. Its integral region is restricted in the film thickness if the acoustooptic interaction outside the film is very weak. Though the value of Γ could be small compared with the unit, the dimension of the effective thickness can always be practically made to be very thin and the consequent efficiency can be much higher than the bulk AO interaction.

4.4 Summary

This chapter discusses the case of AO interaction between guided optical waves and surface acoustic waves. Multiple mechanisms involved in the AO affect in piezoelectric materials are analyzed. The effective index technique is used to simplify the expression of the refractive index $n_{x,y}$ to an x-dependent only function. The coupled-wave method, derived in the case of bulk wave AO diffractions, is demonstrated to be used in the guided wave device by considering the overlap integral of the guided optical and acoustic waves. The overlap integral is an important factor concerned in the diffraction efficiency of GWAO devices.

Chapter 5

FISOS Design: Qualitative Consideration

With the increasing use of optical signals for communications, data storage and sensors, there is a continuing interest in developing corresponding functional elements suitable for monolithically integrated optical circuit applications. Technologies for controlled variability to provide functionality in such optical circuits are quite mature nowadays, for example, by inducing refractive index changes via electrooptic effect, [70], elastooptic effect (photoelastic effect), [71], or carrier injection, [72], etc. Among these approaches, acoustooptic applications utilizing photoelastic effect (and electrooptic effect in piezoelectric medium), particularly the guided wave AO devices driven by acoustic surface wave, have attracted attentions by their significant gains of AO diffraction, relatively low required power, high operation speed and potential feasibility of functionality control.

However, in conventional GWAO devices reported so far, the optical source is assumed to be external to the AO diffraction element. In those devices an essential need is to inject the optical signal into the Bragg cell. There are, in fact, three commonly used methods for coupling the optical mode into planar waveguide. A straightforward way is to collimate an optical fiber to the edge of the wafer, [73]. The experimental configuration for this method is quite simple but very precise fiber alignment / device bonding is essential; besides, the mismatch between optical modes in the fiber and in the waveguide could be large. Another two methods are to couple optical waves from the wafer surface, either through a prism [74] or with an etched planar grating [75]. The employment of a lens to collimate laser beams is

usually unavoidable and so are some other optical elements, such as polarisers. It can be concluded that external optical sources along with other optical components bring in extra complexity to the system assembly, leading to further insertion loss from each additional element.

The purpose of the work presented in this chapter is to propose a practical device structure and appropriate device design guidelines for a functional SAW controlled processor integrated with a semiconductor Laser/LED. This functional integrated semiconductor optical source (FISOS) is expected to be compact in size, flexible in function and robust in performance.

Section 5.1 gives a brief review of several candidate materials used for acoustooptic applications and for light emitting devices. The material parameters and corresponding characteristics of those materials are discussed and suitable materials such as GaAs or GaN, are suggested. In section 5.2, a typical structure of a GaN optical source is represented and the output optical beam profiles are demonstrated with the given material parameters. The prototype design of this integrated device is discussed in section 5.3, giving a description of the structure of FISOS and the optimization to obtain an enhanced performance.

5.1 Selection of Suitable Candidate Materials

A vital limitation of the development of integrated devices is the choice of proper materials with appropriate characteristics which can meet various demands from each unit. The nature of the proposed SAW controlled optical source imposes twofold requirements for the material: efficiently launching the acoustooptic effect and the capability of being an effective optical source. The material selection will be discussed in both ways.

From the acoustooptic consideration, to design a device with high diffraction efficiency, the first criterion is a medium with high figure of merit (M_2, equation (3.47)). This is equivalent to selecting a material with a large refractive index, a large photoelastic constant and low acoustic velocity.

Low acoustic velocity, for an AO deflector, also favours the large angle of deflection and large number of resolvable spots (as discussed in detail in Chapter 6), but it is adverse to the attainment of a high speed operation. Moreover, low acoustic speed typically also introduces high acoustic attenuation, α, since approximately,

[76]

$$\alpha \propto \frac{1}{v^5} \tag{5.1}$$

where α is the attenuation coefficient of materials.

Therefore, in selecting the acoustooptic materials, a certain compromise has to be made between their figures of merit and acoustic attenuation, depending on the purpose of applications. Some popular crystalline AO materials and their corresponding parameters are listed in Table 5.1, and the analysis of several typical materials is given here.

$LiNbO_3$ $LiNbO_3$ is a well-known material used in acoustic, electrooptic and acoustooptic devices. The utilization of the crystal for high frequency acoustooptics has been indicated from the photoelastic measurement made by Dixon and Cohen [77] and acoustic loss measurements made by Wen Mayo [78]. As shown in table 5.1, a high figure of merit and very low acoustic attenuation make $LiNbO_3$ quite suitable for wideband AO modulators [79], high speed AO switches [80] and tunable filters [81].

TeO_2 A notable feature of TeO_2 is that the transverse acoustic wave propagating along the [110] direction with the displacement along [110] is characterized by an extremely low velocity of 616m/s. Combined with high refractive indices of this crystal, the shear mode should have a high figure of merit, and this feature was confirmed by Uchida and Ohmachi, [82]. Although TeO_2 suffers the large attenuation constant [83], it attracts a lot of interests in acoustic device [84] and functional AO devices [85] $\sim$ [87].

GaAs High figure of merit of GaAs makes it a good candidate for acoustooptic applications, particularly in anisotropic AO devices benefited by its high birefringence. This feature can be enhanced by multiquantum-well structure and thus tunable filters and mode converters are potential applications, [88]. GaAs is also an important candidate material useful in infrared region for optical communication and laser radar. Firstly, it is transparent in the infrared region. Besides, since the deflection efficiency is inversely proportional to the square of optical wavelength, the high figure of merit of GaAs becomes quite essential for efficient operation of the devices.

Table 5.1: Parameters concerned in AO applications of typical materials

Material	Elastic wave Propag. dir. /mode[a]	Elastic velocity (10^3m/s)	Elastic attenuation (dB/cm·GHz^2)	Optical polar. dir.[b]	Refractive index	M_1 (10^{-8} m^{2}s/kg)	M_2 (10^{-15} s^3/kg)	M_3 (10^{-11} ms^2/kg)
$LiNbO_3$	[100]/L	6.57	0.15	||	2.2	66.5	7	10.1
	[001]/S	3.59	2.6	$\perp$	2.29	9.2	2.92	2.4
TeO_2	[001]/L	4.20	3.8	$\perp$	2.26	138	34.5	32.8
	[110]/T[c]	0.616	70	[d]	2.26	68	793	110
GaAs[e]	[110]/L	5.15	3.8	||	3.37	925	104	179
	[100]/T	3.32	30	arb.	3.37	155	46.3	49.2
Sapphire	[100]/L	11	0.2	||	1.766	7.7	0.36	10.7
	[001]/L	11.2	0.2	||	1.758	7.32	0.34	0.66
GaN[f]	[1$\bar{1}$0]/R	4.7		$\perp$	2.35		1.95	

[a] L, longitudinal wave; T, transverse wave; R, Rayleigh wave

[b] || and $\perp$, parallel and perpendicular to the acoustic wave vector, respectively

[c] Displacement along [1$\bar{1}$0].

[d] Circularly polarized light incident along the z axis.

[e] Data measured at optical wavelength of 1153nm, whilst the rest material at 633nm.

[f] Data for GaN is from ref. [91] whilst the rest value all from ref. [76]

GaN Although GaN is a well-known blue light emitting material, its applications on acoustooptic interaction was not considered until quite recently. Ciplys in 2002 reported that the AO interaction played an important role in the spectral response to ultraviolet illumination in a GaN-based SAW oscillator, [89]. A UV GaN detector modulated by surface acoustic waves was demonstrated by Palacios in 2004 [90]. The diffraction effect of guided light by SAW was investigated mainly by Shur and Ciplys, [91]$\sim$[93]. The acoustic attenuation for GaN was not available in the literature, but the magnitude of α can be estimated to be in the order of 1.0dB/cm·GHz^2 using equation (5.1) from data in table 5.1.

Now consider the second requirement of material choice for FISOS. Most of the AO materials can only be utilized in passive devices with an external source, i.e., they do not have the capability of being an efficient optical source. Therefore only two candidate materials are left which meet the twofold criterion. They are GaAs and GaN; the detailed parameters are listed in Table 5.2.

From the discussions above, both GaAs and GaN are capable of producing efficient AO diffraction whilst GaAs has a much larger M_2, which means more loaded acoustic power will be needed for the GaN device when 100% diffraction occurs. But this drawback could be compensated to some degree by applying a very thin film of GaN (equation (4.32)). However, the weaker piezoelectric effect in GaAs will require a deposition of a ZnO epitaxial layer (a strong piezoelectric material) on top of GaAs to efficiently generate acoustic waves using IDTs, [94].

Considering the burgeoning interest in blue and ultraviolet wavelength applica-

tions, this project considers a GaN based integrated device structure. Although, of course, the analysis, modeling and methods presented in this monograph are equally applicable for GaAs based integrated devices.

Table 5.2: Material parameters used in the modeling of FISOS

Material	Mass density (10^3kg/m^3)	Stiffness index (GPa)	Piezoelectric index (C/m^2)	Photoelastic index	Electrooptic index (pm/V)
GaN	6.15[a]	c_{11}=370 c_{12}=145 c_{13}=110 [a] c_{33}=390 c_{44}=98	e_{15}=-0.3 e_{31}=-0.36 [b] e_{33}=1	p_{11}=-0.086 [c] p_{13}=-0.017	r_{13}=0.57[d]
AlN	3.512[e]	c_{11}=345 c_{12}=125 c_{13}=120 [e] c_{33}=395 c_{44}=118	e_{15}=-0.48 e_{31}=-0.58 [e] e_{33}=1.55	p_{11}=-0.10 [c] p_{13}=-0.019	
GaAs	5.34	c_{11}=119 c_{12}=53.8 c_{44}=59.4	$e_{14} = -0.16$	p_{11}=-0.165 p_{12}=-0.14 p_{44}=-0.072	r_{41}=-1.43[f]
Sapphire[g]	4	c_{11}=497.6 c_{12}=162.6 c_{13}=117.2 c_{14}=22.9 c_{33}=501.8 c_{44}=147.2			

[a] Bougrov V., Levinshtein M.E., Rumyantsev S.L., Zubrilov A., Properties of Advanced Semiconductor Materials GaN, AlN, InN, BN, SiC, SiGe. Eds. Levinshtein M.E., Rumyantsev S.L., Shur M.S., John Wiley & Sons, Inc., New York, 2001

[b] M.S. Shur, GaN-based pyroelectric and piezoelectric sensors,

[c] S. Yu. Davydov, Evaluation of physical parameters for the group III nitrates: BN, AlN, GaN, and InN, Semiconductors, 36, 41, 2002

[d] X.C. Long, R.A. Myers, S.R.J. Brueck, R. Ramer, K. Zheng, and S.D. Hersee, GaN linear electro-optic effect, Appl. Phys. Lett., 67, 1349, 1995

[e] Tsubouchi, K.; Sugai, K.; Mikoshiba, N., AlN Material Constants Evaluation and SAW Properties on AlN/Al2O3and AlN/Si, Proc. IEEE, Ultrason. Symp., 375, 1981

[f] The linear electrooptic constant was measured by R.L. Greene and K.K. Bajaj in Solid state commun. (USA), 45, 831, 1983, whilst the rest data for GaAs is referenced from S. Adachi, GaAs, AlAs and AlGaAs: Material parameters for use in research and device applications, J. Appl. Phys, 58, R1, 1985

[g] J. M. Winey and Y. M. Gupta, r-axis sound speed and elastic properties of sapphire single crystals, J. Appl. Phys. 90, 3109, 2001

5.2 Structure of Optical Source

Since the first Gallium Nitride LED was reported in 1971 by Pankove [95], designs and fabrications of GaN involved laser diode/LED have experienced a great development in applications such as optical storage, printing, full-colour displays, chemical sensors and medical applications. GaN and its alloys, like AlGaN or InGaN, have generated a lot of interest from industries not only because of their direct bandgap nature for efficient light emission, but also the controllable band gap (between 3.45 and 6.2eV) by varying the Al/In fraction in the alloy. The nitride compound therefore can be made suitable for emission wavelength from UV to green.

There are some other candidates for a blue light emitting device, such as SiC and ZnSe. The quantum efficiency of SiC is limited by the indirect bandgap nature of the material and would require high drive currents. ZnSe is also a direct bandgap material (2.67eV), but it suffers from its low thermal conductivity, poor thermal stability, large ohmic contact resistances and low damage threshold. Therefore GaN turns out to be a better choice for commercial blue light source.

The GaN LED proposed by Pankov in 1971 was not a *p*-*n* junction LED, rather it was a metal-insulator-semiconductor LED since *p*-type GaN was still not available at that time. The first successful demonstration of *p*-*n* GaN LED was reported by Akasaki in 1989 [96], who grew Mg-doped GaN layer on top of an undoped n-type GaN film. In 1995, utilizing InGaN film as the active layer, Nakamura [97] demonstrated the fabrication of the first GaN laser diode. Since then rapidly increasing developments have been achieved throughout the world [98] $\sim$ [102].

The schematic of a typical InGaN multiple-quantum-well (MQW) structure is illustrated in figure 5.1. A buffer layer of GaN is grown on *c*-plane sapphire to reduce the dislocation density before epitaxial films of $Al_xGa_{1-x}N$ are deposited above. To achieve sufficient waveguiding, relatively thick $Al_{0.16}Ga_{0.84}N$ strained-layer superlattice (SLS) cladding layers construct a sandwich structure with the active region, which is composed of two 3nm $In_0.05Ga_0.95N$ quantum wells with 10nm GaN barrier layers. Contact stripes are patterned on these films with typical widths ranging from 0.5μm to 2μm. The structure is formed by etching around the *p*-contact stripe through a depth of 120nm, which serves as a lateral ridge waveguide as well. The compositions and thicknesses are listed in table 5.3 in summary. This structure has referred to conventional designs of InGaN MQW, such as simulation

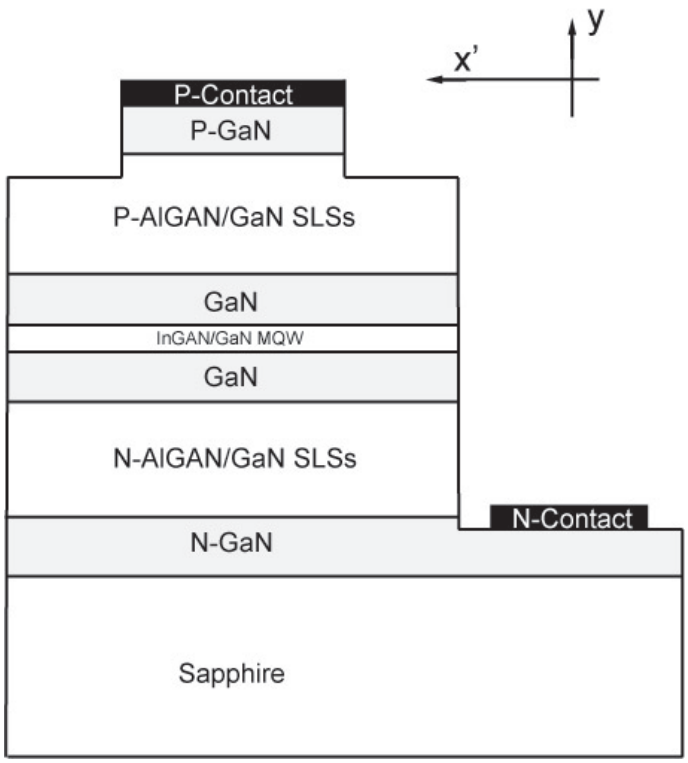

Figure 5.1: Schematic of the cross-section of GaN based optical source.

analysis by Piprek [103] and experiments by Shiojiri [104]. The wavelength of the violet light emitted by this given structure is set to be $\lambda_0 = 405$nm.

To give a numerical evaluation of the proposed GaN laser/LED, there are a lot of associated properties to analyze, such as waveguiding, output power, injected current flow, heat flux, carrier drift and diffusion and defect recombination, etc. The optical modes will be mainly analyzed here because: a, the confinement factor of a given mode is multiplied by the material gain, affecting both the amount of current required to pump the laser and the profile of the output light; b, for the concern of designing a GWAO device integrated in the FISOS, the profile of the optical mode strongly affects the overlap between the GOW and SAW and the value of overlap integral (Γ, equation (4.35)) plays an important role in the performance of the integrated device. Therefore the analysis of mode shapes in the given structure is the main concern of the analysis of the optical source as a part of designing of the proposed integrated device.

The step in the refractive index between the different layers plays a key role in determining the number of modes supported and the mode profiles. The refractive index is dependent on the composition of the AlGaN alloy and also on the wavelength of the light. Larger steps in refractive index require a high fraction of aluminium in

Table 5.3: Layer parameters as used in the simulation

Layer	Material	Thickness (nm)	Refractive Index
Connect layer	P-GaN	100nm	2.5264
Cladding layer	P-$Al_{0.16}Ga_{0.84}N$/GaN SLSs	600nm	2.43
Guilding layer	GaN	100nm	2.5264
Quantum Well	$In_{0.05}Ga_{0.95}N$	3nm	2.63
MP Barrier	GaN	10nm	2.5264
Quantum Well	$In_{0.05}GaN$	3nm	2.63
Barrier	GaN	10nm	2.5264
Guilding layer	GaN	100nm	2.5264
Cladding layer	N-$Al_{0.16}GaN_{0.84}$/GaN SLSs	600nm	2.43
Connect layer	N-GaN	100nm	2.5264
Substrate	Sapphire		1.765

the alloys. However, these layers can be difficult to lattice match to the adjoining material. Therefore, an average mole fraction of 0.08 is chosen in the AlGaN alloy and all the refractive indices are also listed in table 5.3.

The value of indices for GaN, AlN and AlGaN alloy is simulated by the formulas given in Brunner's work in 1997 [105] with the photon energy of 3.06eV. Because of the lack of index data available for InGaN alloys, there are few self-consistent numerical simulations of InGaN, and therefore the magnitude adopted here is gathered from the graph of estimated refractive index curves suggested by Laws in 2001, [106].

It is found there are 14 modes supported in the proposed multilayer structure, in which the fundamental mode is illustrated in figure 5.2. The power fraction confined in the active layer of such structure in fundamental mode is also given, i.e. the confinement factor $\Gamma = 7.76\%$. The lateral modes are also shown in figure 5.3 with different width of the ridge. Only the fundamental mode is supported in the chosen ridge width range.

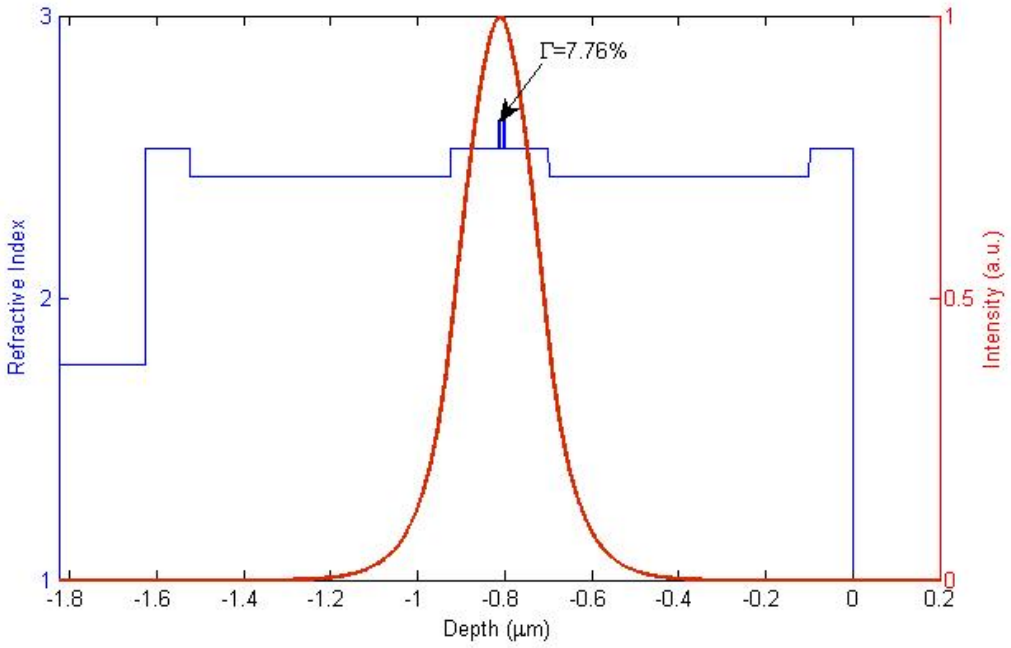

Figure 5.2: Fundamental mode of the GaN/AlGAN multilayer structure. Blue curve corresponds to the left axis and red curve to the right axis.

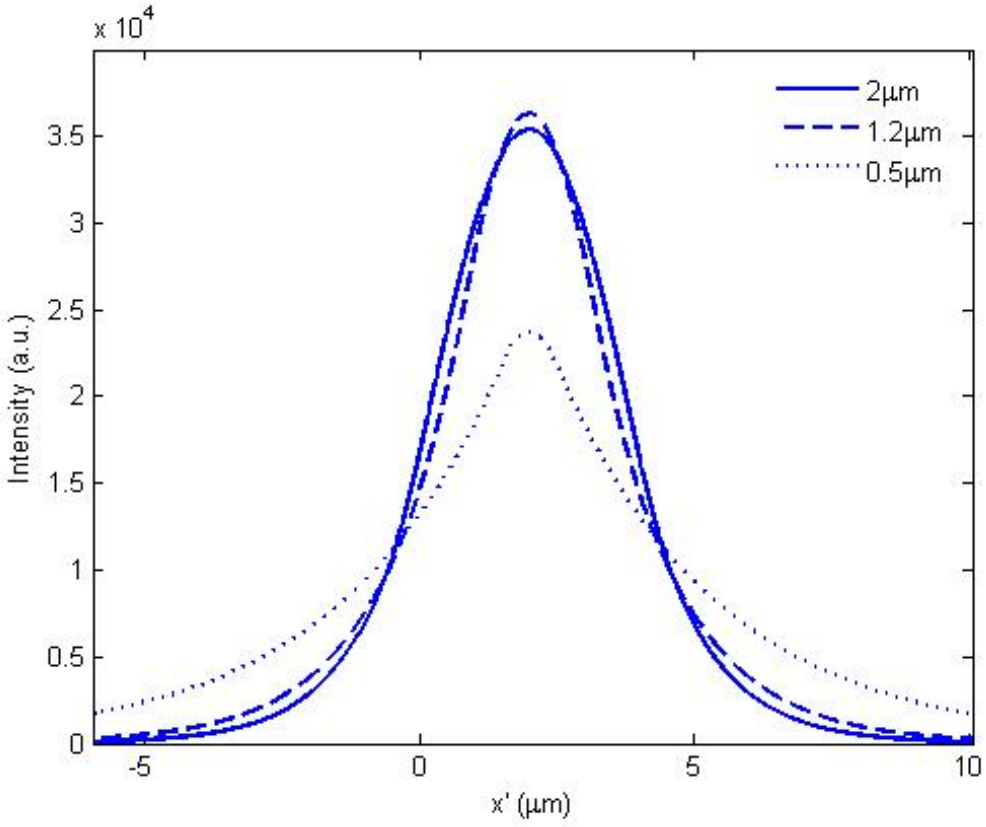

Figure 5.3: Fundamental mode of the lateral ridge waveguide. Different ridge width is choosen to illustrate the divergence of modes.

5.3 Design of the Prototype of FISOS

Device overview The transverse structure of FISOS is considered to be a multiple layer system, amenable to planar fabrication technology. The schematic of the device is illustrated in figure 5.4, suggesting partitioning the configuration into two subdivisions: optical source and acoustic processor. The layered materials used for both parts are the same. The GaN laser/LED is designed at one end of the whole device, with no changes in the usual structure (figure 5.1) except an extension along z'-axis.The interdigitated transducers (IDT) for SAW excitation are assumed to be deposited at the other end of the z' direction. Those transducers are positioned to align precisely to access the maximum of Bragg diffraction efficiency.

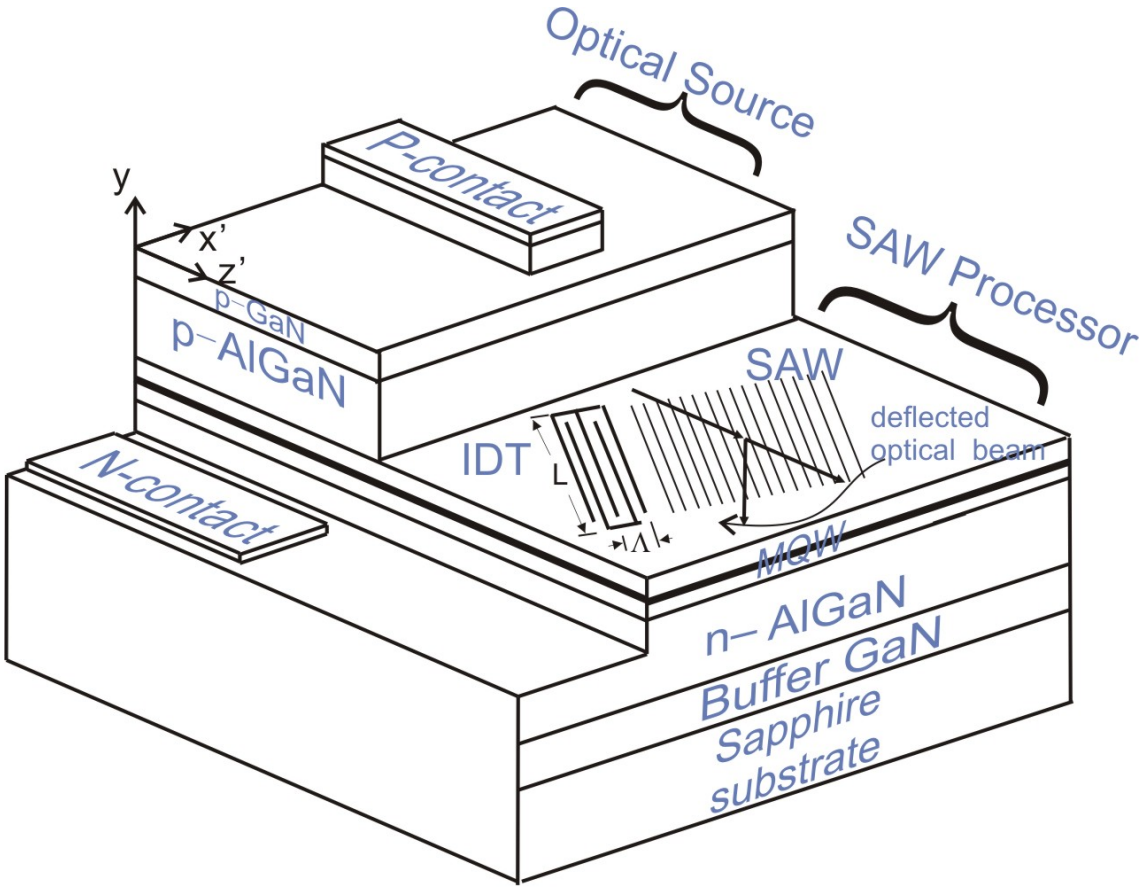

Figure 5.4: Schematic of the prototype of the SAW controlled integrated optical source.

Due to the natural lack of a second mirror in the proposed schematic of this integrated device, the GaN optical source cannot be treated as a laser. However, the assumption of coherent optical radiation is still made to simplify the problem. In fact, an integrated Bragg mirror structure used for a distributed feedback laser can be incorporated if necessary.

The optical wave emitted from the GaN source in the form of modes confined both transversely and laterally, undergoes diffraction in the presence of acoustic waves. Since this schematic is supposed to demonstrate the feasibility of such an integrated device, some useful elements are not included, such as an acoustic absorber or photo detectors, etc. Besides, only the transmitter IDT is considered though a receiver IDT might be required in a practical device to monitor the operation of the SAW.

Etch-down As discussed in Chapter 2, it is known that the acoustic surface wave is mainly confined close to the surface penetrating about one Rayleigh wavelength deep into the material. However, since the optical transverse mode (fundamental mode) is confined mainly in the active region, which is 800nm away from the surface of the device, in order to increase the value of overlap integral of the optical modes and SAW mode, as shown in equation (4.35), an etch-off could be done to the acoustic processor region, as illustrated in figure 5.4. This etching cannot be arbitrarily deep, otherwise the guiding structure in the acoustic processor region will be destroyed. Figure 5.5 shows the plot of two overlap integrals with varying etching depth. Γ_{etch} (blue curve) is the overlap integral between the transverse fundamental mode generated by the GaN source region $\nu(y)$ and the one supported by the acoustic region with an etch-down $\nu^{'}(y)$, that is

$$\Gamma_{\text{etch}} = \frac{\int \nu(y)\nu'^{*}(y)dy}{\int \nu(y)\nu^{*}(y)dy} \tag{5.2}$$

The value of this overlap integral indicates a measure of the power transmitted into the acoustic region when the fundamental mode is passing through the etching facet.

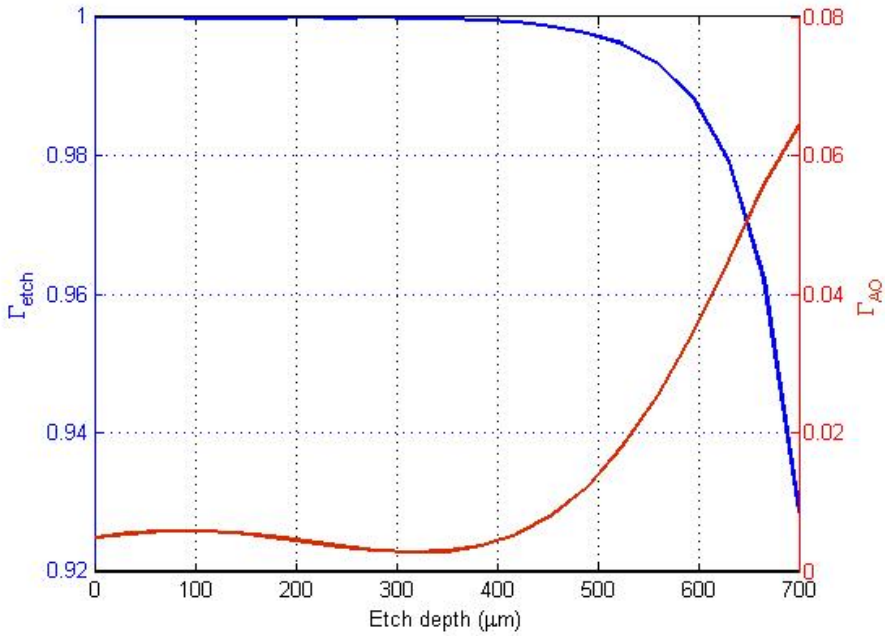

Figure 5.5: Overlap integrals varying with increasing etching depth. Blue curve, left axis; red curve, right axis.

The Γ_{AO} (red) denotes the overlap integral in the process of an acoustooptic interaction, as defined in equation (4.35), in which the incident, diffracted and SAW mode are all involved. The value of Γ_{AO} strongly contributes the AO interaction efficiency and the larger the better. The red curve shown in figure 5.5 is obtained based on the assumption that the incident and diffracted optical mode are both fundamental mode. The data of the SAW mode has been obtained in the example given in section 2.5.

From figure 5.5, The value of Γ_{AO} tends upwards when the etching is deeper. At the same time the power transmission ratio between GaN region and SAW region keeps going downwards as expected. It is found that even when the Γ_{etch} reduces to its minimum, the value of 0.93 still implies a high efficiency transmission. Therefore an etching depth of 700nm is chosen.

The distribution of the optical mode propagating in the acoustic region is thus illustrated in figure 5.6 along with the decaying profile of the index perturbation $\Delta n(y)$ which is obtained from equation (4.1). This index profile is simulated with the given parameter configuration, optical wavelength $\lambda = 405$nm, acoustic frequency $f_0 = 2$GHz, AO interaction length $L = 100\mu$m and acoustic power $P_a = 0.61$mW. The chosen power is the value for which the diffraction efficiency achieves its max-

imum with the given optical and acoustic parameters as shown in figure 1.4. The mean value of the refractive index perturbation is found to be 1.1×10^{-4}.

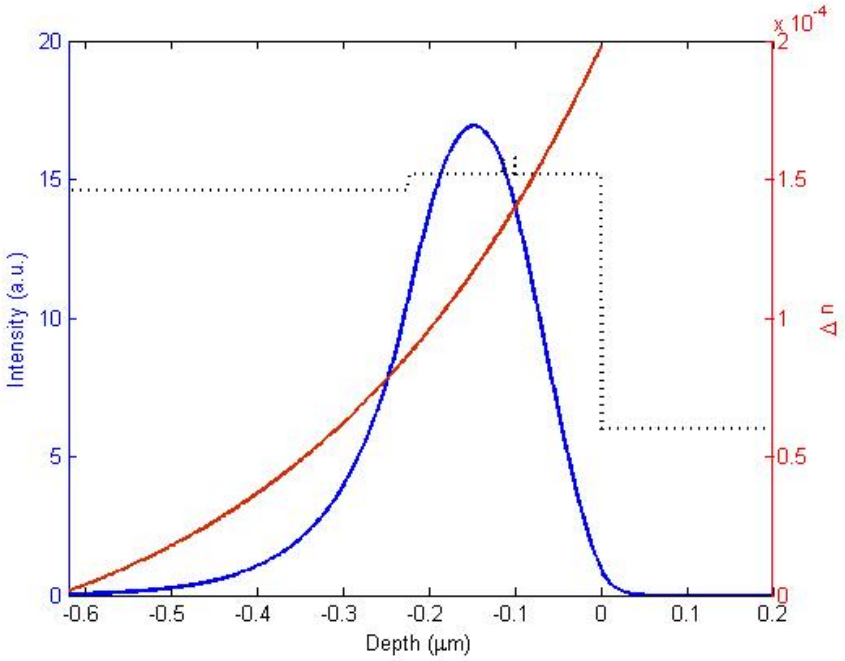

Figure 5.6: Fundamental mode and index perturbation distribution along depth. Blue solid, optical mode; red solid, index perturbation; black dotted, normalized refractive index.

Other considerations There are a couple of other elements required to be considered in the integrated device. Firstly, the optical modes, after leaving the pump region of the source, inevitably experiences losses both in power and horizontal confinement. The horizontal waveguide is chosen to be removed otherwise the diffraction efficiency by the acoustic wave is expected to be strongly reduced. The strong attenuation of optical power in MQW layers without current pumping is unavoidable, but the amount is expected to be small because of the very small confinement factor of the active layer. In fact, as seen in Fig. 5.6, in the etched-down region the peak of the optical mode shifts away from the active region and hence even less modal attenuation is expected in that region. Nevertheless, if there is some way to improve the mode propagation, QW intermixing technique could be one choice as a practical solution, [107][108].

Another possible problem is the power loss in the process of SAW excitation by IDT due to the leaky current from the electrodes to the grounded substrate. In the proposed case, the IDT is positioned on a GaN film. This problem thus becomes even more severe because of the inherent low resistance of undoped GaN. The insulation

of the top layer in the SAW region could be improved either by growing another layer of AlN [109] or GaN with Mg-doping [110].

5.4 Summary

This chapter proposes the idea of a guided wave AO processor integrated with a semiconductor optical source and the consideration in material and structure. It is found that GaAs and GaN are both candidates satisfying the twofold requirements from the integration nature of FISOS, and the design based on GaN is better because of the increasing interest in blue and ultraviolet wavelength applications. A typical multilayer structure based on GaN/InGaN MQWs is then given and the transverse and lateral modes profiles are calculated. An etch-down technique is suggested to be taken to increase the overlap between the optical and acoustic mode and then the interaction efficiency. The optimal etching depth is demonstrated in the given structure. Detailed analysis of the performance and characteristics of FISOS will be discussed in next chapter.

Chapter 6

FISOS Characteristics for Particular Operation

The concept and a reliable structure for a surface acoustic wave controlled AO device integrated with semiconductor optical source has been presented in the previous chapter. In that design a GaN/AlGaN multilayer structure deposited on *c*-Sapphire substrate is chosen to launch a surface acoustic wave and generate an optical wave and provide confinements to both waves for their efficient interaction. The traveling Bragg grating created by the guided acoustic wave, of which the characteristics can be readily altered by the property (power, frequency, .etc) of the SAW, operates a functional processing to the guided optical wave such as beam deflecting, modulating, convolving, filtering, mode converting, spectrum analyzing and so on. The FISOS device, in contrast with conventional passive AO devices along with an external source, provides an access to the potentially high performance of optical control with low fabrication and coating cost mainly because of the fact that the power loss and beam distortion when coupling light into/outof the waveguide is avoided and mature planar fabrication techniques can be employed.

The characteristic features and examples of applications of FISOS are presented in this chapter. Section 6.1 reviews the design considerations of the dimensions of the structure of FISOS. All parameters used in the modeling such as the optical wavelength and acoustic frequency ranges are given. Simulation results from previous chapters such as SAW distribution, optical mode profile and refractive index perturbation are summarized. In section 6.2 and 6.3 the angular and spatial field profiles of the integrated device with different combinations of parameters are

demonstrated. The performance range of the proposed device is discussed. A further investigation of the performance of the device, including diffraction efficiency of the guided optical mode and the FWHM (Full-Width-Half-Maximum) of the incident/diffracted optical modes, are presented in section 6.4. In order to evaluate the feasibility of the FISOS, two application examples are discussed. The practical design considerations and the performances with optimized parameters for an integrated modulator (temporal modulation) and beam deflector (spatial modulation), including bandwidth, throughput efficiency and number of resolvable spots, are discussed in section 6.5 and 6.6, respectively. Finally, in section 6.7, considerations about device tolerance such as the consequence of misalignment of planar elements and incoherent optical source, are investigated.

6.1 Parameter Selection and Optimization

Numerical methods are developed in this project to investigate the properties of the novel functional integrated semiconductor optical source. The cascaded transfer matrix method is used to analyze the lateral and transverse optical modes excited by the integrated GaN optical source. The coupled-mode method is used to evaluate the fraction of the diffracted power of an incident divergent optical beam analyzed by the plane wave (PW) decomposition approach. The SAW is generated by an IDT, of which the frequency response, the insertion loss and the admittance are solved by the transmission line model. The frequency dispersion and the distribution of the SAW are simulated by Adler's transfer matrix method. Those numerical simulations provide an evaluation of the characteristics of each aspect of the integrated device and following the simulation results the appropriate parameters can be chosen and the optimization to the parameters corresponding to different applications can be achieved.

6.1.1 Parameter Consideration in FISOS

The main task of the FISOS design is to optimize the device configuration in order to balance the diverse requirements from the integrated elements, improve the diffraction efficiency, increase the operating bandwidth of the device and minimize the loaded acoustic power, hence also the rf power. The optimization can be pursued

literally in two directions, transverse and lateral.

Since the GaN/AlGaN multilayer structure is designed primarily to achieve efficient photon emission, the transverse structure given in figure 5.1 is more or less decided by this requirement in the proposed device. From the viewpoint of the overlap between optical and acoustic modes, the optimization of the structure in the SAW region i.e. the etch-off of the top layers, has been represented in section 5.3. It was demonstrated that, after etching off 700nm of top layers, the overlap integral increases from 0.5% to 6.5% without too much distortion introduced to the transverse optical mode. Thus an etch-down of 700nm is decided in this design. A typical value of the index perturbation of 1×10^{-4} created by an acoustic wave propagating in this etch-down region with a loaded power of a couple of mW is achieved. Additionally, the guideline about the optimization to properties of the lateral planar elements, such as optical divergence, the AO interaction length, IDT structure and position, as illustrated in figure 6.1, are to be discussed in the rest of this section.

Optical source The lateral confinement along the x-axis in the GaN optical source is obtained by an etched ridge waveguide of width a, figure 6.1. The optical modes excited by this optical source can be calculated by the approach of cascaded transfer matrix (Appendix E). The form of the electric field is assumed to be

$$E(x', y, z) = \nu_m(y) \cdot h_{mn}(x', z) \tag{6.1}$$

where m and n are integers denoting specific modes and the time dependence is omitted. TE polarization of electric field is assumed in the modeling. This quasi-scalar electric field analysis is used throughout the interaction between optical and acoustic waves. Though multiple transverse (y-axis) modes are supported by this structure, the diffraction of the fundamental modes (both transversely and laterally, incident and diffracted) are considered throughout this thesis but the calculation involving different modes has been discussed in section 4.3.

As presented in the previous chapter, in the case of AO interaction between guided waves, the transverse mode shapes of the optical incident and diffracted waves are of very important concern because they strongly influence the value of the overlap integral with the acoustic waves, and then the diffraction efficiency. The overlap integral is expected to be much smaller than unity if the optical mode is

diffracted into another mode (or TM polarization). The lateral optical mode also plays a significant role in the performance of AO interactions. This issue will also be addressed in section 6.5 and 6.6. The lateral divergence is solely determined by the ridge waveguide width a. This ridge is produced by an etch-off of a typical thickness 120nm. The value of a is chosen to be 500nm$\sim$2μm and only a single mode is supported within this range.

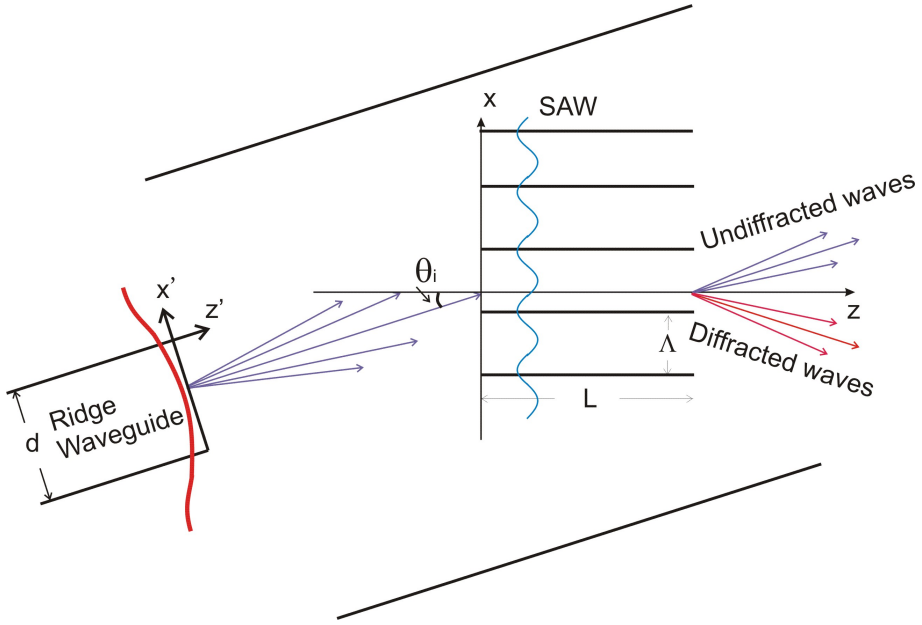

Figure 6.1: Schematics of the topview of the FISOS.

Acoustic porcessor From the viewpoint of crystalline orientation, the epitaxial GaN film is chosen to grow in [001] direction of a wurtzite structure on the (001) plane (c plane) of sapphire. The acoustic wave is taken to be excited by an IDT with electrodes parallel with Y-axis and propagating along X-axis (XYZ, the crystalline internal coordinates system) or as illustrated in figure 6.1 (xyz, laboratory coordinates system) and a rotation of physical parameters needs to be done.

The velocity dispersion and transverse distribution of Rayleigh wave in the proposed layered structure is simulated by Adler's matrix method [43] in the frequency range from 500MHz and up to 2GHz due to the increasing interest in high frequency devices. It will be demonstrated in section 6.2 that the trend of the incident and diffracted waves start to merge with each other with decreasing acoustic frequency, making the AO device unreliable for frequencies lower than 500MHz. On the other hand, due to the instability of the matrix method used at high frequency, 2GHz is almost the highest working frequency for the solvable SAW excitation in the present

GaN/Sapphire layered structure. The Rayleigh velocity up to 5199m/s is obtained for 500MHz and as low as 4276m/s for 2GHz working frequency.

The IDT is supposed to be made of aluminum/gold film of thickness ∼100nm deposited on the surface of the etch-down region and composed of N pairs ($\sim 10^2$) of identical electrodes of uniform length L, and spacing length equivalent to the desired acoustic wavelength corresponding to the working frequency. The frequency response of the IDT and its associated impedance and insertion loss, which relies on the material, the frequency, the length L and the number N, has been discussed in section 2.4. The number of pairs of electrodes N, is found to be only concerned with the electrical property, such as impedance and insertion loss, but have nothing to do with the acoustooptic interaction. Therefore, only the parameter of L will be discussed afterwards, provided that the IDT bandwidth is assumed to be sufficiently large and the mismatch between the electrode spacing and acoustic wavelength does not affect the AO efficiency strongly. The length of L, which is also the acoustic wave aperture, can be used to estimate the acoustic beam width, $\delta\theta_a \approx \Lambda/L$. From the viewpoint of acoustooptic effect, L as the AO interaction length relates inversely to the acoustic power, i.e. longer L gives a saving in acoustic power when the same efficiency is obtained.

Figure of merit As introduced in section 1.2, a figure of merit Q is defined determining diffraction regimes. For Bragg diffraction, Q must be greater than 2π otherwise higher orders of diffracted beams occur and the diffraction efficiency for the desired optical beam falls. This condition serves as a basic restriction to the choice of parameters and will be discussed in detail afterwards.

6.1.2 Trade-offs in AO device Design

The design consideration of a monolithically integrated AO modulator or deflector is quite similar with the separated devices except that the incident optical beam has an angular spectra inversely proportional to the ridge width. To achieve wide modulation bandwidth, the optical beam must be focused to a small width, i.e., the optical divergence needs to be large (equation (6.16)). Besides, to maintain an overall efficient modulation, a sufficiently large divergence of acoustic beam is essential to operate the diffraction with each component of the entire optical beam. The momentum conservation law for Bragg diffraction requires that the momentum

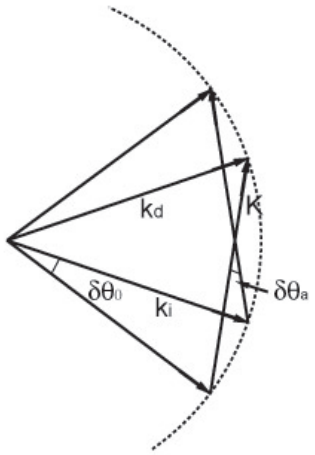

Figure 6.2: Momentum conservation for wave vectors of optical and acoustic waves with divergences.

vector $\boldsymbol{k}_d$ of the diffracted light beam is equal to the vector sum of the momentum vector $\boldsymbol{k}_i$ of the incident light beam and the momentum vector $\boldsymbol{K}$ of the acoustic beam; i.e., the vector relation $\boldsymbol{k}_d = \boldsymbol{k}_i + \boldsymbol{K}$ holds. The incident light beam has a range of $\boldsymbol{k}_i$ vectors of weighted magnitudes and distributed over an angular range $\delta\theta_0$ since the light beam is divergent. For the vector relation to be satisfied, the angular width of the acoustic beam $\delta\theta_a$ must be larger than the optical one. This condition for matching the angular spreads of the acoustic and optical beams is indicated in Figure 6.2. Since the acoustic beam width can be evaluated by the magnitude of Λ/L, this gives a trade-off for the parameter selection in modulator design: wide bandwidth requires a small L, which yet will lead to the diffraction efficiency reduction since the efficiency is proportional to L for weak Bragg diffraction described in equation (3.45).

A similar trade-off exists in AO deflector design as well. The key parameter for a deflector used in a signal processor is the number of resolvable spots N. The number N can be determined by the ratio of the maximal deflection angle divided by the angular spread of the optical beam and $N \propto 1/L$, and the efficiency-N trade-off will be discussed in detail in section 6.5.

In summary, given the multilayer structure of GaN laser/LED along with an etched-down SAW region, there are a series of parameters to be specified and their effects to be analyzed, such as the acoustic frequency, the lateral ridge waveguide width and the IDT electrode length. The magnitudes of those variables will be

discussed and optimized corresponding to specific considerations so as to balance the trade-off.

6.2 Angular Profile of the FISOS Output

An optical beam emitted from the active region of the optical source is scattered in the $x-y$ plane after leaving the ridge waveguide and loses the lateral confinement (while the transverse confinement stays), as shown in figure 6.1. A scalar plane wave decomposition of the lateral mode yields the PW angular spectrum, [111]

$$A(\theta') = \int_{-\infty}^{\infty} h_{00}(x') e^{jn_{\text{eff}} k_0 \sin\theta' x'} dx \tag{6.2}$$

and each PW has the form

$$E_{PW,\theta'}(x', z') = A(\theta') e^{-jn_{\text{eff}} k_0 (\sin\theta' x' + \cos\theta' z')} \tag{6.3}$$

which has been discussed in Chapter 4 (equation (4.22)). This group of PWs are readily considered to be the input of the Bragg grating formed by the acoustic wave. To be consistent with the analysis described in chapter 3, the coordinates system is rotated by an appropriate angle to (x, y, z), the z-axis of which is to be parallel with the wavefronts of the SAW. The angle between the incident optical mode and the SAW wavefronts must be precisely equal to the Bragg angle determined by the optical and acoustic wavelength, so as to satisfy the Bragg condition and attain a maximal efficiency.

For each PW, the approximated coupled-wave method, introduced in section 3.2.2 is employed and the intensities of diffracted PWs are calculated. Hence the angular distributions of the diffracted optical beam are obtained and the angular distribution profiles at different acoustic frequencies are discussed in this section.

The ridge width a is chosen to be 2μm, with which only the fundamental mode is supported. The effective index for the transverse optical mode propagating in the multilayer structure of the etch-down region is $n_{\text{eff}} = 2.45$ and this value holds for the diffracted mode. The transducer width L, which is also the AO interaction length, is chosen to be 500μm and this magnitude gives the AO figure of merit $Q > 2\pi$ for the chosen acoustic frequency, which ensures the availability of the calculation for Bragg diffraction.

Firstly, as a reference, the diffraction efficiency versus acoustic power ((3.46)) injected into SAWs of frequencies 500MHz, 1GHz, 1.6GHz and 2GHz is illustrated in figure 6.3. These curves are obtained for the case of a single plane wave incidence. Bragg condition is satisfied for diffraction with each acoustic frequency. Since for plane wave incidence, the diffraction efficiency is in the simple form of $\sin^2(f)$ (equation (3.45)), its value performs some shift for different working frequency. For example, when 23.3mW of power is applied, the efficiency is up to 100% for an AO interaction with a SAW of 2GHz , whilst it is reduced to 67% for the same power of SAW at 1GHz. Those efficiency variation when altering the applied acoustic power is obvious in the simple case. Howerever, in the case of diffraction problems of a broad optical beam, this relation might not stay the same. In figure 6.3, in practice, such a large acoustic power is more than enough to launch an efficient diffraction. The reason of choosing an operating power range like this is to illustrate the limitation of the conventional definition of diffraction efficiency, although such limitations also exists for smaller acoustic power.

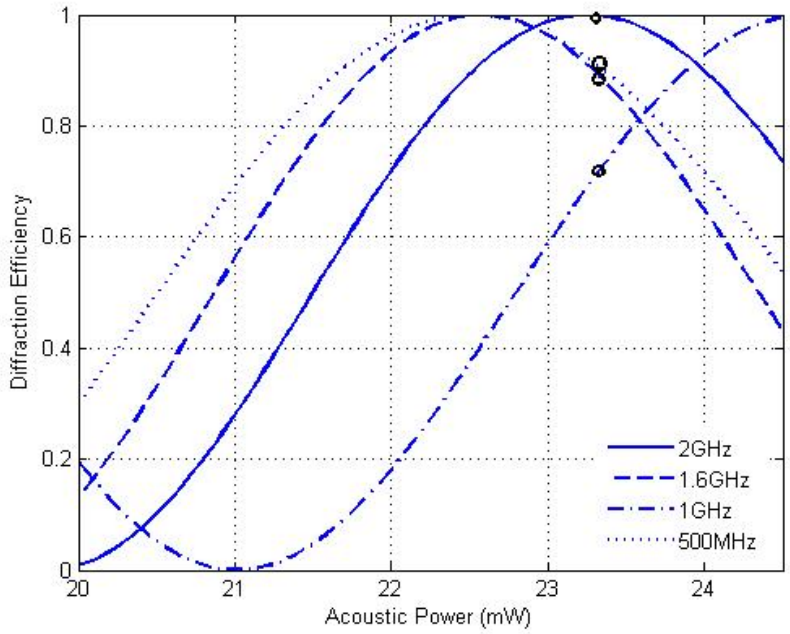

Figure 6.3: Diffraction efficiency varying with loaded acoustic power at frequencies 500MHz ($\cdots$), 1GHz $\cdot-$, 1.6GHz $--$ and 2GHz $-$ when an optical plane wave is diffracted. The marked circles indicate the efficiencies obtained by SAWs by the same injected power.

The far angular distribution of incident optical waves interacted with SAW of different acoustic frequencies are illustrated in figure 6.4. The Bragg condition is

still satisfied separately for the central component of the incident optical waves and acoustic wave. The loaded acoustic power of 23.3mW is chosen (referencing to figure 6.3) to distinguish the properties at different frequencies though smaller power is also possible. In figure 6.4a, the incident optical wave is diffracted by a SAW of 2GHz at a Bragg incident angle 2.2°. Little optical power is left along the incident direction after the interaction, indicating very high efficiency obtained for the whole group of waves. It is noticed that the intensity of the PW component which exactly follows the Bragg angle of incidence falls to zero as expected. The remaining power of PWs along propagating directions adjacent to the Bragg angle implies the possibility of the beam width control to the diffracted waves and beam profile flattening of the undiffracted waves.

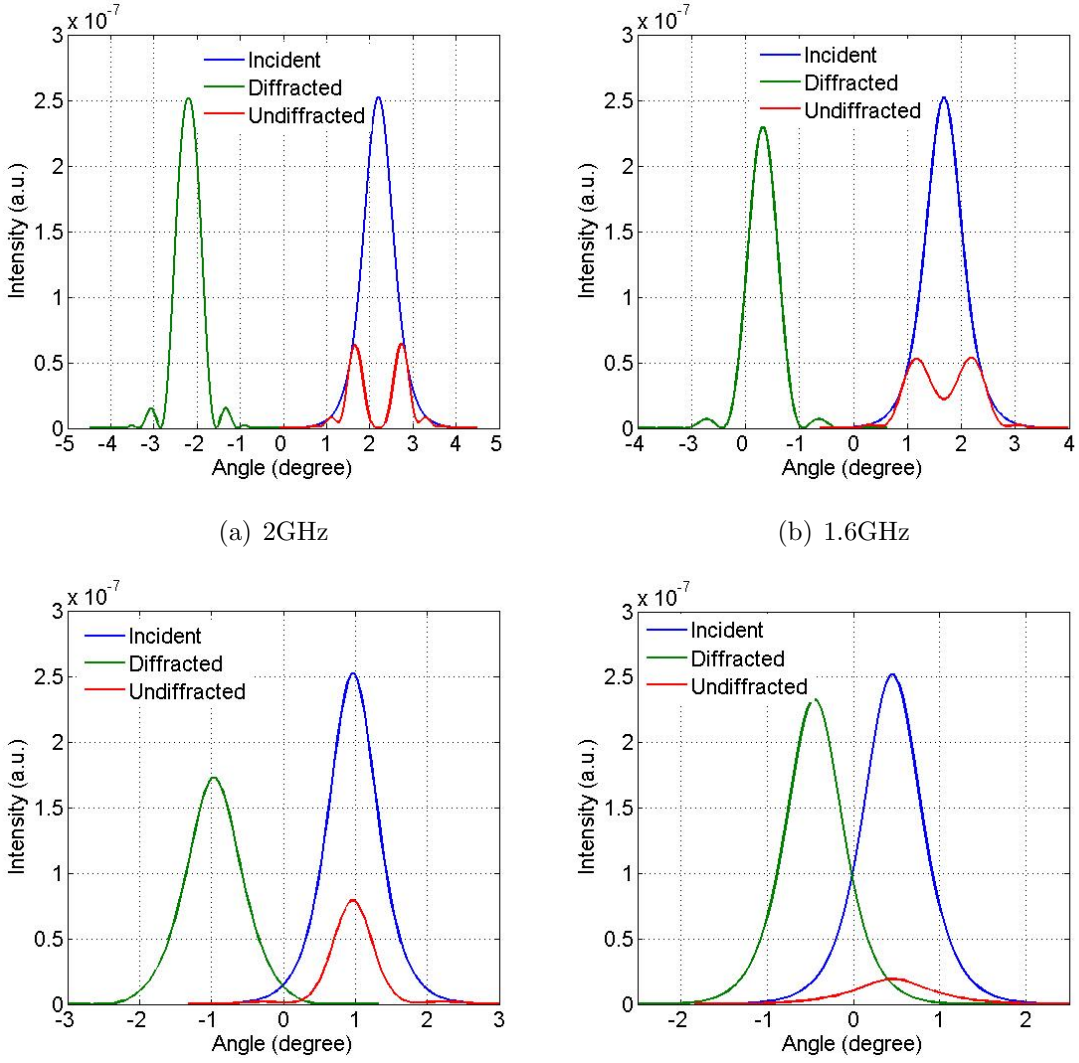

(a) 2GHz

(b) 1.6GHz

(c) 1GHz

(d) 500MHz

Figure 6.4: Angular distributions of the incident (blue) optical mode, diffracted optical mode (green) and undiffracted mode(red) at different acoustic frequencies as titled.

Similar angular distributions at 1.6GHz is shown in figure 6.4b. The angular distance of incident and diffracted modes becomes smaller and the maximal efficiency is strongly reduced. In figure 6.4c for 1GHz SAW, the diffracted and undiffracted beams start merging with each other but are still recognizable. When the SAW frequency reduces to 500MHz, figure 6.4d, the undiffracted mode has almost entirely merged into the diffracted one so that such a low frequency makes the device not appropriate for applications in which the recognizable undiffracted beam is required.

Particularly, according to figure 6.3 the diffraction efficiency of a plane optical wave with a 1.6GHz acoustic wave of 23.3mW is supposed to be much larger than the one at 1GHz. However, it appears that the differencies between the overall diffraction efficiencies in two cases of figure 6.4b and c, are at the same level. Besides, although the diffraction efficiency of the central component of the incident beam is low at 84% at frequency 1.6GHz (see figure 6.3), the fact that higher efficiency is obtained by some PW components(6.4b) might yield an actually larger efficiency for the incident beam. These possible deviations make it necessary to develop a improved approach to describe the diffraction efficiency more precisely for an incident optical wave with large divergence, which will be discussed in section 6.4.

6.3 Spatial Profile of the FISOS Output

In order to achieve the spatial profile of the diffracted beams, a Fourier transform is performed to transfer the diffracted waves from the frequency domain (angular spectrum) to the spatial domain. Using the amplitudes of diffracted wave $U_{-1}(L,\theta_d)$ and undiffracted wave $U_{0L}(L,\theta_i)$, the total field is obtained

$$E_{x,z} = U_1(L,\theta_d)e^{-jn_{\text{eff}}k_0(\cos\theta_d z+\sin\theta_d x)} + U_{0L}(L,\theta_i)e^{-jn_{\text{eff}}k_0(\cos\theta_i z+\sin\theta_i x)} \tag{6.4}$$

where θ_i and θ_d indicate the associated propagation direction of incident and diffracted PW component. The configuration of the system parameters is kept the same as used in the previous section: $a = 2\mu$m, $L = 500\times10^{-6}\mu$m and $P_a = 23.3$mW. The spatial profile at different SAW frequencies, from 500MHz to 2GHz, are illustrated here, figure 6.5$\sim$6.8, in the form of three sub figures: the 3-dimensional view of the electric field in x-z plane with the field intensity as the z-axis, the topview of the intensity with the SAW absent and topview with the SAW

present.

As expected, the optical wave propagates along its original direction when the acoustic wave is absent; efficient diffractions are well performed in all cases with the SAW of the given power supply; the separation between incident and diffracted beams (equal to $2\theta_B$) becomes wider when the frequency increases. Figure 6.8 confirms that the diffracted beam merges with the undiffracted one with the given parameters.

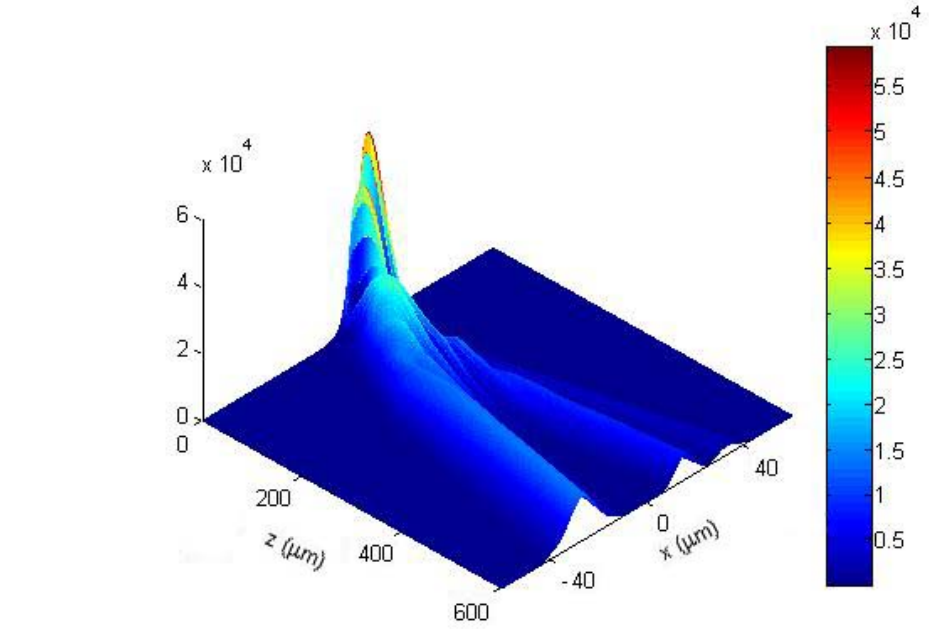

(a) 3-dimensional view

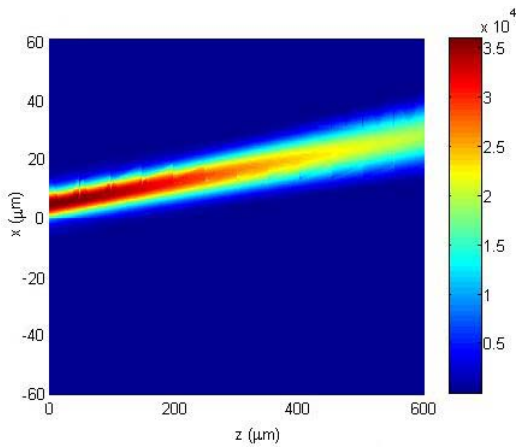

(b) Top view without SAW

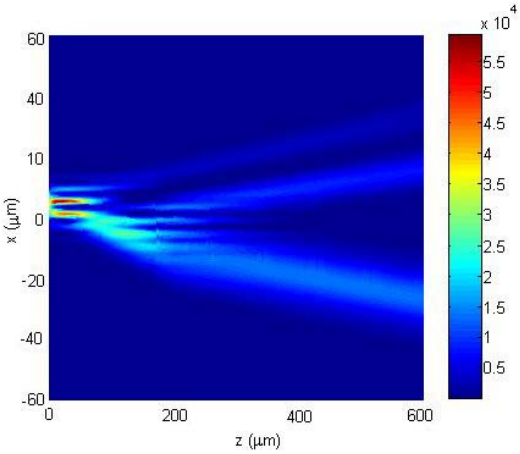

(c) Top view with SAW

Figure 6.5: Spatial profiles of the output of acoustic grating of frequency 2GHz.

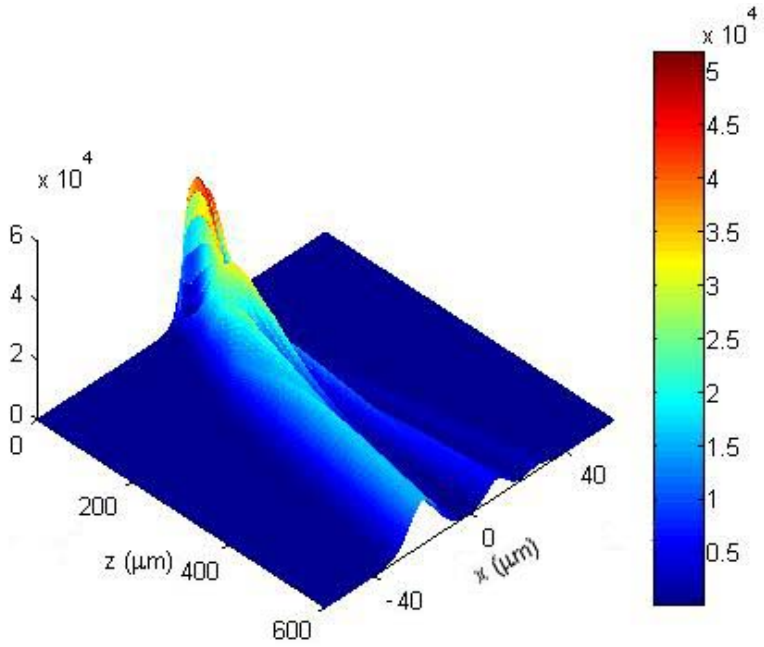

(a) 3-dimensional view

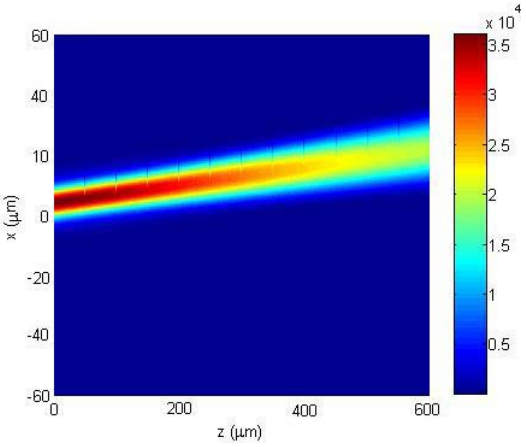

(b) Top view without SAW

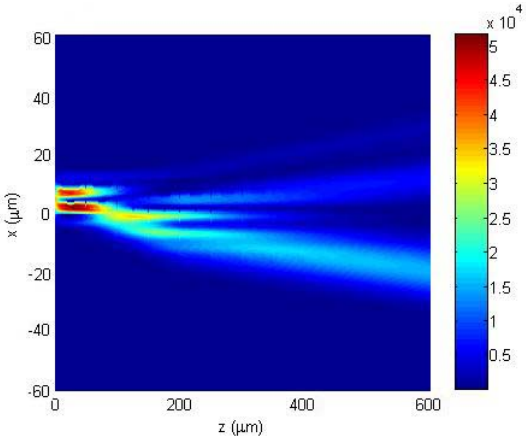

(c) Top view with SAW

Figure 6.6: Spatial profiles of the output of acoustic grating of frequency 1.6GHz.

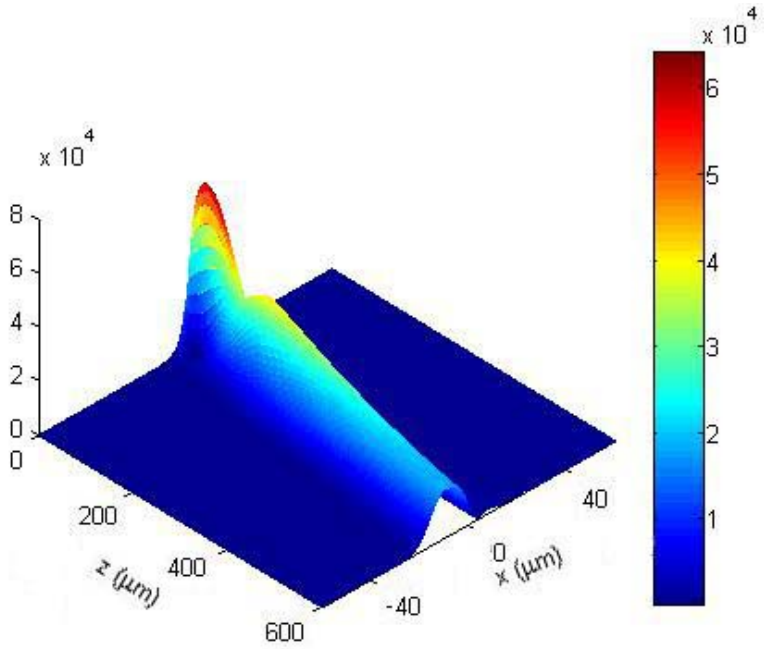

(a) 3-dimensional view

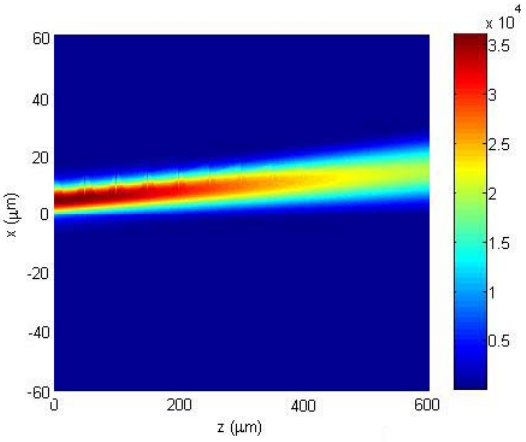

(b) Top view without SAW

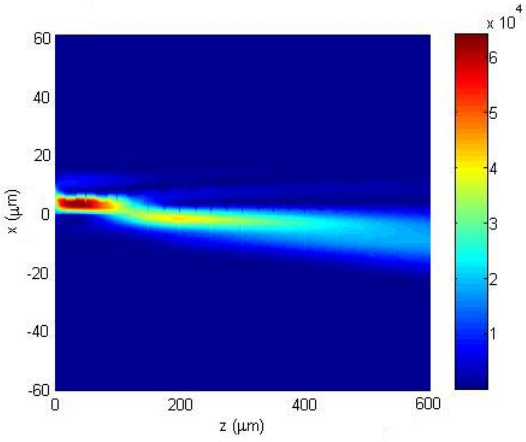

(c) Top view with SAW

Figure 6.7: Spatial profiles of the output of acoustic grating of frequency 1GHz.

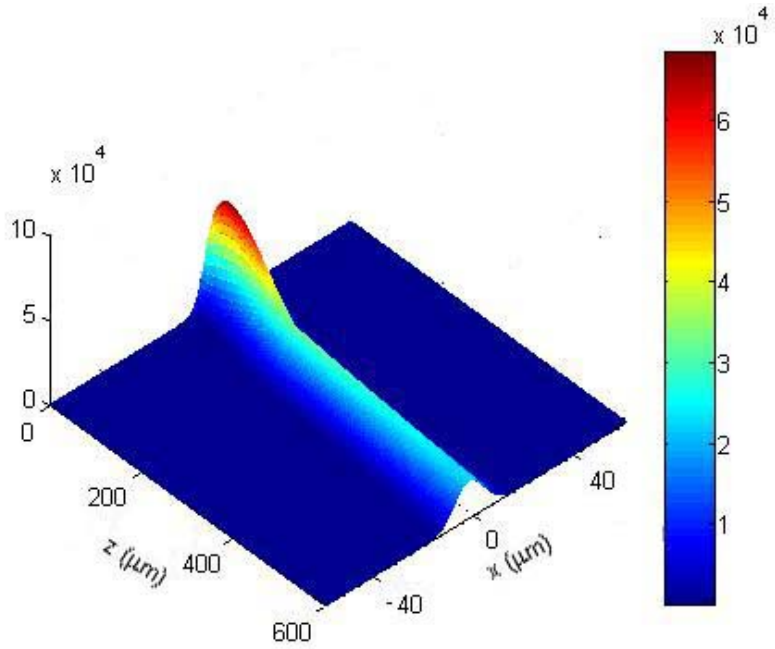

(a) 3-dimensional view

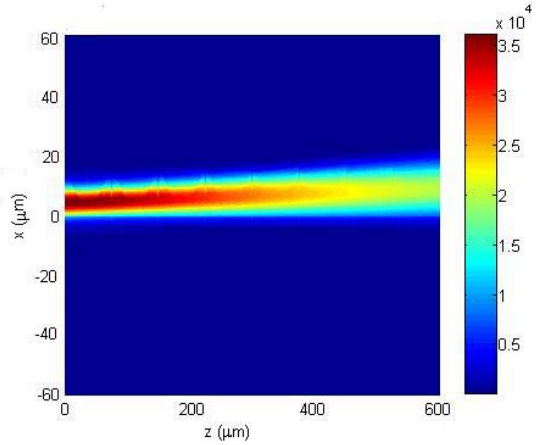

(b) Top view without SAW

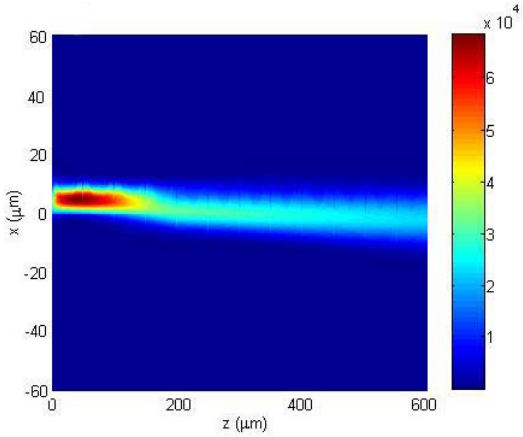

(c) Top view with SAW

Figure 6.8: Spatial profiles of the output of acoustic grating of frequency 500MHz.

6.4 Improved Expression of Diffraction Efficiency

It is realized that the usual expression of diffraction efficiency given in equation (3.43), which is broadly used in analysis on AO device with either collimated optical beams or focused Gaussian beams [93][88], is not able to precisely describe the diffraction performance in the optical source integrated AO device due to the unavoidably large divergence of the optical beams. The deviation introduced by using the efficiency calculated by the central PW instead of the whole beam, will become larger when the divergence of incident waves increases. The evaluation and optimization of associated performances, like bandwidth or number of resolution of spots, of practical devices will tend to be unreliable.

To rectify this problem an improvement in the calculation of diffraction efficiency is needed. In fact, a method to evaluate the effective efficiency of Gaussian beam incidence was firstly proposed by Magdich and Molchanov in 1980 [112] and then reviewed by P.Maak in 1999 [113]. In this method the efficiency is defined as the fraction of the power integrating over the plane wave spectrum of the diffracted optical beam out of the entire incident power. The same concept is used here and the so-called beam diffraction efficiency is defined

$$\eta = \frac{\int U_1(\theta_d) e^{-jn_{\text{eff}}k_0(\cos\theta_d z + \sin\theta_d x)} [U_1(\theta_d) e^{-jn_{\text{eff}}k_0(\cos\theta_d z + \sin\theta_d x)}]^* d\theta_d}{\int U_0(\theta_i) e^{-jn_{\text{eff}}k_0(\cos\theta_i z + \sin\theta_i x)} [U_0(\theta_i) e^{-jn_{\text{eff}}k_0(\cos\theta_i z + \sin\theta_i x)}]^* d\theta_i} \tag{6.5}$$

When the diffracted and undiffracted beam are very close to each other, for instance, figure 6.4d, the result given by equation (6.5) loses its clear physical sense. However, this value still provides an appropriate estimation of the diffraction effect when the acoustic frequency is low.

In order to give a full image of the influence to the efficiency from the acoustic frequency and carried power, contour plots of the beam diffraction efficiency with different parameters are demonstrated here. The ridge width is fixed to be 2μm and it is assumed that the Bragg condition keeps satisfied for each combination of SAW frequency and power. The two dimensional illustrations of efficiency for the AO interaction length 100μm, 50μm and 36μm are shown in figure 6.9. A reference colour bar is also displayed to show the magnitude level of efficiency.

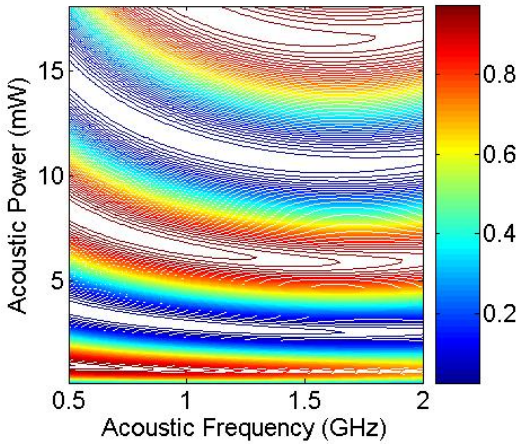

(a) $L = 100\mu$m

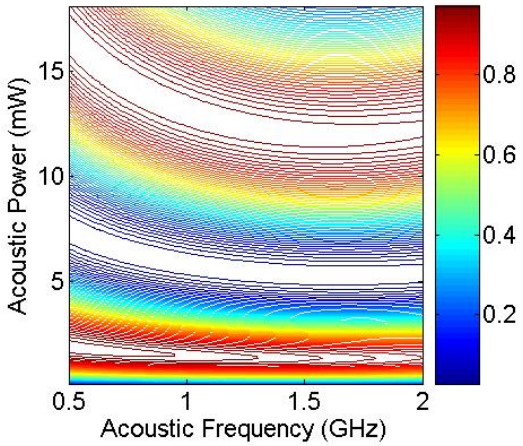

(b) $L = 50\mu$m

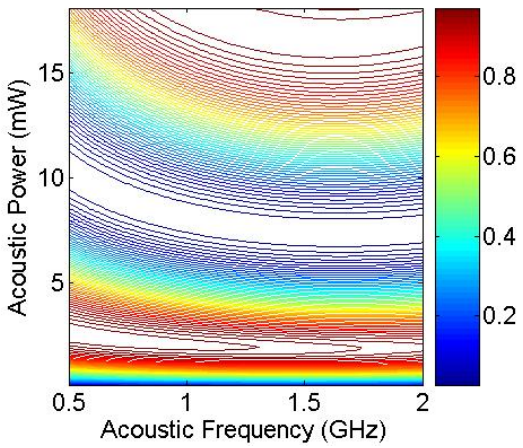

(c) $L = 36\mu$m

Figure 6.9: Contour of beam diffraction efficiency as function of acoustic power and frequency with different AO interaction lengths as titled.

It is noted that very high diffraction efficiency are all obtained for different lengths of AO interaction. Noticing the trends of each contour plot along both axes, the diffraction efficiency is more sensitive with acoustic power at high frequency than low, and this sensitivity strongly depends on L; higher efficiency is usually achieved at lower acoustic frequency if the injected acoustic power is fixed. As an example, the diffraction efficiency versus acoustic power (blue) at 2GHz frequency is shown in figure 6.10. The first peak of the efficiency curve occurs at $P_a \approx 1$mW. When the acoustic power is increased to be over 6mW, the efficiency obtained is high to 93%. Compare this with the experimental results by Bu (2004) [93] in a AlGaN-on-sapphire structure, that the first efficiency peak (95%) occurs at $P_a = 20$mW; if the insertion loss of -23dB of IDT in his system is considered, the estimated power carried by the SAW from the simulation result has good agreement with his data. The reason that the simulation efficiency (first peak, 72%) is lower than than the experimental result (∼100%), is that laterally the optical wave in Bu's system is well collimated rather than a divergent optical beam used here.

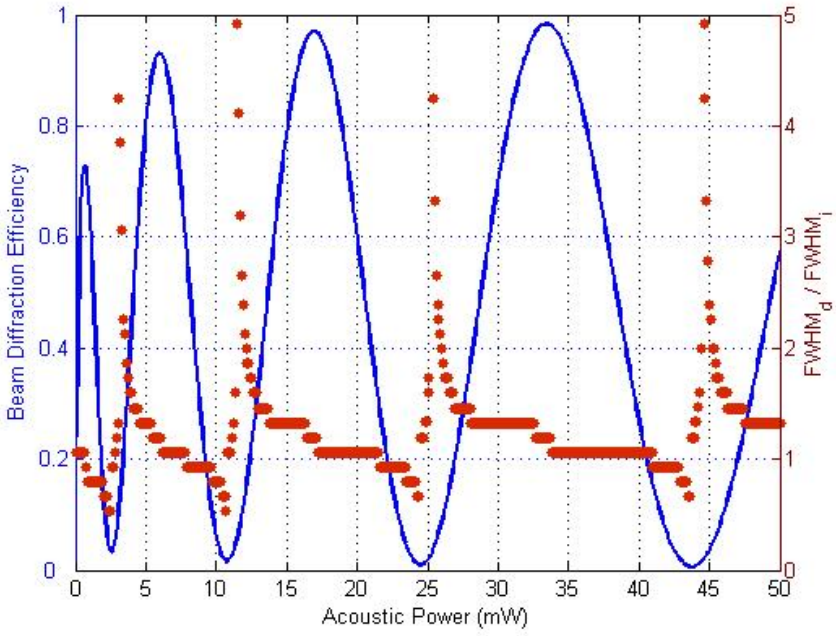

Figure 6.10: Beam diffraction efficiency and FWHM of the diffracted optical beam as function of acoustic power. Blue, left axis; red, right axis

The study of beam width control by acoustic power is also considered. The FWHM (Full-Width-Half-Maximum) of optical beams is defined as the angular width at 3dB below the peak intensity. The ratio of the FWHM of the diffracted

beam over the value of the incident one varying with acoustic power is exhibited in figure 6.10 (red). It is found that the beam width of a diffracted beam could be reduced to half of the incident one with the cost of low efficiency. With most of the driven acoustic power, the diffracted beam is expanded by a slight amount.

In order to give a guideline for the design of a device with diffraction efficiency as the first concern, the maximal efficiency achieved at a given loaded power as well as the corresponding acoustic working efficiency are demonstrated in figure 6.11 with different AO interaction length. A similar conclusion to the contour plot has been obtained, that the peaks of efficiencies are achieved at smaller acoustic power for shorter interaction length. Besides, the peaks of the maximal efficiency curves are found to be mostly at a lower frequency, particularly for the first peak, but in some power range higher frequency SAW does work better. Notice that the cut-off frequencies appearing in each figure (1.17GHz in figure 6.11a, 1.57GHz in figure 6.11b and 1.8GHz in figure 6.11c) are caused by the limit from the figure of merit Q which must be larger than 2π otherwise the results obtained with the Bragg diffraction approximation will not be reliable.

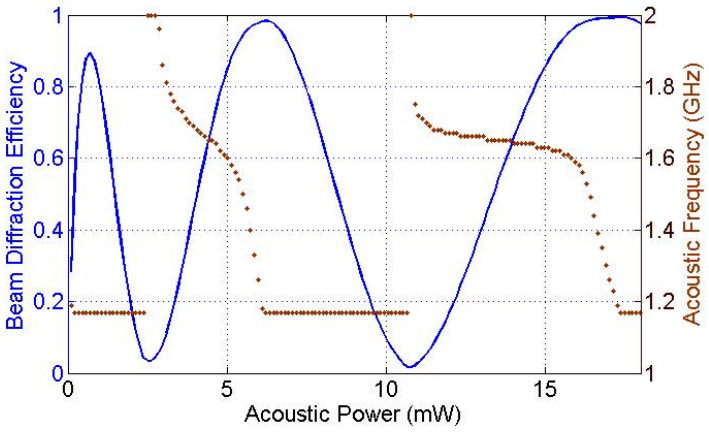

(a) $L = 100\mu$m

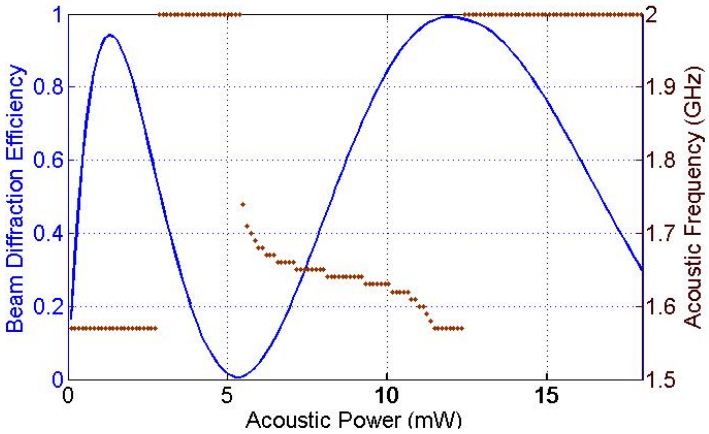

(b) $L = 50\mu$m

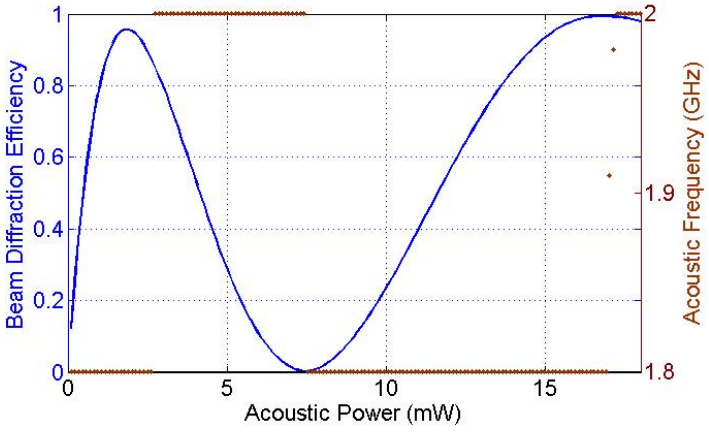

(c) $L = 36\mu$m

Figure 6.11: The maximal beam diffraction efficiency and the acoustic frequency at which the peaks are obtained as a function of acoustic power. Cases with different AO interaction lengths as titled are exhibited. Blue, left axis; red, right axis.

6.5 Application with an Integrated AO Deflector

Planar AO deflectors can be divided into two types. In the first one the incident and diffracted light waves are both transversely guided by the optical waveguide whilst in the second type of deflector, the acoustic surface wave deflects the incident guided light out of the waveguide escaping in the form of radiation mode [114]. Only the first type deflector is discussed here, which was firstly experimentally demonstrated by Kuhn in 1970 [63] and improved in the last four decades [115]∼[91].

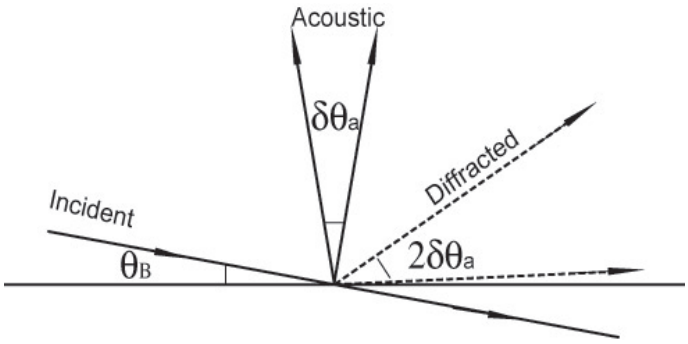

Figure 6.12: Interaction of an optical beam with an acoustic beam having a divergence of $\delta\theta_a$.

Suppose the acoustic beam has a finite angular divergence $\delta\theta_a$,

$$\delta\theta_a \approx \Lambda/L \tag{6.6}$$

while the incident optical beam has a very small divergence, then there will be a range of incident angles for which the incident light will be diffracted by one acoustic plane wave component making the Bragg angle corresponding to the incident light beam, as shown in figure 6.12. The frequency range Δf over which the Bragg condition is satisfied is thus given from the definition of θ_B, equation (3.44), assuming $\theta_B << 1$

$$\Delta f = \frac{2nv_R}{\lambda_0}\Delta\theta_B \tag{6.7}$$

and it is known that the angle of deflection $\theta_d = 2\theta_B$, see figure 6.12, therefore it gives that

$$\Delta\theta_d = 2\Delta\theta_B = 2\delta\theta_a \tag{6.8}$$

and

$$\begin{aligned} \Delta f &= \frac{2nv_R}{\lambda_0}\delta\theta_a \\ &= \frac{4\pi}{Q}f \end{aligned} \tag{6.9}$$

where the definition of AO figure of merit $Q = \frac{2\pi\lambda L}{n\Lambda^2}$ is used. Since the diffracted optical beam has a finite angular spread, the quantity of interest in a deflector is the number of resolvable spots N, i.e. the number of independently addressable directions. If $\delta\theta_0$ is the angular divergence of the optical beam, combining equation (6.10) gives

$$\begin{aligned} N &\approx \frac{\Delta\theta_d}{\delta\theta_0} \\ &= \frac{4\pi\lambda}{Q\Lambda\Delta\theta_0} \end{aligned} \tag{6.10}$$

The derivation of equation (6.10) also uses the definition of Q. It is known that the magnitude of Q must be greater than 2π to ensure the Bragg diffraction, therefore this condition yields the restrictions for the bandwidth Δf and number of resolvable spots N

$$\Delta f \leq 2f \tag{6.11}$$

and

$$N \leq \frac{4\theta_B}{\Delta\theta_0} \tag{6.12}$$

Hence it can be concluded that the bandwidth of a reflector can be up to double its working frequency while the maximum of its resolution spot number is inversely proportional to the optical divergence and proportional to the associated Bragg angle. In order to achieve a larger bandwidth and N, a small Q, thus a short L, and a high acoustic frequency must be chosen.

Given the magnitude of interaction $L = 28.4\mu$m calculated by $Q = 2\pi$ and $f = 2$GHz, the contour plot of beam diffraction efficiency varying with acoustic frequency and power with the ridge width $a = 2\mu$m is illustrated in figure 6.13

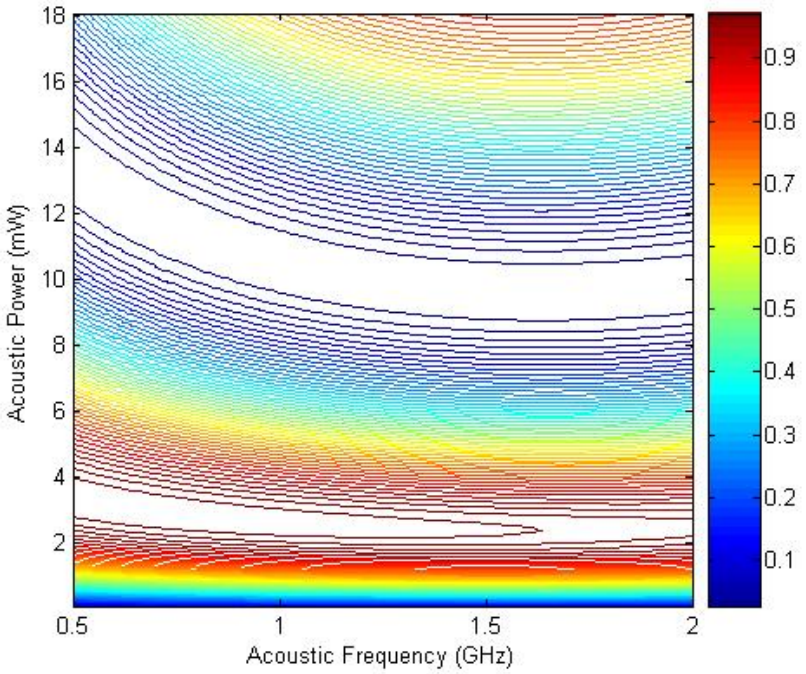

Figure 6.13: Contour of beam diffraction efficiency as function of acoustic power and frequency with AO interaction length $L = 28.4\mu$m.

From figure 6.13 it is noticed that the first peaks of efficiency appear in the power range of 2mW∼4mW, and higher efficiency is achieved for lower frequency. In order to find out the best combination of power-frequency pair, a plot of the maximal efficiency achieved in the power range 2mW∼4mW at frequencies from 500MHz to 2GHz is illustrated as well as the magnitude of N in figure 6.14. For the comparison purposes both curves with shorter ridge width $a = 0.5\mu$m are plotted as well. As expected, for both value of ridge width, the number of resolvable spots achieve their peak values at $f = 2$GHz and the number for smaller a is double the number for larger a, reflecting the fact that a smaller ridge with gives smaller optical divergence. The beam diffraction efficiencies for both ridge width do reduce their values when frequency increases, but even the lowest efficiency (96.7%) is believed to be acceptable.

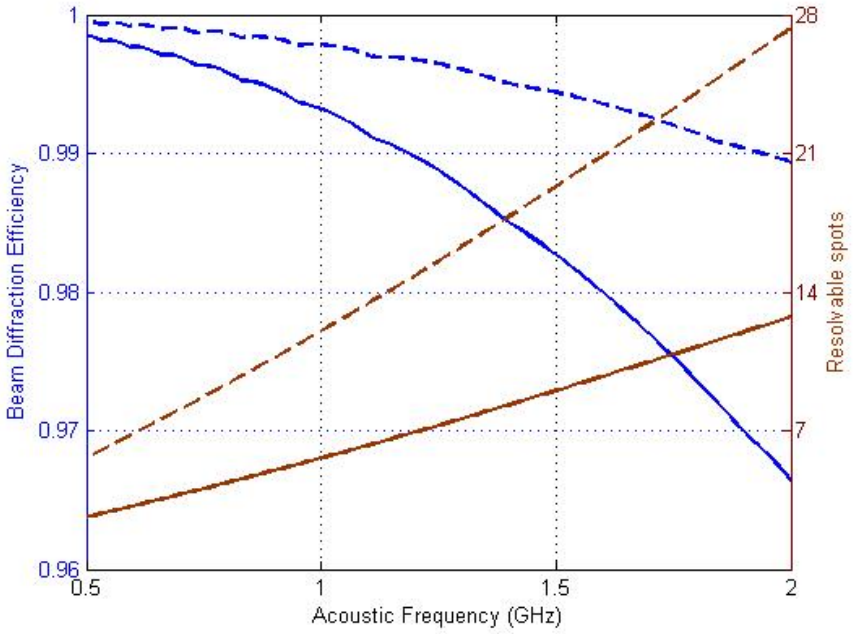

Figure 6.14: Beam diffraction efficiency and number of resolvable spots varying with acoustic frequency. Blue, left axis; red, right axis. Solid, $a = 2\mu$m; dashed, $a = 0.5\mu$m

Compared with the conventional deflector made by other material with an external source, the value of N is much smaller than the typical values ($\sim$1000)in the literatures [82]. It is not surprising due to the fact that there exists a naturally large optical divergence and no particular collimating procedure has been taken.

6.6 Application with an Integrated AO Modulator

In order to find out the expression of the bandwidth of a modulator, the schematic of an incident optical beam with a beam width $\delta\theta_0$ Bragg-diffracted by an acoustic beam with frequency f and f' each with a beam width $\delta\theta_a$ is plotted in figure 6.15. Optical beam AO and BO are reflected respectively by a selected acoustic beam with frequency f to beam OD and OC. If considering an acoustic beam with $f' > f$, this Bragg angle $\theta'_B > \theta_B$ and the optical beam AO may pick up a proper acoustic beam with f' and be deflected to a position OE. The largest f' such that the optical beam diffracted by acoustic beam at f and f' overlap angularly is such that the diffracted optical beam by f' along OE.

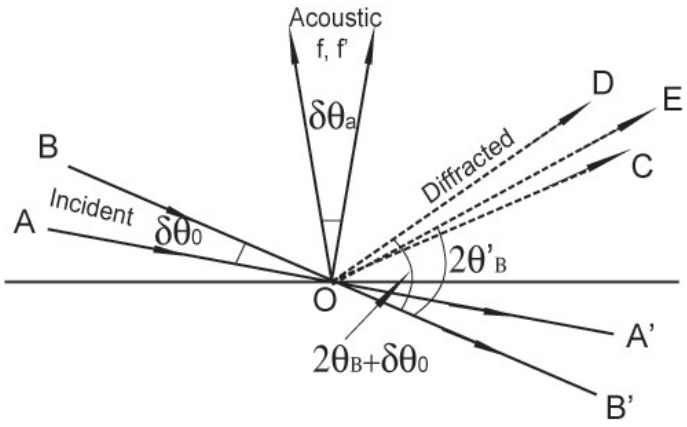

Figure 6.15: Optical beam incident over an angular region $\delta\theta_0$ interacting with acoustic beam at frequencies f and f' and having a divergence $\delta\theta_0$. The optical beam incident along the direction AO and BO are diffracted along OC and OD respectively by acoustic beam of frequency f_0.

It is known that the angle between the undiffracted and diffracted beam is twice the Bragg angle. Therefore the overlap mentioned above will occur if $2\theta' < 2\theta_B + \delta\theta_0$, the largest f' such that the diffracted wave is modulated corresponds to

$$\theta'_B = \sin^{-1}\frac{\lambda f'}{2nv_R} = \theta_B + \frac{1}{2}\delta\theta_0 \tag{6.13}$$

or

$$\begin{aligned} f' &= \frac{2nv_R}{\lambda_0}\sin(\theta_B + \frac{1}{2}\delta\theta_0) \\ &\approx f_0 + \frac{nv_a}{\lambda}\cos\theta_B\delta\theta_0 \end{aligned} \tag{6.14}$$

where it is assumed $\delta\theta_0 << 1$ using the relation

$$f_0 = \frac{2nv_R}{\lambda_0}\sin\theta_B \tag{6.15}$$

From equation (6.14), the maximum modulation frequency, i.e. the bandwidth, is obtained

$$\Delta f_{\max} = \frac{nv_a}{\lambda}\cos\theta_B\delta\theta_0 \tag{6.16}$$

Thus the larger $\delta\theta_0$ and v_a are, the larger the bandwidth will be. Another restriction, that the undiffracted and diffracted beam may not overlap with each other, can be found from figure 6.15 as well, that is

$$\delta\theta_0 < \theta_B \tag{6.17}$$

Using equation (6.17) in (6.16), the maximal bandwidth for a modulator is obtained

$$\Delta f_{\max} < \frac{1}{2} f \tag{6.18}$$

where it is assumed that $\sin\theta_B \approx \theta_B$ and $\cos\theta_B \approx 1$. Thus it follows that the largest modulation bandwidth is half of the working frequency and hence for larger bandwidth, f must be large.

The restrictions described in equation (6.17) and (6.18), in which the lower and upper limit of acoustic frequency are concerned, are not that important here, because it can be demonstrated that the incident and diffracted beams are still recognized even at the smaller frequency 500MHz, and the highest frequency which can be operated here is 2GHz, which arises from the limit of the numerical method used for SAW.

In order to demonstrate the effect of parameters, acoustic frequency f, acoustic power P_a, ridge width a and AO interaction length L, since it will become too complicated if dealing with them at the same time, two means are proposed in the following discussion. Firstly, the contour plot of beam diffraction efficiency is again use to select the optimal combination of f and P_a. Secondly, the figure of Merit Q is introduced in the analysis instead of f and L with $Q = \frac{2\pi\lambda_0 L}{n\Lambda^2}$. The reason for doing this is not just reducing the number of variables but also making it easy keeping $Q > 2\pi$ at any time.

Therefore it is shown in figure 6.16 the contour plot of beam diffraction efficiency in the acoustic power range from 0.1mW to 1.5mW. A larger power is of course available but choosing this small range of power that very limited peaks of diffraction efficiencies appear in the contour plots and a clear demonstration is easy to be made. From the figure it is noticed that the maximal efficiencies always appear with the largest power, therefore the diffraction efficiency at the power of 1.5mW as a function of acoustic frequency along with the modulation bandwidth is shown in figure 6.16. The upper and lower x-axis values has the same meaning since Q is fixed and $\frac{L}{\Lambda} \propto \frac{1}{f}$. A largest bandwidth of 383MHz is obtained at the smallest frequency as indicated in equation (6.16).

Similar groups of contour plot and bandwidth are shown in figure 6.17 and 6.18 with parameters, $Q = 5\pi$, $a = 2\mu$m, and $Q = 5\pi$, $a = 0.5\mu$m, respectively. It is

found that the maximal beam diffraction efficiency is achieved with $Q = 5\pi$ and $a = 0.5\mu$m, but the bandwidth has a larger value at $a = 2\mu$m since it has nothing to do with Q.

In conclusion, a smaller figure of merit Q and ridge width a will benefit beam diffraction efficiency, but larger ridge width a is good for larger bandwidth. For a specific Q and a, the trade-off between the efficiency and bandwidth about choosing a proper frequency (AO interaction length) emerges. For example, given $Q = 5\pi$ and $a = 2\mu$m, figure 6.17 shows that it is suggested either choose the interaction length of $L = 130\Lambda$ (1.1mm) and a working frequency 600MHz with a bandwidth of 379MHz and diffraction efficiency of 78% achieved, or choose $L = 74\Lambda$ (360μm) and a frequency 1GHz with a bandwidth of 359MHz and diffraction efficiency of 84% achieved.

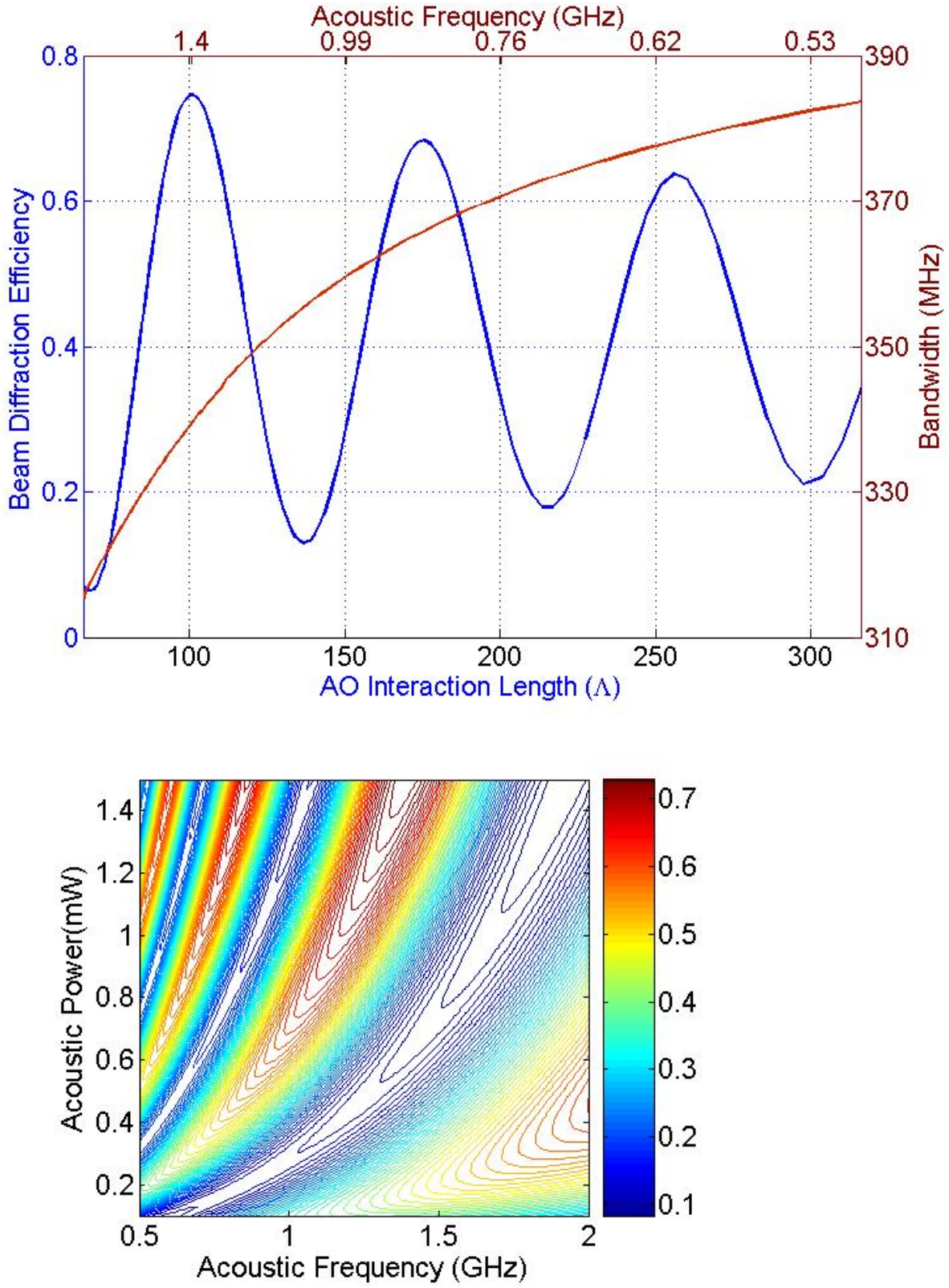

Figure 6.16: Beam diffraction efficiency and bandwidth with varying AO interaction length (acoustic frequency) and $Q = 10\pi$ and $a = 2\mu$m. The diffraction efficiency is demonstrated by acoustic driven power of: Solid, 0.22mW; dashed, 0.64mW; dotted. 1.3mW. Blue, left axis; red, right axis.

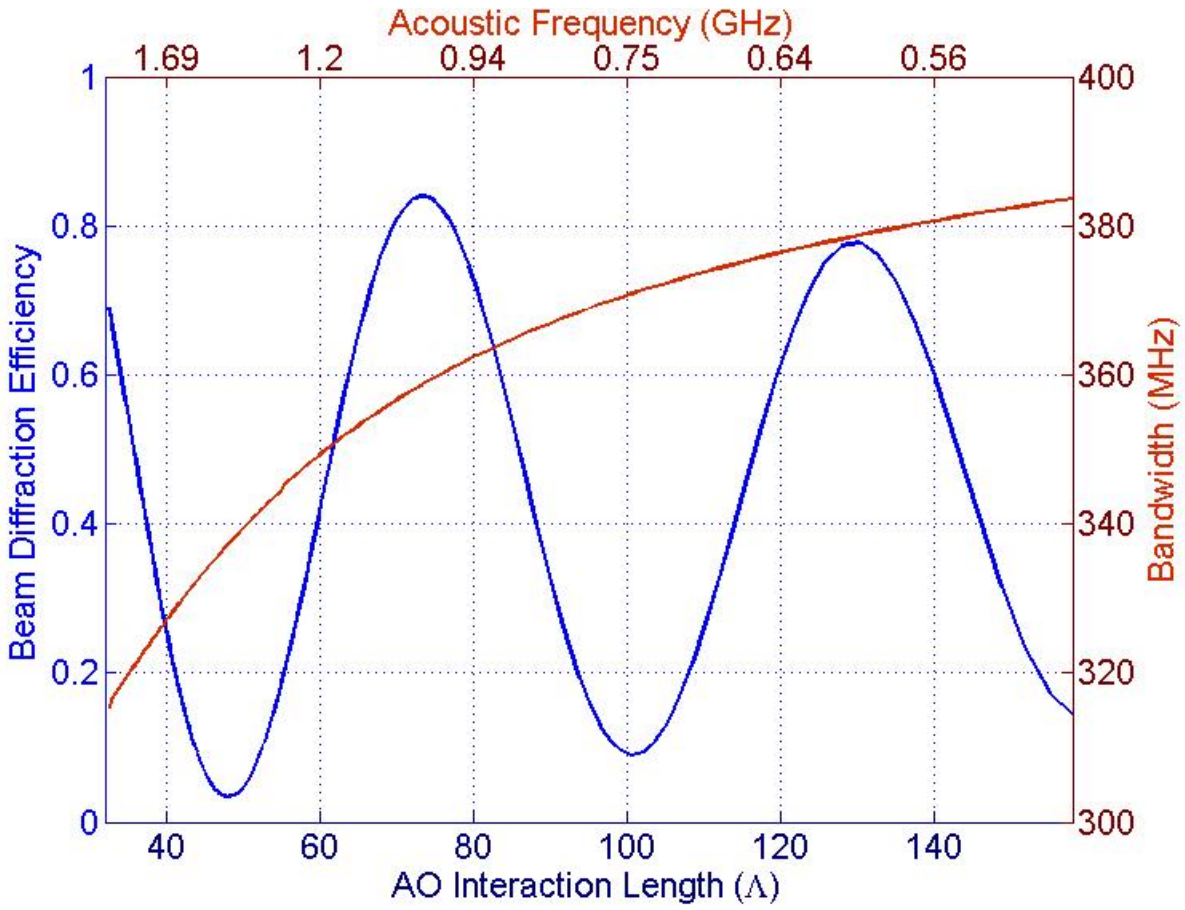

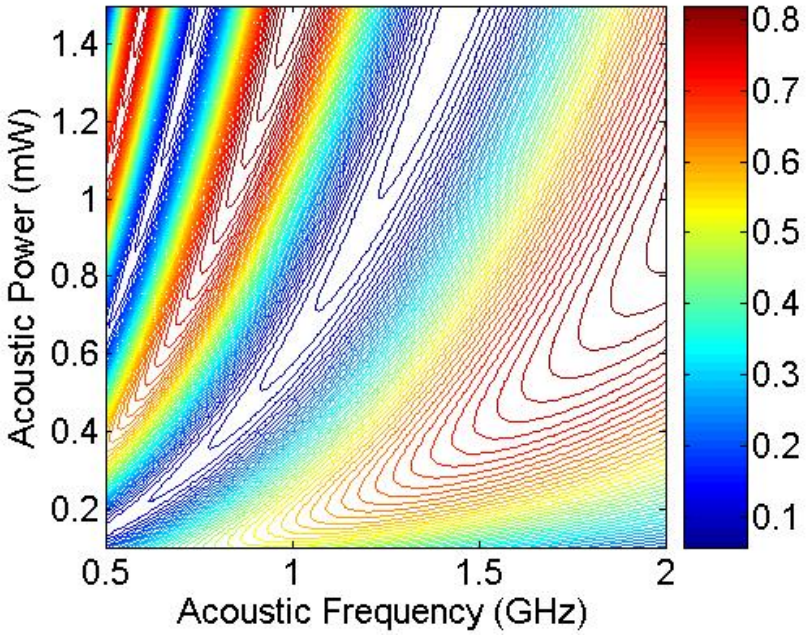

Figure 6.17: Beam diffraction efficiency and bandwidth with varying AO interaction length (acoustic frequency) and $Q = 5\pi$ and $a = 2\mu$m. The diffraction efficiency is demonstrated by acoustic driven power of: Solid, 0.42mW; dashed, 1.3mW. Blue, left axis; red, right axis.

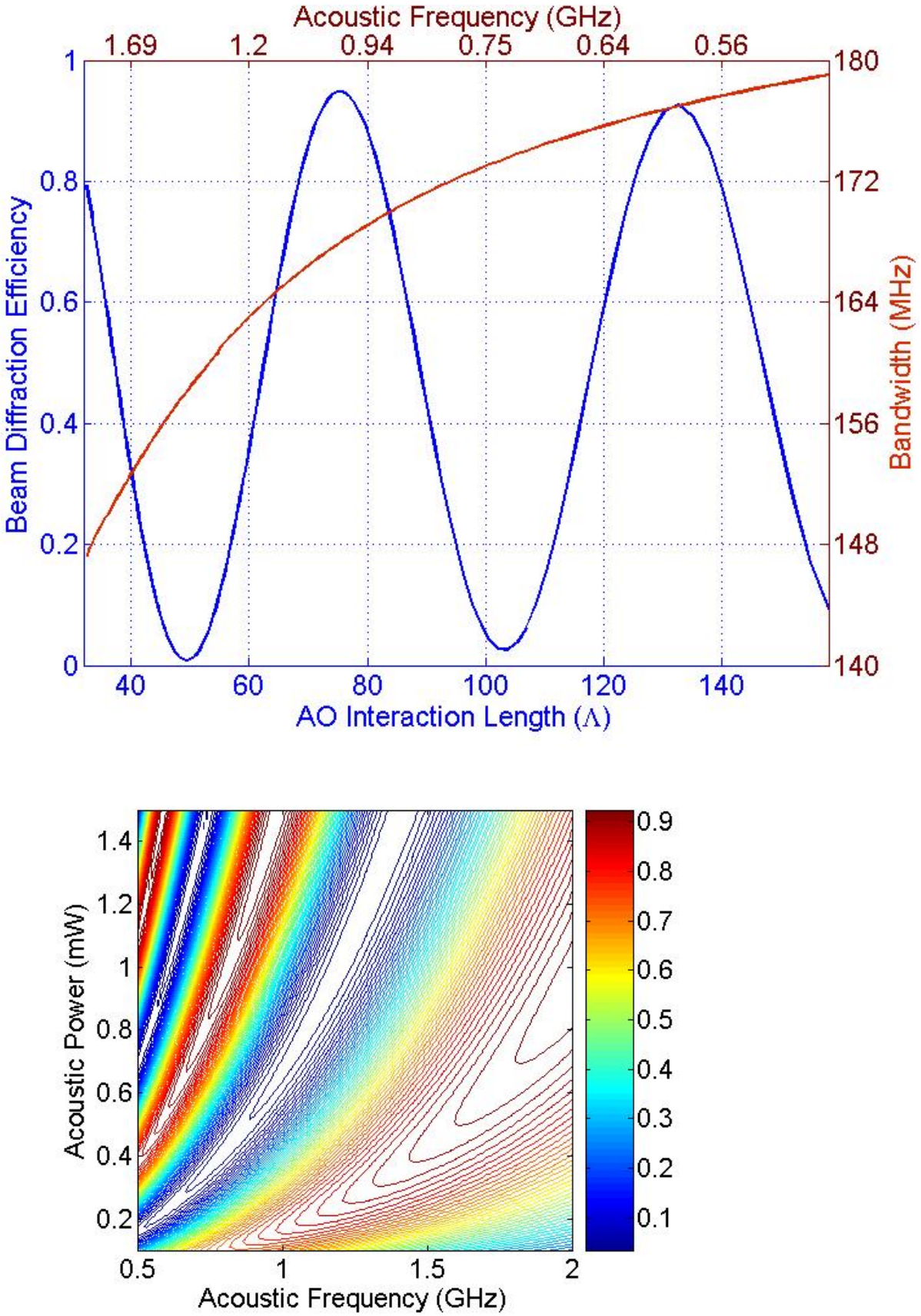

Figure 6.18: Beam diffraction efficiency and bandwidth with varying AO interaction length (acoustic frequency) and $Q = 5\pi$ and $a = 0.5\mu$m. The diffraction efficiency is demonstrated by acoustic driven power of: Solid, 0.42mW; dashed, 1.4mW. left axis; red, right axis.

6.7 Some Practical Consideration of FISOS

In the representation of the design of a FISOS, several useful assumptions have been made, such as the Bragg condition is precisely satisfied by optical and acoustic modes, and the optical source used is coherent. The section will give some evaluation in situations that those assumptions are not satisfied.

6.7.1 Misalignment

As long as the device is fabricated, an integrated modulator or deflector, any distortion of the position or dimension of planar elements on the surface, such as the ridge waveguide and the IDT, will give rise to the deviation of satisfying the Bragg condition. Simplifying the case by supposing there is an angle deviation between the ridge and the IDT, i.e., the elements are not well aligned, the resultant performance reduction is to be demonstrated here.

Considering an integrated SAW-controlled modulator, from the discussion in the previous section, the parameters are chosen: figure of merit $Q = 5\pi$, ridge width $a = 2\mu$m, designed working frequency $f = 1$GHz, IDT length $L = 360\mu$m, such that a desired incident Bragg angle of $\theta_i = \theta_B = 0.97°$, a modulation bandwidth 359MHz is achieved and the beam diffraction efficiency of 84% is obtained with the operating acoustic power $P_a = 1.1$mW given. Suppose the misalignment angle is $+0.2°$, the consequent frequency deviation is given

$$\Delta f = \frac{\lambda_0}{2nv_R}\Delta\theta_i \tag{6.19}$$

in which the definition of Bragg angle $\theta_B = \frac{\lambda_0 f}{2nv_R}$ is used and the acoustic velocity dispersion is neglected. The angular distribution of the desired profile (solid curve) and the one after misalignment (dashed curve) is shown in figure 6.19. It is noticed that due to the slight distortion of the spectrum, the overall diffraction efficiency is reduced from 84% to 80%. Thus a suggested modification of the working frequency is given by equation (6.19) that $f' = f - \Delta f$ with $\Delta f = 180$MHz and the diffraction efficiency can be restored (back to 84%).

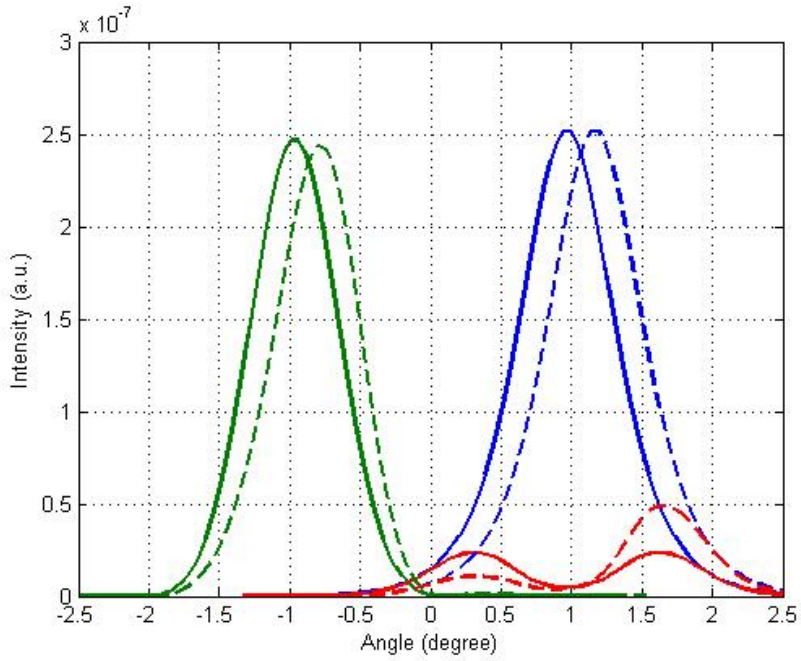

Figure 6.19: Angular spectrum of the Bragg diffraction in the proposed device. Solid, desired design; dashed, device with misalignment. Blue, incident optical mode; Green, diffracted; red, undiffracted.

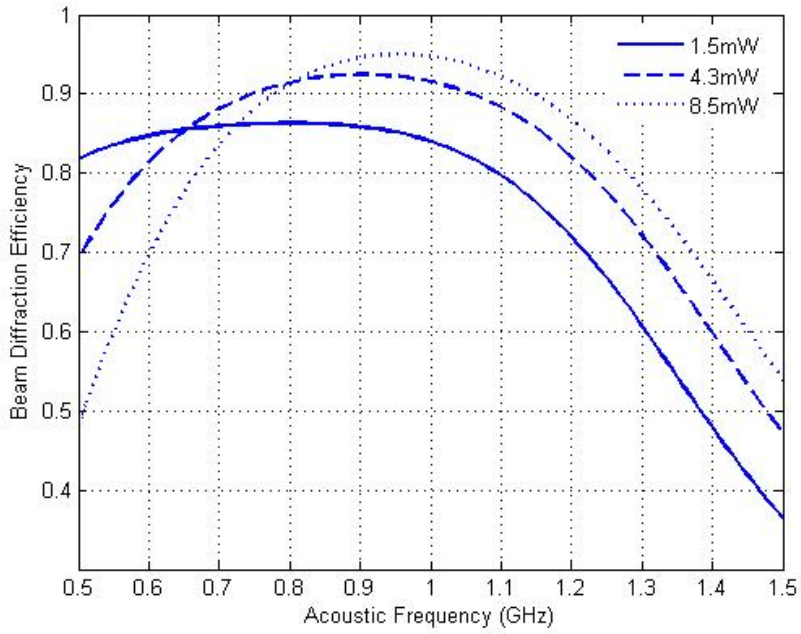

Figure 6.20: Beam diffraction efficiency varying with frequency in the device with misalignment driven by different acoustic power.

In fact, the practical performance of diffraction efficiency for such a modulator with misalignment can be simulated, as shown in figure 6.20, driven by different

acoustic powers, which are chosen to achieve a locally high efficiency. Particularly, it is noted that the flatter efficiency curve with smaller acoustic power gives the device more tolerance in misalignment, and this feature arises from the divergence of the optical beam and the modified expression of efficiency.

6.7.2 Incoherent optical source

Either GaN laser or LED could be fitted in the FISOS. The natural lack of one mirror for the integrated optical source indicates that using LED might be an easy option for the system. Supposing the source is totally incoherent and just taking an example for the purpose of demonstration, a Electroluminescent spectra with FWHM≈ 120nm in [117], of which the profile is simply approximated by a Gaussian function, is treated as the output of the GaN LED, i.e. the input for the acoustic Bragg grating. The beam diffraction efficiency is thus shown in fig 6.21 of both devices with coherent (blue) and incoherent optical source (red). The parameters for the proposed configuration is ridge width $a = 2\mu$m, acoustic frequency $f = 2$GHz, acoustic power $P_a = 1.1$mW and IDT length $L = 100\mu$m.

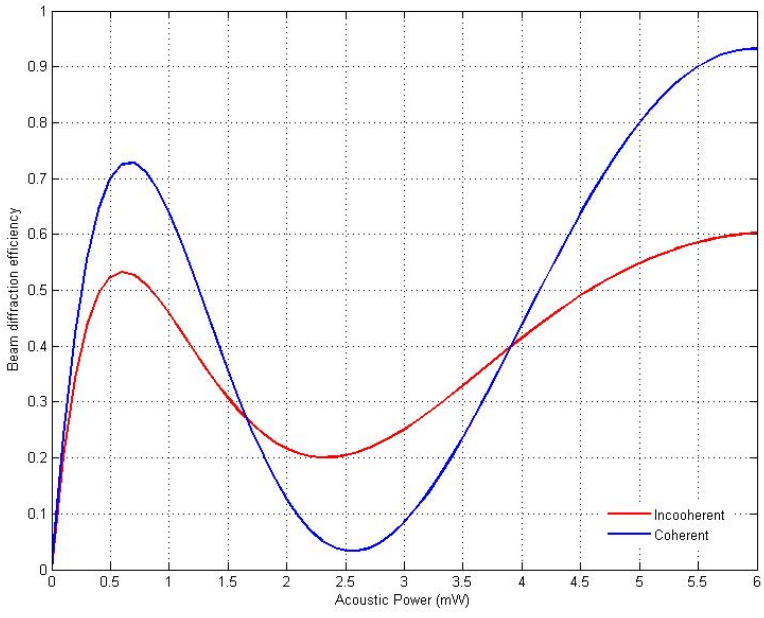

Figure 6.21: Beam diffraction efficiency as a function of loaded acoustic power. Blue, device with coherent source; red, incoherent source.

It is noted that in figure 6.21, though the variation of the beam diffraction efficiency with acoustic power is still in sin form, the scale between the peak and

valley is smaller, that is, the modulation capability of the acoustic power to the efficiency is getting weaker when the integrated optical source is incoherent. The consequence of partly coherence is expected to be between the two extreme cases of coherence and incoherence. The distortation of the curve is contributed to the Bragg diffractions of the components all through the spectrum.

6.8 Summary

The design consideration for a integrated functional optical source using GaN multilayer on sapphire structure is presented in this chapter. The angular distribution profile and spatial profile of AO interaction with guided optical and acoustic mode involved are demonstrated. An improvement to the expression of the diffraction efficiency, equation (6.5) is proposed and used for evaluations of the performance of FISOS. The so-called beam diffraction efficiency will give a more complete description of the AO effect when optical incidence with large divergence is included.

The analysis of the efficiency-resolution trade-off in a integrated deflector design is described. Short interaction length, high acoustic frequency and narrow ridge are proved to be helpful for a larger number of resolvable spots with a fairly high efficiency.

The design of the integrated modulator is also considered. Given the figure of merit Q is fixed, it is demonstrated that smaller Q, longer interaction length, larger ridge width and lower acoustic frequency will give rise to a larger bandwidth, though the highest efficiency might appear at a higher frequency.

The contour plot of the beam efficiency varying with acoustic frequency and power is proved to be convenient and powerful in the device design.

Some practical issues such as the misalignment of planar elements on the device and the incoherence of the integrated optical source are discussed. A modified working frequency can be used to compensate the efficiency loss in the former case; in the latter case, it is demonstrated that the nature of coherence of the optical source is not important from the viewpoint of diffraction efficiency.

Chapter 7

Conclusion and Future Work

The idea of monolithic integration of a semiconductor optical source and an acoustooptic functional processor is proposed in this report. This novel functional integrated semiconductor optical source (FISOS), compared with the conventional passive AO devices, is expected to achieve a reduction in insertion loss, an expansion of function and a simplification of assembly and packaging.

Numerical modeling has been used to investigate the characteristic features in the electrical properties of the IDT, the distribution and dispersion of the SAW in a multilayer structure and the guided-wave involved acoustooptic interaction. Due to the fact that in this monolithic integrated device gives rise to a large lateral divergence of the light emitted by the optical source, plane wave decomposition is used to analyze the incident light in the interaction with a SAW. Moreover, as a key parameter of an acoustooptic processor, the expression of the diffraction efficiency is improved to provide an appropriate description for the capability of SAW altering the characteristics of the optical beam with a large divergence.

A prototype of a FISOS is demonstrated in Chapter 5 and 6 based on a GaN/AlGaN multilayer structure providing both a visible light ($\lambda_0 = 405$nm) radiation (by assistance of InGaN MQW) and a high speed SAW of wavelength ($\sim \mu$m) comparable with light (by use of IDT). An etch-down at the SAW region is performed to increase the overlap between the guide optical mode and SAW mode, and then the diffraction efficiency. The reasonable depth of etching is suggested to be 700nm in the associated multilayer structure. The interaction in the GaN/AlGaN epitaxial film between the optical guide mode and a SAW of GHz frequency is investigated in such a monolithic substrate. Using the formulation of beam diffraction efficiency,

an efficiency over 90% is achieved with a typical 100μm acoustooptic interaction length by a driven rf power of a couple of mW. Taking a deflector and a modulator as example, the characteristic performance of FISOS is also reported. Given a small interaction length $L = 28.4\mu$m, although the efficiency is found to be over 96%, the number of resolvable spots achieved is 13 for 2μm of ridge width and 27 for 0.5μm of ridge width, which is quite small compared with data of the literatures using other material of separated device, [118]. This is because the divergence of the optical beam is much larger than one in free space after collimation used in separated AO device. In the case of integrated modulator, the simulation indicates that smaller magnitude of Q and larger ridge width a give rise to a larger modulation bandwidth. Given $Q = 5\pi$ (i.e. $L = 1.7$mm), $a = 2\mu$m, the bandwidth is up to 372MHz at a 500MHz working frequency with the price of diffraction efficiency falling to 60% from its peak value of 80% when a driven power of 1.4mW is used. This result is comparable with conventional AO modulators in the literature [120]but the required driving power is smaller. Although it has demonstrated the advantages and feasibility of the FISOS, there is still a lot of work to do to improve and enhance this design. First of all, the modeling, although from the generation of SAW to the interaction of guided waves are inclusive, is far from complete. The evaluation of injected current density, the optical gain and absorption and the electroluminescent spectra of the source, the absorption of the SAW to prevent its reflection at edges of wafer [82], the photo detector as one essential part of a monolithic OIC, the thermal effect of the whole device [121][122], the impedance matching for rf input [57] and the device packaging, are not considered yet. These elements are quite essential for a mature device design and must be considered in the future.

For the purpose of simplifying the analysis, a variety of assumptions have been made. For example, though the acoustic loss while SAW propagating and the optical loss in the unpumped region have been mentioned, they are not included in the modeling. The performance fall-off in the acoustic path when the optical beam is very wide should be estimated [123]. Techniques preventing the strong optical absorption in the unpumped region (SAW region) must be considered, such as QW intermixing to alter the band gap of the unpumped region, or extending the metal contact to the SAW region for a current pump throughout the device. Besides, a coherent optical source is assumed in the simulation of the acoustooptic diffraction, but it is not the case in a practical laser, particularly not for the LED. However,

the incoherent optical source is considered at the end of the previous chapter and no significant influence to the diffraction efficiency is found.

Another important simplification is that the material is assumed to be isotropic in the analysis of acoustooptic interaction. This is true for GaN film since the physical properties on the (001) plane is isotropic. In fact, for most of AO materials, such as $LiNbO_3$, GaAs and TeO_2, anisotropic acoustooptic interaction takes place between ordinary and extraordinary optical beams. The momentum reservation relationship in a birefringent crystal is shown in fig 7.1. It can be seen that a change in the direction of the diffracted wave vector $\boldsymbol{k}_d$ to $\boldsymbol{k}'_d$ can be obtained by a change in the magnitude of the acoustic wave vector $\boldsymbol{K}$ to $\boldsymbol{K}'$. Thus an optical beam can be deflected simply by varying the frequency of a well-collimated acoustic beam which remains fixed in direction. This implies that the angular spread of the acoustic wave vector required for phase matching across a particular acoustic bandwidth needs to be much less for the anisotropic than for the isotropic interaction. This represents an advantage of the anisotropic interaction over the isotropic, because it allows the design of AO devices with much wider bandwidth (for fixed diffraction efficiency) or with higher diffraction efficiency (for fixed bandwidth). Therefore, in order to take advantage of the anisotropic AO interaction, for example, tunable filters used in WDM (wavelength division multiplexing) network [124], or an anisotropic material GaAs might be a proper choice for the FISOS device, [125].

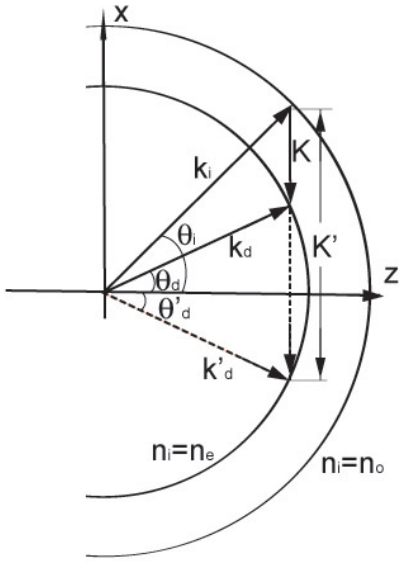

Figure 7.1: Wave vector diagram for the general case of anisotropic diffraction.

The modeling proposed in the report is supposed to give estimations in some

aspects that are not considered yet. For example, pure Bragg regime ($Q > 2\pi$) is just one extreme case that is used in the simulation of FISOS. Since sometimes the magnitude of Q is expected to be small (for example, a modulator) for a wider bandwidth, the analysis in the intermediary region $1 < Q < 2\pi$ might be necessary due to the possibility of the appearance of higher order diffraction. The efficiency and bandwidth might be decreased again [126] when the value of Q is lower than some threshold. The proposed rigorous grating diffraction theory is expected to be employed for a simulation in such case. Moreover, the acoustic wave is considered to be a plane wave in the diffraction calculation, but in fact, the distortion of the acoustic wave is suggested to be considered when its length L is decreased for a wider bandwidth. Therefore the PW decomposition of the acoustic wave can be proceeded to determine its power distribution. Therefore an optimal direction and position of the acoustic and optical beam relative to the crystal axes can be found, [113].

In addition, the transfer matrix used to simulate the mode solution of SAW propagating in a multilayer structure has been found to be unstable when the frequency is higher than 2GHz. Alternatively, the scattering matrix, reported by Zhang in 2008 [127], was proved to be able to give more stable solutions particularly when the layer is quite thick relative to the SAW wavelength or frequencies are very high.

From the viewpoint of monolithic integration, some mature technique in separated AO device can be used as well in FISOS. For example, beam-steering transducers can be used to obtain efficient deflectors with large bandwidth, [128]. The IDTs are connected parallel to steer the acoustic beam as a function of frequency in such a manner that the optical beam and the acoustic wave remain phase matched at the Bragg angle over large frequency changes.

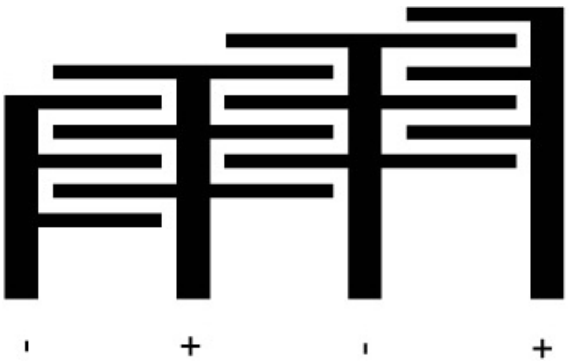

Figure 7.2: Series-parallel connected transducers.

In conclusion, the key modeling and the feasibility of the FISOS device have been demonstrated in this report, whilst there are still lots of work to do before it goes to practicality.

References

[1] S.E. Miller, Integrated optics: an introduction, Bell System Technical J., 48, 2059, 1969

[2] K.Yoshida, Y.Kurui, S. Sentsui, T. Kuroha, Low-loss fibre prepared under high deposition rate by modified c.v.d. technique, Electron. Lett.,13(20), 608, 1977

[3] J.E.U. Ashton, R.M. Gibb and B.A. Eales, Semiconductor cw laser packages with full hermeticity integral power monitoring and direct fibre optic launching, Optics Laser Tech., 12(5), 261, 1980

[4] E.J. Murphy, J.Ocenasek, C.R.Sandahl, R.J.Lisco, Y.C.Chen, Simultaneous single-fibre transmission of video and bidirectional voice/data using LiNbO3 guided-wave devices, J. Lightwave Tech., 6(6), 937, 1988

[5] J.A. Chiddix, The integration of optical fiber into today's cable television networks, Broadband Analog Optoelectronics: Devices and Systems, 1990. Conference Digest., 39, 1990

[6] R. Yamauchi, Specialty fibers, Lasers and Electro-Optics Society Annual Meeting, LEOS '94 Conference Proceedings IEEE, Volume 2, 228, 1994

[7] R.C.Alferness, Multiwavelength optical network activities in the US, Optical Communication, ECOC '96, 22nd European Conference on, Volume 2, 35, 1996

[8] C.D. Chen, I. Kim, O. Mizuhara, T.V.Nguyen, K. Ogawa, R.E.Tench, L.D.Tzeng, P.D.Yeates, 40 Gbit/s25 ch (1 Tbit/s aggregate capacity) WDM transmission over 342 km of fibre, Electronics Letters, 35(8), 648, 1999

[9] F.Tian, Ch.Harizi, H.Herrmann, V.Reimann, R.Ricken, U.Rust, W.Sohler, f.Wehrmann and S.Westenhofer, Polarization-Independent Integrated optical, acoustically tunable double-stage wavelength filter in LiNbO3, J. Lightwave Tech., 12(7), 1192, 1994

[10] D.A.Smith, R.S.Chakravarty, Z.Bao and A.E.Willner, Evolution of the acousto-optic wavelength routing switch, J. Lightwave Tech., 14(6), 1996

[11] K.Schafer, I. Baumann, W.Sohler, H.Suche and S.Westenhofer, Diode-pumped and package acoustooptically tunable Ti:Er:LiNbO3 waveguide lader of wide tuning range, IEEE J. Quantum Electron., 33(10), 1997

[12] P.V.Santos, Collinear light modulation by surface acoustic waves in laterally structured semiconductors, J. Appl. Phys., 89(9), 5060, 2001

[13] A.Kar-Roy and C.S.Tsai, New integrated acousto-optic matrix algebra processor architecture, Appl. Phys. Lett., 59(24), 3093, 1991

[14] S.Krishnamurthy and P.V.Santos, High-contrast optical modulation by surface acoustic waves, Appl. Phys. Lett., 83(13), 2548, 2003

[15] L. Brillouin, diffusion de la lumiere et des rayons X par un corps transparent homogene, influence de l'agitation thermique, Ann. Phys. 17, 88, 1922

[16] R.Lucas, P. Biquard, Proprietes optiques des milieux solides et liquids soumis aux vibrations elastiques elastiques ultrasonores, J. Physique, 10, 464, 1932

[17] P.Debye, F.W.Sears, On the scattering of light by supersonic waves, Proc. Nat. Acad. Sci., 18, 409, 1932

[18] C.V.Raman, N.S.N.Nath, The diffraction of light by high frequency sound: part I, Proc. Indian Acad. Sci., 2, 406; Part II, 2, 413, 1936; Part III, 3, 75, 1936; Part IV, 3, 119, 1936; Part V, 3, 459, 1936; Generalised theory, 4, 222, 1936

[19] R. Adler, Interaction betweeen light and sound, IEEE spectrum 4, 42, 1967

[20] H. Szmacinski, J.R. Lakowicz, Fluorescence lifetime-based scensing and imaging, Sensors and Actuators B, 29, 16, 1995

[21] C.S.Tsai, guided wave acoustooptic bragg modulators for wideband integrated optic communications and signal processing, IEEE Trans. Circuits Syst., CAS-26, 1072, 1979

[22] E.H. Younf, S. Yao, Design considerations for acousto-optic devices, Proceedings of the IEEE, 69, 54, 1981

[23] J. remenyi, P. Maak, I. Frigyes, L. Jakab and P. Richter, Demonstration of continuously variable true-time delay in frequency dependent phase compensating system with acousto-optics and liquid crystal modulator, Optics commu., 226, 211

[24] S. Zohar, spectral window of the acousto-optic folded spectrum analyzer, Appl. Opt., 32, 6445, 1993

[25] S.Veeriah, F.A.Rahman and V.Mishra, Multiple parameter tuning of the bandwidth, wavelength and attenuation of a fiber-based acoustooptic tunable filter, Optik-International Journal for light and electron optics, 2006

[26] H.Matsumoto and Akiko Hirai, A white-light interferometer using a lamp source and heterodyne detection with acousto-optic modulators, Optics Commu., 170, 217, 1999

[27] W.R.Klein and B.D.Cook, Unified Approach to Ultrasonic Light Diffraction, IEEE Trans. Sonics Ultrason. SU-14, 123, 1967

[28] W.G.Mayer, gBLamers, and D.C.Auth, J. Acoust. Soc. Am., 42, 1255, 1967

[29] G.I.Stegeman, IEEE Trans. Sonic. Ultrason., SU-23, 33, 1976

[30] S.Petroni, G.Tripoli, C.Combi and A.Passaseo, Noise reduction in GaN-based radio frequency surface acoustic wave filters, Appl. Phys. Lett., 85 (6), 1039, 2004

[31] V.V. Nikulin, M. Bouzoubaa, V.A. Skormin, T.E. Busch, Modeling of an acousto-optic laser beam steering system intended for satellite communication, Optical engineering, 40(10), 2001

[32] E.I. Gordon, Figure of merit for acousto-optical deflection and modulation devices, J. Quan. Elec., QE-2, 104, 1966

[33] S.K.Yao and E.H. Young, SPIE, 90, 23, 1976

[34] D.Mergerian, Appl. Opt., 19, 3033, 1980

[35] W. Xu, X. Zhang, H. Yu, A. Abbaspour-Tamijani, J Chae, In-Liquid Quality Factor Improvement for Film Bulk Acoustic Resonators by Integration of Microfluidic Channels, IEEE Electron Device Letters, 30, 647, 2009

[36] A. Chatterjee, P.K.Das and L.B.Milstein, The use of SAW convolvers in spread-spectrum and other signal proceesing applications, IEEE Trans. on Sonics and Ultrasonics, SU-32, 745, 1985

[37] C.Qiu, Z.Liu, J.Mei, J. Shi, Mode-selecting acoustic filter by using resonant tunneling of two-dimensional double phononic crystals, Appl. Phys. Lett., 87(10), 104101, 2005

[38] C.K.Campbell, Y.Ye and J.J.Sferrazza Papa, Wide-band linear phase SAW filter design using slanted transducer fingers, IEEE Transactions on Sonics and Ultrasonics, SU-29, 224, 1982

[39] R.M.White and F.W.Voltmer, Direct piezoelectric coupling to surface elastic waves, Appl. Phys. Lett., 7, 314, 1965

[40] J.F. Nye, Physical properties of crystals, Clarendon, Oxford, 1960

[41] Lord Rayleigh, On waves propagated along the plane surface of an elastic solid, Proc. London Math. Soc. 17, 4, 1885

[42] Y.Takagaki, P.V.Santos, Guided propagation of surface acoustic waves in AlN and GaN films grown on 4H-SiC(0001) substrates, Phys. Rev. B, 66, 155439,2002

[43] A.H. Fahmy and E.L. Adler, Propagation of acoustic surface waves in multilayers: A matrix description, Appl. Phys. Lett., 22, 495, 1973

[44] S.W. Director and R.A.Rohrer, Introduction to system theory, New York: McGraw-Hill, 205-256, 1972

[45] T.M.Reeer, D.K.Winslow, 'Characteristics of microwave acoustic transducers for volume wave excitation', Microwave Theory Tech., IEEE Trans., MTT-17, 927-941, 1969

[46] R.M.White, Surface elastic waves, Proc. IEEE 58, 1238, 1970

[47] D.P.Morgan, Key papers on Surface Acoustic Wave Passive Interdigital Devices, IEE, Reprint Series 2, Peter Peregrinus, Stevenage, 1976

[48] K.Yamanouchi, T.Meguro, Z.H.Chen and K.Matsumoto, 'New surface acoustic wave interdigital transducers with narrow electrod gaps', Ultrasonics Symp., IEEE Proceedings, 63-66, 1988

[49] O. Manner, R. Ganss-Puchstein, 'Accurate computation of apodized SAW transducer capacitances', Ultrasonics Symp, IEEE proceedings, 23-28, 1988

[50] Y. Satoh, K. Yamanouchi, SAW unidirectional interdigital transducer with ultra-low insertion loss and wide band in 10MHZ-10GHZ range, Digital Object Identifier 10.1109/FREQ.1573997,2005

[51] B.A.Auld and G.S.Kino, IEEE Trans. Electron. Devices, ED-18, 898, 1871

[52] D. Royer, E. Dieulesaint, Translater: David P. Morgan, Elastic waves in solid II, Springer, 76, 1996

[53] S.Datta, B.J.Hunsinger, and D.C.Malocha, IEEE Trans. Son. Untrason., SU-26, 235, 1979

[54] C.Deger, E.Born, H. Angerer and G.Fischerauer, Sound velocity of AlGaN thin films obtained by surface acoustic-wave measurements, Appl. Phys. Lett., 72(19), 1998

[55] T.K.Gaylord and M.G.Moharam, Analysis and application of optical diffraction by gratings, IEEE Proc. 73(5), 1985

[56] G.L.Mattaei, L.Young, and E.M.T.Jones, Microwave Filters, Impedance-Matching Networks, and Coupling Structures. New York: McGraw-Hill, 1964

[57] E.H.YOung and S. Yao, Design considerations for acousto-optic devices, Proc. IEEE, 69(1), 1981

[58] A.A.Cottey, Floquet's theorem and band theory in one dimension, American J. Phys., 39, 1235, 1971

[59] J.A.Kong, Second-order Soupled-mode Equations for Spatially Periodic Media, J. Opt. Soc. Amer., 67, 1165-1170, 1977

[60] N.S.N.Nath, The diffraction of light by supersonic waves, Proc. Ind. Acad. Sci. A, 8, 499, 1938

[61] P. Phariseau, On the diffraction of light by progressive supersonic waves, Proc. Ind. Acad. sci. A, 44, 165, 1956

[62] C.S.Tsai, Guided-Wave Acousto-Optics Interactions, Devices and Applications, Springer-Verlag, 1990

[63] L.Kuhn, M.L.Dakss, P.F.Heidrich, and B.A.Scott, Deflection of an optical guided wave by a surface acoustic wave, Appl. Phys. Lett., 17, 265, 1970

[64] R.V.Schmidt, I.P.Kaminow and J.R.Carruthers, Acoustooptic diffraction of guided optical waves in LiNbO3, Appl. Phys. Lett., 23, 417, 1973

[65] M.L.Shah, Fast acoustic diffraction-type optical waveguide modulator, Appl. Phys. Lett., 23, 556, 1973

[66] I.C.Chang, Acousto-optic devices and application, IEEE Trans. Sonics and Ultrasonics, SU-23, 2, 1976

[67] Eric G.H. Lean, James M.White, and Christopher D.W. Wilkinson, Thin-film Acoustooptic Devices, Proceddings IEEE, 64, 779, 1976

[68] R.W.Dixon, IEEE J. Quantum Electron. QE-3, 85, 1967

[69] K. Schafer, I.Baumann, W.Sohler, H.Suche and S.Westenhofer, Diode-Pumped and packaged acoustooptically tunable Ti:Er:LiNbO3 waveguide laser of wide tuning range, IEEE J. Quan.Electron. 33(10), 1636, 1997

[70] K. Yoshino, Y. Shimoda, Y. Kawagishi, K. Nakayama, M. Ozaki, Temperature tuning of the stop band in transmission spectra of liquid-crystal infiltrated synthetic opal as tunable photonic crystal, Appl. Phys. Lett. 75, 932 (1999)

[71] , Z. Liu, Y. Huang, B. W. Wessels, Performance simulation for ferroelectric thin-film based waveguide electro-optic modulators, Optics Communications, 255, 319 (2005)

[72] P. Halevi, F. Ramos-Mendieta, Tunable Photonic Crystals with Semiconducting Constituents, Phys. Rev. Lett. 85, 1875 (2000)

[73] S.Krishnamurthy and P.V.Santos, Optical modulation in photonic band gap structures by surface acoustic waves, J. Appl. Phys., 96(4), 1803, 2004

[74] T.Tamir, H.L.Bertoni, Unified theory of optical beam couplers, Digest of Technical Papers, Topical meeting on Integrated Optics, MB3-1, 1972

[75] S.T.Peng, T.Tamir and H.L.Bertoni, analysis of thick-grating beam couplers, digest of technical papers, Topical meeting on Integrated Optics, TuB8-4, 1974

[76] N. Uchida and N. Niizeki, Acoustooptic deflection materials and techniques, Proc. IEEE, 61, 1073, 1973

[77] R.W.Dixon, Photoelastic properties of selected materials and their relevance for applications to acoustic light modulators and scanners, J. Appl. Phys., 38, 5149, 1967

[78] C. P. Wen and R. F. Mayo, Acoustic attenuation of a single domain lithium niobate crystal at microwave frequencies, J. Electron. Mater., 9, 135, 1966

[79] R. Madabhushi, Wide-band Ti:LiNbO3 optical modulator with low driving voltage,Optical Fiber Communication Conf., Vol. 2 of 1996 OSA Technical Digest Series, 1996

[80] P.R.Pedersen, J.L.Nightingale, B.E. Kincaid, J.S. Vrhel, R.A. Becker, A high-speed 44 Ti:LiNbO3 integrated optic switch at 1.5um, J. Lightwave Tech., 8(4), 618, 1990

[81] J. Wang, J. Shi, Z. Zhou, and X. Chen, Tunable multi-wavelength filter in periodically poled LiNbO3 by a local-temperature-control technique, Opt. Express 15, 1561, 2007

[82] N. Uchida and Y. Ohmachi, Elastic and photoelastic properties of TeOz single crystal, J. Appl. Phys., 40, 4692, 1969

[83] N. Uchida, Acoustic attenuation in TeO2, J. Appl. Phys., 43, 2915, 1972

[84] X.Gong and D. Zhang, A novel temperature stable composite substrates for surface acoustic wave applications, Piezoelectricity, Acoustic Waves, and Device Applications, 2008. SPAWDA 2008. Symposium on, 550, 2008

[85] V.V.Proklov, S.N. Antonov, M.Y. Mesh, High-stability acousto-optical devices using bulk acoustic waves in TeO2, Electron. Lett., 14, 535, 1978

[86] Takahashi, M. Hideo, M. Chihiro, Koh-Ichi, A New Automatic Measuring Method for Optical Fibers Using an Acoustooptic Tunable Filter, Instrumentation and Measurement, IEEE Transactions on, 29(4),348, 1980

[87] R.J. Sadler, M.R. Buttinger, Acousto-optic ambiguity function processor, Optoelectronics, IEE Proceedings J., 133, 85, 1986

[88] B.Beche, H.Porte, J. Goedgebuer, and C. Fontaine, A Tunable filter with collinear acoustooptical TE-TM mode conversion in a GaAs-AlAs multiquantum-well waveguide, IEEE J. Quant. Elec., QE-35, 820, 1999

[89] D.Ciplys, R.Rimeika, M.S.Shur, S.Rumyantsev, R.Gaska, A.Sereika, J.Yang and M. Asif Khan, Visible-blind photoresponse of GaN-based surface acoustic wave oscillator, Appl. Phys. Lett., 80(11), 2020, 2002

[90] T.Palacios, F.Calle, J.Grajal, Remote collection and measurement of photogenerated carriers swept by surface acoustic wave in GaN, Appl. Phys. Lett., 84(16), 3166, 2004

[91] R.Rimeika, D.Ciplys, R.Gaska, J.W.Yang, M.A.Khan, M.S.Shur and E.Towe, Diffraction of guided optical waves by surface acoustic waves in GaN, Appl. Phys. Lett., 77(4), 480, 2000

[92] D.ciplys, R.Rimeika, M.S.Shur, R.Gaska, J.Deng, J.W.Yang and M.A.Khan, Acousto-optic diffraction of blue and red light in GaN, Appl. Phys. Lett., 80(10), 1701, 2002

[93] G.Bu, M.S.Shur, D.Ciplys, R.Rimeika, R.Gaska and Q.Fareed, Guided-wave acoustooptic diffraction in AlGaN epitaxial layers, Appl. Phys. Lett., 85(12), 2157, 2004

[94] C.S.Tsai, B.Sun and A.Kar-Roy, Guided-wave acoustooptic Bragg diffraction in indium gallium arsenide phosphide waveguides, Appl. Phys. Lett., 70(24), 3185, 1997

[95] J.I.Pankove, E.A. Miller, and J.E. Berkeyheiser, GaN electroluminescent diodes, RCA Rev. 32, 383, 1971

[96] H. Amano, M. Kito, K. Hiramatsu and I. Akasaki, P-Type Conduction in Mg-Doped GaN Treated with Low-Energy Electron Beam Irradiation (LEEBI), Jpn. J. Appl. Phys. Vol. 28, L2112, 1989

[97] S. Nakamura, M. Senoh, N. Iwasa, and S. Nagahama, Jpn. J. Appl. Phys. 34, L797 (1995).

[98] S.Nakamura, InGaN-based violet laser diodes, Semiconductor Sci. and Tech., 14, R27, 1999

[99] D. Bour, Nitride Lasers, conf. Lasers and Electoro-Optics, OSA, 7, 1999

[100] S.Nakamura, T.Yanamoto, M. Sano and T. Mukai, Jpn. J. Appl. Phys., 41, 5, 2002

[101] H.Yang, L.Chen, S.Zhang, Chin. J. Semiconduct., 26, 414, 2005

[102] A.Smith, J.E.Hastie, H.D.Foreman, T.Leinonen, M.Guina, M.D.Dawson, GaN diode-pumping of red semiconductor disk laser, Electro. Lett., 44(20), 1195, 2008

[103] J.Piprek, R.K.Sink, M.A. Hansen, J.E.Bwers, and S.P.DenBaars, Simulation and Optimization of 420 nm InGaN/GaN Laser Diode, Phys. Simmula. Opto-electro. Devices VIII, ed. R.Binder, P.Blood and M.Osinski, SPIE Proc. 3944, 2000

[104] M.Shiojiri, M.Ceh, S.Sturm, C.C.Chuo, J.T.Hsu, J.R.Yang, and H. Saijo, Structural and compositional analyses of a strained AlGaN/GaN superlattice, J. Appl. Phys., 100, 013110, 2006

[105] D.brunner, H. Angerer, E. Bustarret, f. Freudenberg, R.Hopler and R.Dimitrov, Optical constants of epitaxial AlGaN films and their temperature dependence, J. Appl. Phys, 82(10), 5090, 1997

[106] G.M.Laws, E.C.Larkins, I.Harrison, C.Molloy and D.Somerford, Improved refractive index formulas for the AlGaN and InGaN alloys, J. Appl. Phys., 89(2), 1108, 2001

[107] C.Y.Chan, K. Tsang, E.Herbert Li and P. Steven, Theermal annealing of InGaN/GaN Strained-layer quantum wall, Denbaars MRS Internet J. Nitride Semicond. Res. 4S1, G6.25, 1999

[108] I.Gontijo, T.Krauss, J.H.Marsh and R.M.De La Rue, Postgrowth control of GaAs/AlGaAs quantum well shapes by impurity-free vancancy diffusion, IEEE J.Quantum Electron., 30, 1189, 1994

[109] H. Lin, c.Wu, W. Chien, S. Chen, H. Kao, J. Chyi, J. Chen, Investigation of layered structure SAW devices fabricated using low temperature grown AlN thin film on GaN/Sapphire, IEEE Tran. Ultrasonics Ferroelec. Freq. Contr., 52(5), 923, 2005

[110] S. Lee, H. Jeong, S. Bae, H. Choi, J. Lee and Y. Lee, Epitaxially grown GaN thin-film SAW filter with high velocity and low insertion loss, IEEE Tran. Electron Device, 48(3), 524, 2001

[111] I.C.Chang, Characteristics of acousto-optic devices for signal processors, Opt. En. 21(1), 76, 1981

[112] L.N. Magdich, V.Y. Molchanov, J. Opt. Spectrosc. 70(1), 1980

[113] P.Maak, Improved design method for acousto-optic light deflectors, Opt. Comm., 172, 297, 1999

[114] W.S.C.Chang, Acoustooptic deflections in thin films, Quant. Elect. QE-7, 167, 1971

[115] E.G.Lean, Acousto-optic interaction in guided wave structures, Introduction to Integrated Optics, M.K.Barnoski, Ed. New York: Plenum Press, 441-470, 1974

[116] C.J.Lii, C.S.Tsai, and C.C.Lee, Wideband guided-wave acoustooptic Bragg cells in GaAs-GaAlAs waveguide, IEEE J. Quan. Electron., QE-22, 868, 1986

[117] S.N. Mohammad, Emerging Gallium Nitride Based Devices, Proceedings of the IEEE, vol. 83, No. 10, 1306, 1995

[118] J.B.Merry, High resolution acousto-optic deflector demonstrated in a laser scanner, CLEOS, 1978

[119] T.G.Gialorenzi, A.F.Milton, J.Appl. Phys, 24, 159, 1974

[120] Y.Omachi, J. Appl. Phys., 44, 3928, 1973

[121] G.Bu, D.Ciplys, M.Shur, L.J.Schowalter, S.Schujman and R.Gaska, Temperature coefficient of SAW frequency in single crystal bulk AlN, Electron. Lett., 39(9), 755, 2003

[122] P. Maak, T. Takacs, A.Barocsi, E.Kollar, V.Szekely and P.Richter, Refractive index nonuniformities in acousto-opitic devices due to heat production by ultrasound, Opt. Commu., 266, 419, 2006

[123] N.J.Berg, M. Dekker, Acousto-optic signal processing, New York, 1983

[124] J. Sapriel, D.Charissoux, V.Voloshinov and V.Molchanov, Tunable acoustooptic filters and equalizers for WDM application, J. Lightwave Tech., 20(5),864, 2002

[125] A. Kar-Roy, C.S.Tsai, Ultralow sidelobe-level integrated acoustooptic tunable filters using tapered-gap surface acoustic wave directional couplers, J. Lightwave Tech., 12(6), 1994

[126] C.C.Wang, C.W.Tarn, Theoretical and experimental analysis of the near-Brag acousto-optic effect, Opt. Eng., 37, 208, 1998

[127] V. Zhang and V. Laude, Unified and stable scattering matrix formalism for acoustic waves in piezoelectric stacks, J. Appl. Phys., 104, 064916,2008

[128] R.M. de la Rue, C. Stewart, C.D.W. Wilkinson, and I.R. Williamson, Frequency-controlled beam steering of surface acoustic waves using a stepped transducer array, Electron. Lett., 9, 326, 1973

[129] S.K.Chatterjee, Crystallography and the World of Symmetry, Springer-Verlag Berlin Heidelberg, 2008

[130] S.Datta, Surface Acoustic Wave Devices, Prentice-Hall, 1986

[131] C.A.balanis, Advanced Engineering Electromagnetics, John Wiley & Sons, 1989

[132] Pochi Yeh, Optical Waves in Layered Media, Wiley-Interscience, 1998

[133] H. Kogelnik and V. Ramaswamy, Appl. Opt., 8, 1857, 1974

[134] T.M.Smith and A.Korpel, Measurement of light-sound interaction efficiency in solids, IEEE J. Quanium Electron, QE-1, 283, 1965

Appendix A

Bulk acoustic waves in isotropic medium

Rewrite equation (2.23) below, the one derived from the dynamic motion equation (2.21) with a plane elastic wave considered

$$(c_{ijkl}s_j s_l - \rho\delta_{ik})U_k = 0 \tag{A.1}$$

The slowness $\boldsymbol{s}$ in fact can be written in the form

$$\boldsymbol{s} = \frac{\hat{s}}{v} \tag{A.2}$$

where $\hat{s}$ is the unit vector indicating the propagation direction of the elastic wave and v denotes the magnitude of the phase velocity of the elastic wave.

Substituting equation (A.2) into equation (A.1) yields

$$(c_{ijkl}\hat{s}_j\hat{s}_l - v^2\rho\delta_{ik})U_k = 0 \tag{A.3}$$

Consider a plane elastic wave propagating along x_1 in a infinitely large GaN material. The x_3-axis is supposed to parallel to the c-axis of GaN and the stiffness tensor c_{ijkl} is thus in the form as shown in equation (2.15). Given $\hat{s} = [1, 0, 0]$, the previous equation becomes

$$\begin{pmatrix} c_{11} - v^2\rho & 0 & 0 \\ 0 & c_{66} - v^2\rho & 0 \\ 0 & 0 & c_{55} - v^2\rho \end{pmatrix} \begin{pmatrix} U_1 \\ U_2 \\ U_3 \end{pmatrix} = 0 \tag{A.4}$$

Letting the determinant of this equation being zero gives nontrivial solutions. It is easily to find out that one pure longitudinal wave and two pure shear waves are supported by GaN bulk material. The longitudinal elastic wave (particle displacements polarized along x_1-axis) has its phase velocity $v = \sqrt{c_{11}/\rho}$; the shear elastic waves have phase velocities $v = \sqrt{(c_{11} - c_{12})/2\rho}$ and $\sqrt{c_{44}/\rho}$ (particle displacements polarized along x_2-axis and x_3-axis respectively) using $c_{55} = c_{44}$ and $c_{66} = (c_{11} - c_{12})/2$.

The same procedures can be taken if the elastic wave is supposed to propagate along x_2-axis or x_3-axis. It is found that the same longitudinal and shear velocities obtained in the case of x_2-axis propagation and this is not surprising because GaN is elastically isotropic in its c-plane (x_1-x_2 plane), [129]. In the third case of x_3-axis propagation, the elastic wave supports a longitudinal mode with velocity $\sqrt{c_{33}/\rho}$ and two shear modes with the same velocity $\sqrt{c_{44}/\rho}$.

Appendix B

Expression of matrix A defined in Adler's transmission matrix method, [43]

The motion dynamic equation (2.21) and constitutive relation (2.31) can be rewritten in a more compact form

$$\begin{aligned} \frac{\partial T'_{ij}}{\partial x_j} &= \rho_{ik}\frac{\partial^2 u'_k}{\partial t^2} \\ T'_{ij} &= c'_{ijkl}\frac{\partial u'_k}{\partial x_l} \end{aligned} \qquad j,l = 1,2,3;\ i,k = 1,\cdots,4 \tag{B.1}$$

H where T_{ij} $(i = 1,2,3)$ is stress and $T_{4j} \equiv D_j$ is the electrical displacement; u_k $(k = 1,2,3)$ is particle displacements and $u_4 \equiv V$ is the electric potential; $\rho_{i,i} \equiv \rho$ is mass density with $\rho_{44} = 0$ and all the other elements ρ_{ik} $(i \neq k)$ are identical null; $c_{ijkl}(i,j,k,l = 1,2,3)$ is the stiffness tensor, $c_{ij4l} \equiv e_{lij}$ and $c_{4jkl} \equiv e_{jkl}$ are the piezoelectric tensor, and $-c_{4j4l} \equiv \epsilon_{jl}$ are the permittivity.

Given the definition of the state variable

$$\boldsymbol{\tau} = [T_{12}\ T_{22}\ T_{32}\ D_2\ v_1\ v_2\ v_3\ \phi]^t \tag{B.2}$$

each element of this column vector is assumed to be in the form

$$F(\boldsymbol{r},t) = C_i e^{-(\alpha+j\gamma)x_2} e^{j\Omega(t-s_1x_1)} \tag{B.3}$$

Substitution of equation (B.3) into (B.1) yields, respectively

$$\frac{\partial T'_{i2}}{\partial x_2} = js_1\Omega T_{i1} - \Omega^2\rho_{ik}u'_k \tag{B.4}$$

$$T'_{ij} = -js_1\Omega c_{ijk1}u_k + c_{ijk2}\frac{\partial u'_k}{\partial x_2} \tag{B.5}$$

One must notice that the quantity j only appears as a suffix means it is an integer, and it denotes the imaginary unit $\sqrt{-1}$ in the rest cases.

Equation (B.5) gives, for $j = 1, 2$, a set of two equations

$$\begin{aligned} c'_{i1k2}\frac{\partial u'_k}{\partial x_2} &= T'_{i1} + js_1\Omega c'_{i1k1}u_k \\ c'_{i2k2}\frac{\partial u'_k}{\partial x_2} &= T'_{i2} + js_1\Omega c'_{i2k1}u_k \end{aligned} \tag{B.6}$$

In order to transform the tensor-notation relations into matrix equations, vectors $\boldsymbol{T}_1$ and $\boldsymbol{T}_2$ are introduced

$$\boldsymbol{T}_1 = [T_{11}T_{21}T_{31}D_1]^t \tag{B.7}$$

$$\boldsymbol{T}_2 = [T_{12}T_{22}T_{32}D_2]^t H \tag{B.8}$$

as well as the following 4×4 matrix G_{jl}

$$G_{jl} = \begin{pmatrix} c_{1j1l} & c_{1j2l} & c_{1j3l} & e_{l1j} \\ c_{2j1l} & c_{2j2l} & c_{2j3l} & e_{l2j} \\ c_{3j1l} & c_{3j2l} & c_{3j3l} & e_{l3j} \\ e_{j1l} & e_{j2l} & e_{j3l} & -\epsilon_{jl} \end{pmatrix} \tag{B.9}$$

In terms of the matrix G_{jl} and the vector $\boldsymbol{u}'$, $\boldsymbol{T}_1$ and $\boldsymbol{T}_2$, equation (B.6) becomes

$$\begin{aligned} \boldsymbol{G}_{12}\frac{\partial \boldsymbol{u}}{\partial x_2} &= \boldsymbol{T}_1 + js_1\Omega\boldsymbol{G}_{11}\boldsymbol{u} \\ \boldsymbol{G}_{22}\frac{\partial \boldsymbol{u}}{\partial x_2} &= \boldsymbol{T}_2 + js_1\Omega\boldsymbol{G}_{21}\boldsymbol{u} \end{aligned} \tag{B.10}$$

After a few matrix manipulations the following results can be obtained

$$\boldsymbol{T}_1 = \boldsymbol{G}_{12}\boldsymbol{G}_{22}^{-1}\boldsymbol{T}_2 + js_1\Omega(\boldsymbol{G}_{12}\boldsymbol{G}_{22}^{-1}\boldsymbol{G}_{21} - \boldsymbol{G}_{11})\boldsymbol{u} \tag{B.11}$$

$$\frac{\partial \boldsymbol{u}}{\partial x_2} = \boldsymbol{G}_{22}^{-1}\boldsymbol{T}_2 + js_1\Omega\boldsymbol{G}_{22}^{-1}\boldsymbol{G}_{21}\boldsymbol{u} \tag{B.12}$$

Substituting equation (B.11) into (B.4) yields

$$\frac{\partial \boldsymbol{T}_2}{\partial x_2} = j s_1 \Omega \boldsymbol{G}_{12} \boldsymbol{G}_{22}^{-1} \boldsymbol{T}_2 + (j s_1 \Omega)^2 (\boldsymbol{G}_{12} \boldsymbol{G}_{22}^{-1} \boldsymbol{G}_{21} - \boldsymbol{G}_{11}) \boldsymbol{u} - \Omega^2 \rho_{ik} \tag{B.13}$$

Now multiplying equation (B.12) by $j\Omega$ and putting together the resulting equation with (B.13), a set of first-order differential equation about the unknown state vector $\boldsymbol{\tau}$ as given by (2.38) in the main text is obtained, that is

$$\frac{d\boldsymbol{\tau}}{dx_2} = j\Omega A \boldsymbol{\tau} \tag{B.14}$$

where the system matrix A is defined by the following

$$A = \begin{pmatrix} \boldsymbol{G}_{12} \boldsymbol{G}_{22}^{-1} s_1 & (\boldsymbol{G}_{12} \boldsymbol{G}_{22}^{-1} \boldsymbol{G}_{21} - \boldsymbol{G}_{11})^2 + \boldsymbol{\rho} \\ \boldsymbol{G}_{22}^{-1} & \boldsymbol{G}_{22}^{-1} \boldsymbol{G}_{21} s_1 \end{pmatrix} \tag{B.15}$$

Appendix C

Transmission line model of SAW

The propagation of SAW in piezoelectric medium may be modeled as a transmission line problem, [130]. The SAW is described by the electric potential φ at the surface, which occurs along with the piezoelectric field coupled with the acoustic wave. The surface potential φ of the SAW is equated to the voltage V on the transmission line. The current I is defined so that

$$\varphi = V \tag{C.1}$$

$$P = \frac{1}{2} V I^* = \frac{1}{2} \varphi I^* \tag{C.2}$$

where P is the total power carried by the surface wave. Unlike the voltage, however, the current cannot be identified with any physical quantity associated with the surface wave. The characteristic impedance Z_0 is the ratio of the voltage V and the current I

$$Z_0 = \frac{V}{I} = \frac{|\varphi^2|}{2P} \tag{C.3}$$

Given the surface wave velocity v_R, the L and C parameters for the equivalent transmission line can thus be determined

$$C = \frac{1}{Z_0 v_R} \qquad L = \frac{Z_0}{v_R} \tag{C.4}$$

The characteristic impedance Z_0 as defined by equation (C.3) varies, of course, with different acoustic propagation direction and substrate orientation in anisotropic material. Apart from that, however, it depends on the beam width L as well. A wider SAW beam carries more power for a given amplitude φ and has a lower impedance. A quantity z_0 which is independent of the beam width can be defined

$$Z_0 = \frac{z_0}{L/\Lambda} \tag{C.5}$$

with Λ being the acoustic wave wavelength. Similarly, the characteristic admittance Y_0, which is proportional to the beam width, is given

$$Y_0 = \frac{1}{Z_0} = y_0 \frac{L}{\Lambda} \tag{C.6}$$

It is important to note that the characteristic impedance and admittance depends on the beam width measured in wavelength rather than meters. The reason for this is related to the fact that the SAW energy distribution in depth changes with wavelength rather than meters. The SAW gets more confined with shorter wavelength, i.e., higher frequency.

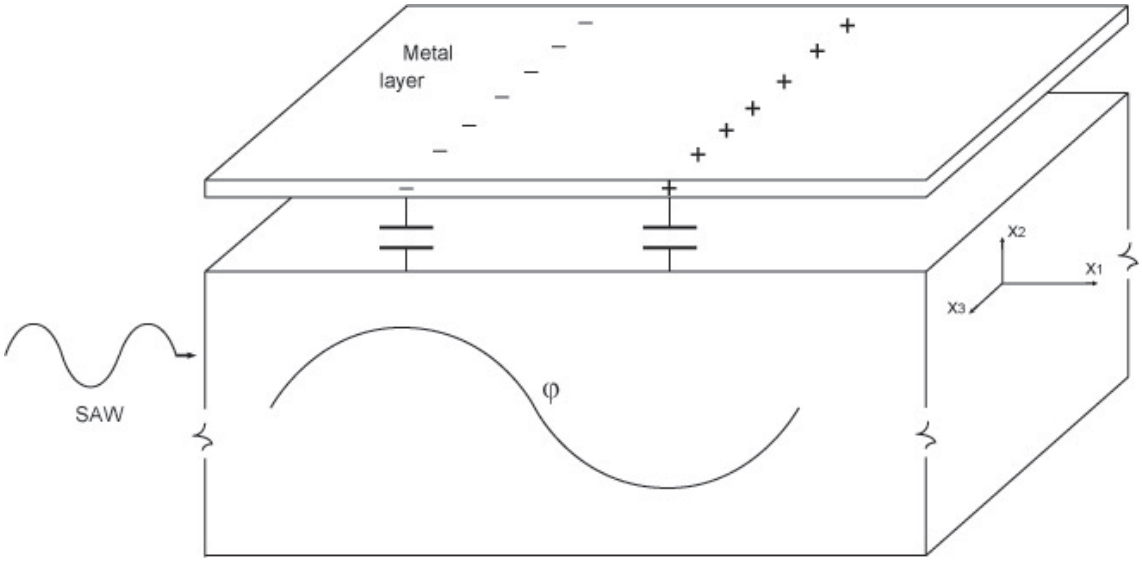

Figure C.1: Charges induced in a thin metal layer by a propagating surface wave.

In order to find the value of y_0 for a given SAW, a thin metal layer is put on the surface of the piezoelectric medium, figure C.1. There shown a little gap between the surface and the layer for clarity, however, the film is physically on the surface. The metal layer shorts out the piezoelectric field, causing a reduction in velocity and the reason for this is to be shown below. A quantity K^2 is introduced to denote the fractional change in velocity caused by the conductor

$$K^2 = 2\left|\frac{\Delta v_R}{v_R}\right| \tag{C.7}$$

It is called electromechanical coefficient used as a measure of ability of a piezoelectric material converting electrical signals to elastic ones. Since the SAW produces

an electrical potential φ at the surface, this potential induces charges in the conducting layer as shown in figure C.1. In terms of the transmission line, it is as if a capacitance ΔC per unit length is added. It is this capacitance changing that causes a reduction in velocity. Since $v_R = 1/\sqrt{LC}$, for small changes in velocity it gives

$$\left|\frac{\Delta v_R}{v_R}\right| = \frac{1}{2}\left|\frac{\Delta C}{C}\right| \tag{C.8}$$

and hence

$$K^2 = \frac{\Delta C}{C} \tag{C.9}$$

The present task is to find the relation between the characteristic admittance y and the electromechanical constant K^2 if the value of ΔC can be evaluated. There is surface charge density ρ_s induced in the sheet conductor, the magnitude of which is expected to be proportional to the potential φ of the surface wave. Since ρ_s is the charge per unit area, the capacitance per unit length ΔC is given by

$$\Delta C = -\frac{\rho_s L}{\varphi} \tag{C.10}$$

The negative sign reflects the fact that negative charges accumulate in the region of positive potential as shown in figure C.1. With the given surface potential φ generated by the acoustic wave, the charge ρ_s in the conducting layer also generates a electric field in the substrate, which varies with x_1 as a traveling wave. The potential produced by this induced electronic field is assumed in the form

$$\psi = \psi_s e^{\alpha x_2} e^{-j\Omega s_1 x_1} \tag{C.11}$$

where α is some positive constant and ψ_s is its peak value at the surface.

In the substrate with no free charges inside, Laplace equation is satisfied by the potential field

$$\frac{\partial^2 \psi}{dx_1^2} + \frac{\partial^2 \psi}{dx_2^2} = 0 \tag{C.12}$$

which is used to determine the value of the decaying constant α

$$\alpha^2 - (\Omega s_1)^2 = 0 \tag{C.13}$$

that is

$$\alpha = \Omega|s_1| \tag{C.14}$$

Therefore the potential field generated by the induced surface charge ρ_s is

$$\psi = \psi_s e^{\Omega|s_1|x_2} e^{-j\Omega s_1 x_1} \tag{C.15}$$

In the assumption of quasi-static approximation, equation (2.32) in Chapter 2 is valid, and the electronic displacement $\boldsymbol{D}$ induced by ρ_s is given

$$D_1 = -\epsilon_p \frac{\partial \psi}{\partial x_1} = j\Omega s_1 \epsilon_p \psi \tag{C.16}$$

$$D_2 = -\epsilon_p \frac{\partial \psi}{\partial x_2} = \Omega|s_2|\epsilon_p \psi \tag{C.17}$$

$$D_3 = -\epsilon_p \frac{\partial \psi}{\partial x_3} = 0 \tag{C.18}$$

where ϵ_p is the substrate permittivity and the substrate is assumed to be isotropic. While in the air similar calculation can be done with the only change replacing ϵ_p by ϵ_0 and adding a minus sign to α

$$D_2^{\text{air}} = -\epsilon_0 \Omega|s_1|\psi \tag{C.19}$$

The discontinuity of D_1 in the substrate and in the air is equal to the surface charge density ρ_s. Hence

$$\rho_s = (\epsilon_p + \epsilon_0)\Omega|s_1|\psi_s \tag{C.20}$$

Combing equation (C.10) and (C.20) it gives an evaluation of ΔC

$$\Delta C = 2\pi(\epsilon_p + \epsilon_0)\frac{L}{\Lambda}\left(-\frac{\psi_s}{\varphi}\right) \tag{C.21}$$

In deriving this equation the relation $\Omega s_1 = 2\pi/\Lambda$ with Λ being the SAW wavelength has been used. Note that φ is the potential produced by the SAW at the surface and ψ_s is the potential produced by the induced charges at the surface. Those two must be equal and opposite since no longitudinal electric field (E_1) can exist in the conductor film, that is

$$E_1 = j\Omega s_1(\varphi + \psi_1) \tag{C.22}$$

or

$$\psi_s = -\varphi \tag{C.23}$$

Therefore equation (C.21) becomes

$$\Delta C = 2\pi(\epsilon_p + \epsilon_0)\frac{L}{\Lambda} \tag{C.24}$$

Substituting equation (C.24) and (C.4) into equation (C.9) yields

$$K^2 y_0 = 2\pi C_s v_R \tag{C.25}$$

and

$$C_s = \epsilon_p + \epsilon_0 \tag{C.26}$$

It must be noticed that in the derivation of equation (C.25), a relation of $D = \epsilon E$ has been used for the piezoelectric substrate rather than the the more complete one $D = \epsilon E + eS$ (equation (2.17)). The assumption is that the acoustic fields remain undisturbed by this additional field produced by the induced charges.

Appendix D

Maxwell's Equations and Electromagnetic Fields

D.1 Maxwell's Equations

In general, electric and magnetic fields are vector quantities that have both magnitude and direction. The relations and variations of the electric and magnetic fields, charges, and currents associated with electromagnetic waves are governed by physical laws, which are known as Maxwell's equations, [131]. The differential form of Maxwell's equation is as followed

$$\nabla \times \boldsymbol{H} = \frac{\partial \boldsymbol{D}}{\partial t} + \boldsymbol{J} \tag{D.1}$$

$$\nabla \times \boldsymbol{E} = -\frac{\partial \boldsymbol{B}}{\partial t} \tag{D.2}$$

$$\nabla \cdot \boldsymbol{D} = \rho \tag{D.3}$$

$$\nabla \cdot \boldsymbol{B} = 0 \tag{D.4}$$

All these fields quantities, $\boldsymbol{H}$, $\boldsymbol{D}$, $\boldsymbol{B}$, $\boldsymbol{E}$ and $\boldsymbol{J}$ are assumed to be time-varying, and each is a function of the space coordinates and time, that is

$$\boldsymbol{F} = \boldsymbol{F}(x, y, z, t) \tag{D.5}$$

The definitions and units of the quantities are

$\boldsymbol{H}$ magnetic field intensity (A/m)

$\boldsymbol{D}$ electric displacement (C/m^2)

$\boldsymbol{B}$ magnetic flux density ($\mathrm{Wb/m^2}$)

$\boldsymbol{E}$ electric field intensity (V/m)

$\boldsymbol{J}$ current density ($\mathrm{A/m^2}$)

ρ charge density ($\mathrm{C/m^2}$)

Materials contain charged particles, and when these materials are subjected to electromagnetic fields, their charged particles interact with the electromagnetic field vectors, producing currents and modifying the electromagnetic wave propagation in these media compared to that in free space. Equations relating the electromagnetic fields and materials are referred to as the constitutive relations. In isotropic medium, they are expressed as

$$\boldsymbol{D} = \epsilon \boldsymbol{E} \tag{D.6}$$

$$\boldsymbol{B} = \mu \boldsymbol{H} \tag{D.7}$$

where ϵ is the material permittivity (dielectric constant) and μ is the material permeability (magnetic conductivity). Combing the constitutive relations with Maxwell's equations yields solutions for electromagnetic fields in any materials.

In many practical systems involving electromagnetic waves the time variations are of cosinusoidal form and are referred to as time harmonic. In general, such time variations can be represented by $e^{j\omega t}$ with j being the unit of imaginary number $j = \sqrt{-1}$ and ω being the angular frequency. The instantaneous electromagnetic field vectors can be related to their complex forms by

$$F(x, y, z, t) = \mathrm{Re}[F(x, y, z)e^{j\omega t}] \tag{D.8}$$

where the operator Re means the real part of the fields. In what follows, the Maxwell's equations for harmonic electromagnetic fields can be written in a simpler form, that is

$$\nabla \times \boldsymbol{H} = j\omega\epsilon \boldsymbol{E} + \boldsymbol{J} \tag{D.9}$$

$$\nabla \times \boldsymbol{E} = -j\omega\mu \boldsymbol{H} \tag{D.10}$$

$$\nabla \cdot \boldsymbol{H} = \rho \tag{D.11}$$

$$\nabla \cdot \boldsymbol{E} = 0 \tag{D.12}$$

in which the constitutive relations (D.6) and (D.7) have been used. No strict distinctions are drawn between the notations of the value of the instantaneous fields and their complex forms throughout this monograph. If the complex spatial quantities can be found, it is then a very simple procedure to find their corresponding instantaneous forms by using equation (D.8).

D.2 Boundary Condition

As previously presented, the differential form of Maxwell's equations are used to solve for the field vectors provided the field quantities which possess continuous distributions. Along boundaries where the media involved exhibit discontinuities in electrical properties, the field quantities are thus discontinuous and their behavior across the boundaries is governed by the boundary conditions. At points of discontinuity in the field vectors, the derivatives of the field have no meaning and cannot be properly used to define the field vectors across these boundaries. In order to derive the boundary conditions, the integral form of Maxwell's equations for time-harmonic fields is useful

$$\oint_l \boldsymbol{H} \cdot d\boldsymbol{l} = \iint_S \boldsymbol{J} \cdot d\boldsymbol{s} + j\omega \iint_S \boldsymbol{D} \cdot d\boldsymbol{s} \tag{D.13}$$

$$\oint_l \boldsymbol{E} \cdot d\boldsymbol{l} = -j\omega \iint_S \boldsymbol{B} \cdot d\boldsymbol{s} \tag{D.14}$$

$$\oiint_S \boldsymbol{D} \cdot d\boldsymbol{s} = Q \tag{D.15}$$

$$\oiint_S \boldsymbol{B} \cdot d\boldsymbol{s} = 0 \tag{D.16}$$

where Q is total charges in the volume of interest. Consider an interface between two media, as shown in figure D.1. It is assumed that there is no source along the interface.

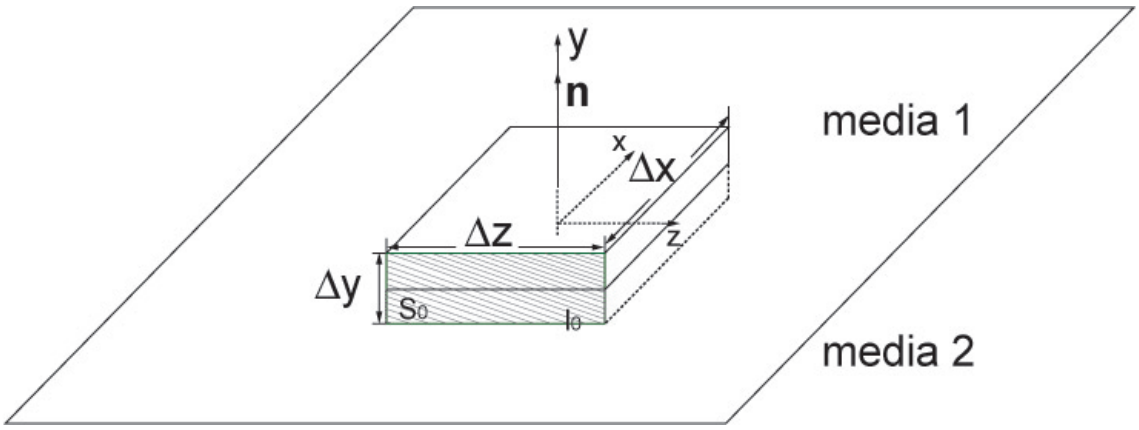

Figure D.1: Geometry for boundary conditions.

At a given point along the interface, a rectangular thin box is chosen which covered by a surface S. Denote the boundary (in green) of one of its surface by l_0 and the surrounded area by S_0 (in shadow). The x, y, z coordinate system is chosen to represent the local geometry of the box. Applying Maxwell's equation (D.13), as the height Δy of the rectangle becomes progressively shorter, the area S_0 also becomes vanishingly smaller so that the contributions of the surface integral in equation (D.13) are negligible. In addition, the contributions of the line integral along Δy are also minimal so that in the limit $\Delta y \to 0$, the left hand side (LHS) of equation (D.13), i.e. the line integral along l_0, reduces to

$$LHS = (H_{1t} - H_{2t})\Delta x \tag{D.17}$$

where H_{1t} and H_{2t} represent, respectively, the tangential component of the electric field in media 1 and 2 along the interface. As $\Delta y \to 0$, the current density $\boldsymbol{J}$ reduces to $\boldsymbol{J}_s$, the current density on surface with its direction along the interface. Hence the right hand side (RHS) of equation (D.13) becomes

$$RHS = J_s \Delta x \tag{D.18}$$

Combining equation (D.17) and (D.18) yields

$$H_{1t} - H_{2t} = J_s \tag{D.19}$$

or in vector form

$$\boldsymbol{n} \times (\boldsymbol{H}_1 - \boldsymbol{H}_2) = \boldsymbol{J}_s \tag{D.20}$$

where $\boldsymbol{n}$ denotes a unit vector with its direction along the normal of the interface from media 2 to 1. Equation (D.20) state that the tangential components of the magnetic field across an interface between two media, along which there exists a surface electric current $\boldsymbol{J}_s$ (A/m), are discontinuous by an amount equal to the electric current density.

Using a similar procedure on the same rectangle but for equation (D.14), it is obtained

$$E_{1t} - E_{2t} = 0 \tag{D.21}$$

or

$$\boldsymbol{n} \times (\boldsymbol{E}_1 - \boldsymbol{H}_2) = 0 \tag{D.22}$$

which states that the tangential components of the electric field across an interface are continuous.

The boundary condition on the normal components of the electric and magnetic quantities on an interface along which a surface charge density ρ_s resides on a very thin layer, can be derived by applying the equation (D.15), that is

$$D_{1n} - D_{2n} = \rho_s \tag{D.23}$$

with D_{1n} and D_{2n} being the normal components of the electric displacement vector. This equation can be written in vector form

$$\boldsymbol{n} \cdot (\boldsymbol{D}_1 - \boldsymbol{D}_2) = \rho_s \tag{D.24}$$

which states that the normal components of the electric field across an interface are continuous.

Using a similar procedure on the same rectangle but for equation (D.16), it is obtained

$$B_{1n} - B_{2n} = 0 \tag{D.25}$$

or

$$\boldsymbol{n} \cdot (\boldsymbol{B}_1 - \boldsymbol{B}_2) = 0 \tag{D.26}$$

which states that the tangential components of the electric field across an interface are continuous.

If both the media are lossless along whose interface $\rho_0 = 0$ and $J_s = 0$, the boundary conditions for the electromagnetic quantities become

$$\boldsymbol{n} \times (\boldsymbol{H}_1 - \boldsymbol{H}_2) = 0 \tag{D.27}$$

$$\boldsymbol{n} \times (\boldsymbol{E}_1 - \boldsymbol{H}_2) = 0 \tag{D.28}$$

$$\boldsymbol{n} \cdot (\boldsymbol{D}_1 - \boldsymbol{D}_2) = 0 \tag{D.29}$$

$$\boldsymbol{n} \cdot (\boldsymbol{B}_1 - \boldsymbol{B}_2) = 0 \tag{D.30}$$

D.3 Wave Equation

Consider a homogenous medium without source, i.e. $\rho = \boldsymbol{J} = 0$. Taking the curl of both sides of equation (D.10) gives

$$\nabla \times \nabla \times \boldsymbol{E} = -j\omega\mu\nabla \times \boldsymbol{H} \tag{D.31}$$

Using the vector identity

$$\nabla \times \nabla \times \boldsymbol{F} = \nabla(\nabla \cdot \boldsymbol{F}) - \nabla^2 \boldsymbol{F} \tag{D.32}$$

into the left side of equation (D.31) and substituting equation (D.9) into the right side, noticing the divergence of electric field is zero (equation (D.12)), equation (D.31) can be written

$$\nabla^2 \boldsymbol{E} + \omega^2 \mu\epsilon \boldsymbol{E} = 0 \tag{D.33}$$

For magnetic field $\boldsymbol{H}$, similar equation can be obtained

$$\nabla^2 \boldsymbol{H} + \omega^2 \mu\epsilon \boldsymbol{E} = 0 \tag{D.34}$$

Equation (D.33) (or (D.34)) is the well-known Helmholtz equation, which is followed by electromagnetic fields.

The solution of equation (D.33) can be a plane wave, which is assumed in the form

$$\boldsymbol{E} = \boldsymbol{E}_0 e^{-j(k_x x + k_y y + k_z z)} = \boldsymbol{E}_0 e^{-j(\boldsymbol{k}\cdot r)} \tag{D.35}$$

where $\boldsymbol{E}_0$ is a constant vector and $\boldsymbol{k}$ is wave vector, of which the direction is the propagation direction of the electric field and the magnitude is $k = 2\pi/\lambda$ with λ being the wavelength in medium. Substituting equation (D.35) into the wave equation (D.33) yields

$$k^2 = \omega^2 \mu \epsilon \tag{D.36}$$

which is called the dispersion relation of a plane electromagnetic wave in this medium.

In vacuum, equation (D.36) becomes

$$k_0^2 = \omega^2 \mu_0 \epsilon_0 \tag{D.37}$$

With the assumption $\mu \approx \mu_0$, in dielectric material, it gives $\epsilon = n^2 \epsilon_0$ with n being the refractive index. Combining equation (D.36) and (D.37) it gives

$$k = n k_0 \tag{D.38}$$

Define a relative permittivity $\epsilon_r = \epsilon/\epsilon_0$, one has

$$\epsilon_r = n^2 \tag{D.39}$$

Using the expressions of wave vector and relative permittivity, the wave equation (D.33) can be written

$$(\nabla^2 + \epsilon_r k_0^2)\boldsymbol{E} = 0 \tag{D.40}$$

or

$$(\nabla^2 + n^2 k_0^2)\boldsymbol{E} = 0 \tag{D.41}$$

Appendix E

Dielectric Optical Waveguide

Utilizing the fact that optical waves undergo total reflection in some condition when transmitting from a dielectric of higher refractive index into one of lower index, optical waveguide technique has been developed to confine and modify optical paths. Starting from Maxwell's equations in a no-source homogeneous medium, as given in Appendix D, the wave equation is

$$(\nabla^2 + n^2 k_0^2)\boldsymbol{E} = 0 \tag{E.1}$$

where n is the refractive index of the medium. Since the time-harmonic electric field propagating in the z-direction is of interest, it is assumed the electric field in vector is in the form

$$\boldsymbol{E}(x, y, z) = \boldsymbol{E}_0 f(x, y) e^{-j\xi z} \tag{E.2}$$

as a solution to equation (E.1). The magnitude of $\boldsymbol{E}_0$ is the amplitude of the electric field and its direction indicates the polarization of the electric field and $f(x, y)$ is usually normalized such that $\int |f(x, y)|^2 dA = 1$. Substituting equation (E.2) into (E.1) and factoring out common terms, it is found that the transverse amplitude $f(x, y)$ must satisfy

$$\nabla^2 f(x, y) + (n^2 k_0^2 - \xi^2) f(x, y) = 0 \tag{E.3}$$

The concept of effective index n_{eff}, i.e. the normalized propagation constant, can also be introduced so that

$$\xi = n_{\text{eff}} k_0 \tag{E.4}$$

which is used to describe a specific mode supported by a given structure.

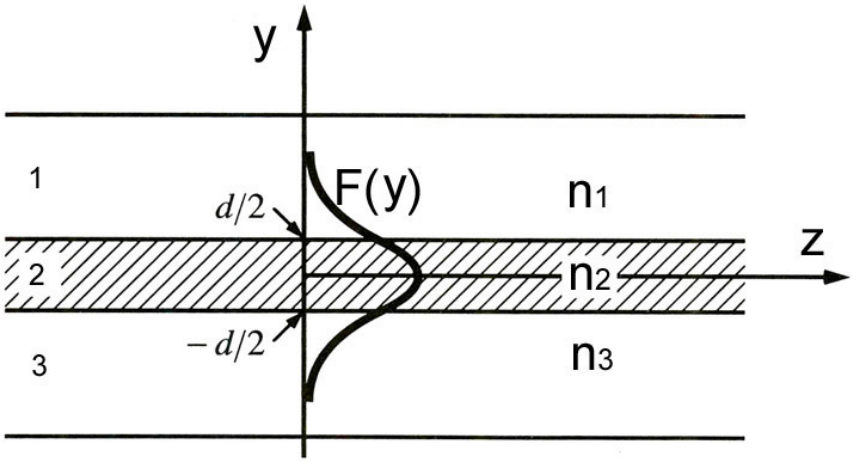

Figure E.1: Schematic of a three-layer slab waveguide. Indices are assumed to be uniform in the y-axis.

Figure E.1 shows a simple configuration of a slab waveguide composed of three layers with generally different index for each layer. For one dimensional slab case, i.e. the medium uniform along x, TE waves polarized along x-axis is considered and there is no variation along x-axis for the field. The calculation for TM waves is analogous with slightly more mathematical complexity. An exact solution by solving equation (E.3) for uniform index in each of the three regions is achievable and using boundary conditions at the interfaces then gives the appropriate propagation constant ξ.

E.1 Symmetric and asymmetric three layer slab dielectric waveguide

In the case of a symmetric slab waveguide, i.e. $n_1 = n_3$, the solution in the central region is assumed in the form

$$F_2(y) = \begin{cases} A\cos k_y y & \text{(symmetric solutions)} \\ A\sin k_y y & \text{(antisymmetric solutions)} \end{cases} \tag{E.5}$$

In region 1,

$$F_1(y) = Be^{-\gamma y} \tag{E.6}$$

Substituting equation (E.5) and E.6 into E.3 with $n_3 = n_1$, respectively, yields

$$k_y^2 = n_2^2 k_0^2 - \xi^2$$
$$\gamma^2 = \xi^2 - n_1^2 k_0^2 \tag{E.7}$$

In the region 3, it is known that $F_3(y) = Be^{\gamma y}$, but by symmetry in this case, only one boundary condition at $y = d/2$ between regions 1 and 2.

for TE waves at $y = d/2$, the continuity of both the tangential electric and magnetic fields requires $F_1 = F_2$ and $\partial F_1/\partial y = \partial F_2/\partial y$. For symmetric solutions, this gives

$$A\cos\frac{k_y d}{2} = Be^{-\gamma d/2} \tag{E.8}$$

$$Ak_y \sin\frac{k_y d}{2} = B\gamma e^{-\gamma d/2} \tag{E.9}$$

Dividing equation (E.9) by E.8 yields

$$\gamma = k_y \tan\frac{k_y d}{2} \tag{E.10}$$

Similarly, for the antisymmetric solutions, it is obtained

$$\gamma = -k_y \cot\frac{k_y d}{2} \tag{E.11}$$

The propagation constants of the TE wave are found from a numerical or graphical solution of equation (E.10) and (E.11). A simple and well-known graphic solution is described here since it clearly shows the way in which the number of TE modes relies on both the thickness d and the index step. By putting $u = \frac{1}{2}k_y d$ and $v = \frac{1}{2}\gamma d$, equation slab symm gamma becomes $v = u\tan u$ and

$$u^2 + v^2 = (n_2^2 - n_1^2)\left(\frac{\pi d}{\lambda_0}\right)^2 \equiv V^2 \tag{E.12}$$

Since u and v are both positive values, the propagation constants may be found in this case from the intersection of both the curve $v = u\tan u$ and a circle of known radius $V = (n_2^2 - n_1^2)^{1/2}(\pi/\lambda_0)$ in the first quadrant of the uv plane. A similar graphic construction for the solution of equation E.11 can be obtained by plotting $v = -u\cot u$ and the circle on the uv plane. Figure E.2 (to be plotted) shows such a graphic method for three values of V. For $V = 1$, there is only one solution. There are two solutions when V is 2.5 and three when $V = 4$. Notice that the number of solutions apparently depends on the value of V. In fact, for V between 0 and $\frac{1}{2}\pi$,

there is just one symmetric solution. The first antisymmetric solution appears when V is greater than $\frac{1}{2}\pi$. More symmetric and antisymmetric solutions appear if the magnitude of V keeps increasing.

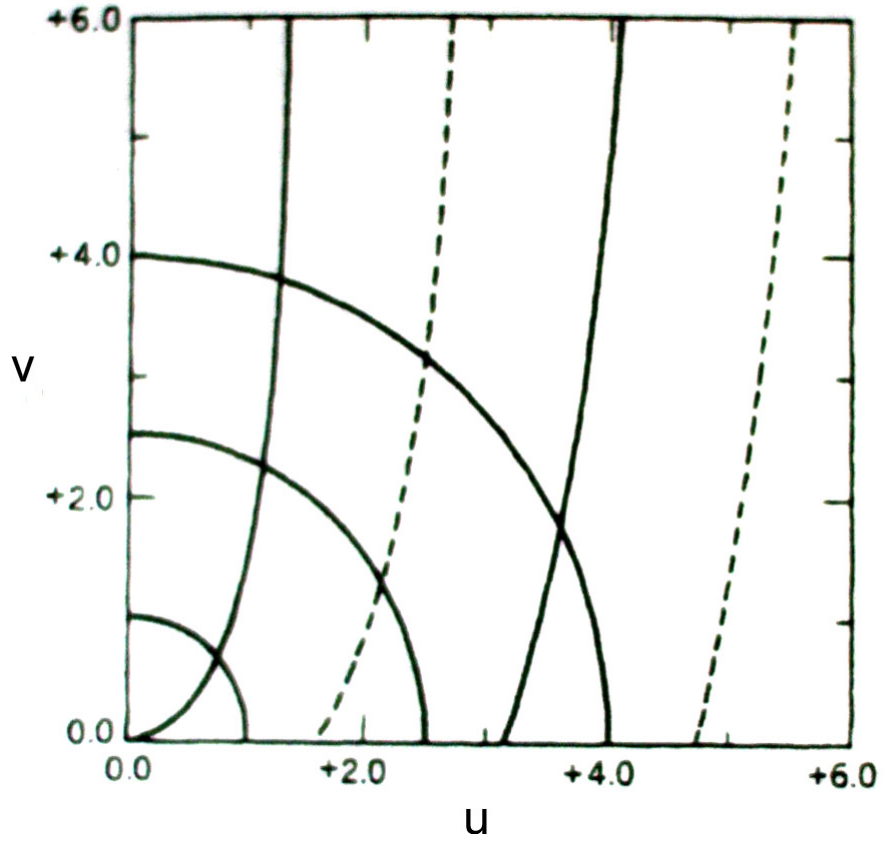

Figure E.2: Graphic solution for three values of V. Solid curve denotes $v = u\tan u$ and the dashed curves are $v = -u\cot u$, [132]

For the TM waves, the continuity of the tangential electric and magnetic fields at the boundaries results in an additional factor of n_2^2/n_1^2 on the left side of equation (E.10) and inside the brackets of the $\tan^{-1}$ function in equation (E.10). Similar graphic solutions can be obtained using the same procedure.

To add additional generality to the present case, the above procedures can be repeated for asymmetric slab waveguide given $n_1 \neq n_3$. for the TE waves, the characteristic equation (E.10) becomes

$$\tan k_y d = \frac{(\gamma_1/k_y) + \gamma_3/k_y}{1 - \gamma_1\gamma_3/k_y^2} \tag{E.13}$$

where γ_1 and γ_3 are the decay constants in the upper and lower cladding regions, respectively, defined as in equation (E.7). To solve this equation graphically, it is convenient to define a normalized frequency Q, propagation parameter b, and

asymmetry parameter a so as to display the results:

$$\begin{aligned} A &\equiv k_0 d(n_2^2 - n_3^2)^{1/2} \\ b &\equiv \frac{n_{\text{eff}}^2 - n_3^2}{n_2^2 - n_3^2} \\ a &\equiv \frac{n_3^2 - n_1^2}{n_2^2 - n_3^2} \end{aligned} \tag{E.14}$$

It gives in figure E.3 plots of the normalized propagation parameter as a function of the normalized frequency for a range of normalized asymmetry parameters.

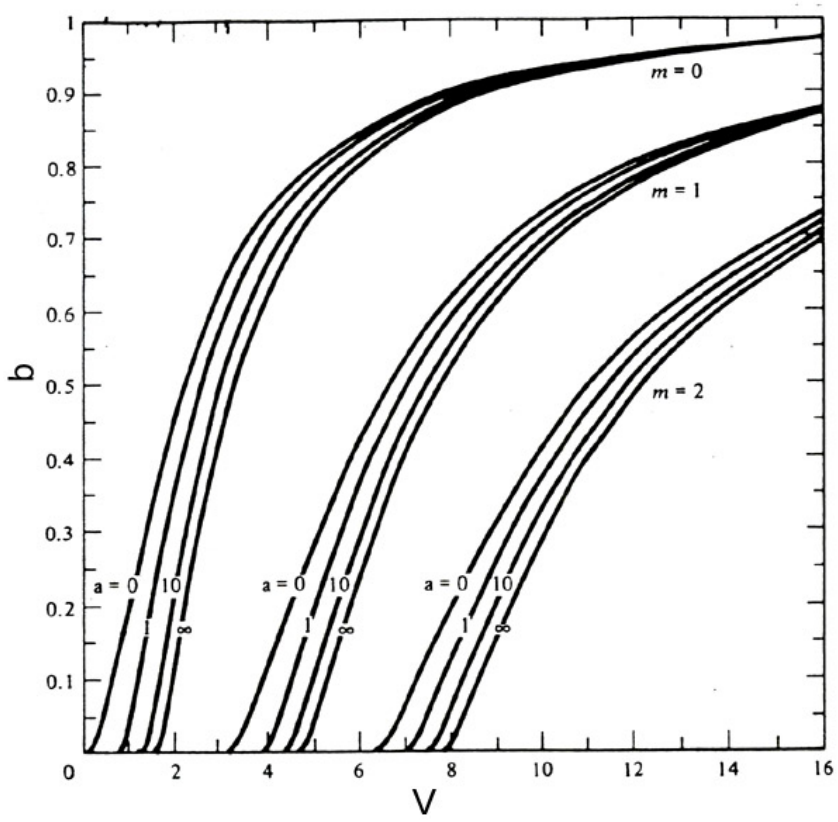

Figure E.3: Normalized propagation parameter versus normalized frequency for a range of asymmetries for the first three TE modes, [133]

E.2 Confinement Factor

The confinement factor for the three-layer slab waveguide is defined as the fraction of the optical energy that is contained in the active slab region. This fraction can be given

$$\begin{aligned}\Gamma &= \frac{\int_{-d/2}^{d/2} E \cdot H^* dy}{\int_{-\infty}^{\infty} E \cdot H^* dy} \\ &= \frac{n_2}{n_{\text{eff}}} \frac{\int_{-d/2}^{d/2} |F(y)|^2 dy}{\int_{-\infty}^{\infty} |F(y)|^2 dy}\end{aligned} \tag{E.15}$$

This concept can be expended to multilayer waveguide structure by replacing the integration limit in the numerator by the corresponding value for any layer.

E.3 Effective index method

Although simple layered structures such as dielectric slabs can be used for waveguiding purposes, the confinement of energy is only limited to one dimension. In practical cases like integrated optics or guided-wave optics, two dimensional waveguides and ridge waveguides are broadly used. Figure E.4 illustrate an example of such ridge waveguide. Exact analytical treatment of these waveguide structures is not possible. However, approximate analytical approaches are available and effective index method is the simplest one.

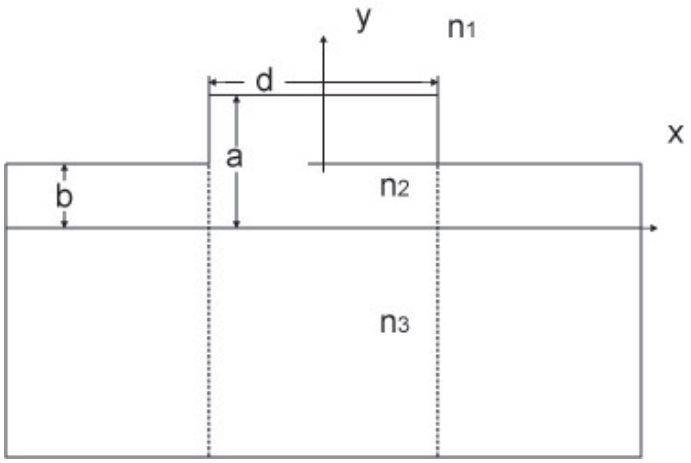

Figure E.4: Schematics of a typical structure of ridge waveguides.

In figure E.4, three regions are divided, the ridge and the rest two parts. The thickness a of the layer in the ridge part is chosen to be greater than the layer thickness b in the side parts because the confinement of electromagnetic fields at the ridge is of interest. Materials characterized by refractive index and layer structures in different regions are as marked in the figure.

In each region, the confinement along the vertical direction (y-axis) is exactly identical to that of the asymmetric slab waveguide. For simplicity, it is assumed to

be only one TE mode is supported by those segments of the slab waveguides. The propagation constant of the confined mode inside the ridge is, however, different from those on both sides of the ridge because of the difference in layer thickness. The effective index defined equation (E.4) for the three parts is

$$n_{\text{eff}}(x) = \begin{cases} n_b & x > -\frac{1}{2}d \\ n_a & -\frac{1}{2}d < x \quad \frac{1}{2}d \\ n_b & x < \frac{1}{2}d \end{cases} \tag{E.16}$$

where n_a and n_b are the effective indices of refraction.

In the method of effective index, lateral waveguiding is treated by taking equation (E.16) as a slab waveguide structure along the x direction. Thus, confinement of electromagnetic waves requires that $n_a > n_b$. This is always true when the thickness a is greater than b. This conclusion can be easily verified in the waveguide theory that the effective index of any confined mode is an increasing function of layer thickness.

E.4 Waveguiding in multiple Layers

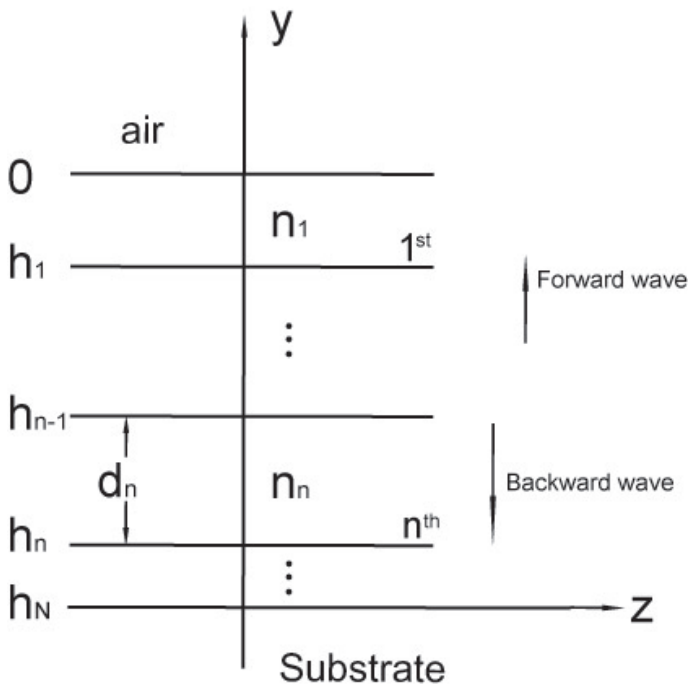

Figure E.5: Schematics of s multiple layer system between air and a semi-infinite substrate.

Analogous with transfer matrix method applied to the acoustic wave calculation in layered medium, the propagation of guided optical waves can be solved following the same concept. Indices for a thin layer and its neighbour layers are illustrated in figure E.5. Assuming the material is uniform along y-axis, the general solution of electric field satisfying equation (E.3) is

$$F(x) = ae^{-jk_x(x-h_n)} + be^{jk_x(x-h_n)} \equiv A_n(x) + B_n(x) \tag{E.17}$$

where constants a and b are amplitudes of the forward and backward waves in each layer. The x components of the wave vectors are given by

$$k_x^2 + \xi^2 = (n_n k_0)^2 \tag{E.18}$$

with β being the propagation constant along z-axis.

The variables $A(x)$ and $B(x)$ in any layer, are linked with ones in its adjacent layer by matching the boundary conditions at their interface, i.e.

$$\begin{aligned} A_n(x)e^{jk_x d_n} + B_n(x)e^{-jk_x d_n} &= A_{n-1}(x) + B_{n-1}(x) \\ -k_x^{(n)}A_n(x)e^{jk_x d_n} + k_x^{(n)}B_n(x)e^{-jk_x d_n} &= -k_x^{(n-1)}A_{n-1}(x) + k_x^{(n-1)}B_{n-1}(x) \end{aligned} \tag{E.19}$$

which can be rewritten in the form of matrices

$$\begin{pmatrix} A_n \\ B_n \end{pmatrix} = T_n \begin{pmatrix} A_{n-1} \\ B_{n-1} \end{pmatrix} \tag{E.20}$$

and

$$T_n = \begin{pmatrix} \frac{1}{2}\left(1 + \frac{k_x^{(n-1)}}{k_x^n}\right) e^{-jk_x d_n} & \frac{1}{2}\left(1 - \frac{k_x^{(n-1)}}{k_x^n}\right) e^{jk_x d_n} \\ \frac{1}{2}\left(1 - \frac{k_x^{(n-1)}}{k_x^n}\right) e^{-jk_x d_n} & \frac{1}{2}\left(1 + \frac{k_x^{(n-1)}}{k_x^n}\right) e^{jk_x d_n} \end{pmatrix} \tag{E.21}$$

Therefore, for an entire N layer system as shown in figure E.5, the chain-product of the cascaded transfer matrices gives

$$T = T_N T_{N-1} \cdots T_2 T_1 \tag{E.22}$$

and the electric field in the air and the substrate are coupled

$$\begin{pmatrix} A \\ B \end{pmatrix}_{\text{sub}} = T \begin{pmatrix} A \\ B \end{pmatrix}_{\text{air}} \tag{E.23}$$

where the subscript 'sub' denotes parameters in the substrate.

In the case of light propagating as guided waves in the layered system, optical fields must be decaying in the air and substrate. Given the fact that there is no waves coming from the positive or negative infinite, it is assumed

$$\begin{aligned} B_1 &= 0 \\ A_N &= 0 \end{aligned} \tag{E.24}$$

and

$$\begin{aligned} k_x^{(air)} &= \sqrt{k_0^2 - \beta^2} = \alpha j \\ k_x^{(sub)} &= \sqrt{n_{sub}^2 k_0^2 - \beta^2} = \gamma j \end{aligned} \qquad \alpha, \gamma > 0 \tag{E.25}$$

A numerical method in the aid of computer can thus be applied to obtain proper propagation constants β, i.e. n_{eff}. The range of the possible magnitude of n_{eff} is that one must greater than the index in the substrate but smaller than the maximal index value of the layers.

Appendix F

Analysis of Waveguide with Small Perturbation

Consider a slab dielectric waveguide of layered structure, defined by $\epsilon = \epsilon_r(y)\epsilon_0$, as shown in figure F.1. Any field quantities of the electromagnetic wave in this region satisfy the wave equation (D.40), that is

$$(\nabla^2 + \epsilon_r(y)k_0^2)\boldsymbol{F} = 0 \tag{F.1}$$

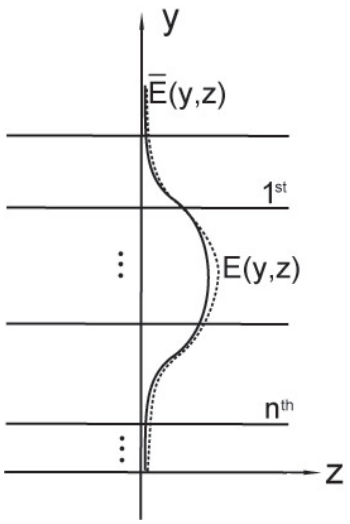

Figure F.1: Schematics of slab waveguide in layered structure. $\bar{E}(y,z)$ and $E(y,z)$ are field solutions of the structure without and with perturbation of ϵ, respectively.

In the present case the electric field is assumed to be TE polarized, i.e. $\boldsymbol{E} = \bar{E}_x(y,z)$. The wave equation for electric field thus becomes

$$(\frac{\partial^2}{\partial y^2} + \frac{\partial^2}{\partial z^2} + \epsilon_r(y)k_0^2)\bar{E}(y,z) = 0 \tag{F.2}$$

The solution of the electric field is supposed to be expressed as a product of two independent function, that is

$$\bar{E}(y,z) = \bar{f}(y)\bar{h}(z) \tag{F.3}$$

Substituting the variable separation equation (F.3) back to (F.2), dividing out by $f(y)h(z)$, gives

$$\frac{1}{\bar{f}(y)}\frac{d^2\bar{f}(y)}{dy^2} + \epsilon_r(y)k_0^2 = -\frac{1}{\bar{h}(z)}\frac{d^2\bar{h}(z)}{dz^2} \tag{F.4}$$

Since the LHS is purely a function of y and the RHS is purely a function of z, it follows that equation (F.4) can be satisfied only if both LHS and RHS equal to a constant, denoted as ξ^2, that is for the RHS

$$\frac{d^2\bar{h}(z)}{dz^2} + \bar{\xi}^2\bar{h}(z) = 0 \tag{F.5}$$

for the LHS

$$\frac{d^2\bar{f}(y)}{dy^2} + \epsilon_r(y)k_0^2\bar{f}(y) = \bar{\xi}^2\bar{f}(y) \tag{F.6}$$

Following equation F.5 the solution is

$$\bar{h}(z) = e^{-j\bar{\xi}z} \tag{F.7}$$

and thus ξ has the physical sense of propagation constant, which is in general complex.

Equation F.6, treating $\bar{\xi}^2$ as eigenvalue, can be recognized as an eigen function problem, which can be solved combining with proper boundary conditions.

For the present study assume that, for appropriate boundary conditions, equation (F.6) admits solutions of eivenvectors $\bar{f}_p(y)$ corresponding to eigenvalues $\bar{\xi}_p$ with $p = 1, 2, 3\cdots$, .etc.

Therefore, equation (F.6) can be rewritten

$$\frac{d^2\bar{f}_p(y)}{dy^2} + (\epsilon_r(y)k_0^2 - \bar{\xi}_p^2)\bar{f}_p(y) = 0 \tag{F.8}$$

where $\bar{f}_p(y)$ is the modes of the waveguide structure defined by $\epsilon_r(y)$ and $\bar{\xi}_p$ is the corresponding propagation constant.

Suppose there is a small perturbation on the waveguide structure. The perturbation is assumed to be via ϵ, i.e.

$$\epsilon = (\epsilon_r(y) + \Delta\epsilon_r(y))\epsilon_0 \tag{F.9}$$

given that

$$\left|\frac{\Delta\epsilon_r}{\epsilon_r}\right| << 1 \tag{F.10}$$

Referring to equation (F.2), this equation is rewritten

$$(\frac{\partial^2}{\partial y^2} + \frac{\partial^2}{\partial z^2} + (\epsilon_r(y) + \Delta\epsilon_r(y))k_0^2)E(y,z) = 0 \tag{F.11}$$

In the general analysis, equation (F.11) is to be solved as a problem of a waveguide defined by $\epsilon_r(y) + \Delta\epsilon_r(y)$ rather than $\epsilon_r(y)$ with the same procedures done to the unperturbed waveguide.

Alternately, equation (F.11) can also be solved using a function expansion technique. The solution of a particular mode $F_p(y,z)$ is expressed as a linear summation of a complete set, that is

$$E_p(y,z) = \sum_m a_{pm}(z)\phi_m(y) \tag{F.12}$$

where $\phi_m(y)$ is an appropriate set of complete functions. For convenience, $\phi_m(y)$ is usually chosen to be the mode of the given structure $\bar{f}(y)$.

However, in the case of $|\Delta\epsilon_r(y)| << |\epsilon_r(y)|$, it is assumed that the eigenmodes are unchanged and thus the mode amplitudes $a_{pm}(z)$ in equation (F.12) reduces to $A_p(z)$. Then the task is to evaluate the change in the eigenvalue, i.e., the propagation constant ξ_p. It is assumed the new solution is in the form

$$E_p(y,z) \approx A_p(z)\bar{f}_p(y)e^{-j\bar{\xi}_p z} \tag{F.13}$$

Substituting equation (F.13) into the wave equation (F.11) yields

$$A_p(z)\frac{d^2\bar{f}_p}{dy^2}e^{-j\bar{\xi}_p z} + (\epsilon_r(y) + \Delta\epsilon_r(y))k_0^2\bar{f}_p(y) + \bar{f}_p(y)\frac{d^2}{dz^2}(A_p(z)e^{-j\bar{\xi}_p z}) = 0 \tag{F.14}$$

or

$$\begin{aligned} A_p(z)[\frac{d^2\bar{f}_p}{dy^2} + (k_0^2\bar{\epsilon}_r(y) - \bar{\xi}_p^2)\bar{f}_p(y)] \\ +k_0^2\Delta\epsilon_r(y)A_p(z)\bar{f}_p(y) - j2\bar{\xi}_p\frac{dA_p(z)}{dz}\bar{f}_p(y) \\ +\bar{f}_p(y)\frac{d^2A_p(z)}{dz^2} = 0 \end{aligned} \tag{F.15}$$

Notice the terms inside the square brackets corresponding to equation (F.15), the unperturbed waveguide equation, are equivalent to zero. Besides, consider $|\Delta\epsilon_r(y)| << |\epsilon_r(y)|$, the following approximation applies

$$\left|\bar{\xi}_p\frac{dA_p}{dz}\right| >> \left|\frac{d^2A_p}{dz^2}\right| \tag{F.16}$$

Therefore equation F.15 becomes

$$k_0^2\Delta\epsilon_r(y)A_p(z)\bar{f}_p(y) - j2\bar{\xi}_p\frac{dA_p(z)}{dz}\bar{f}_p(y) = 0 \tag{F.17}$$

or

$$\bar{f}_p(y)\frac{dA_p(z)}{dz} + j\frac{k_0^2}{2\bar{\xi}_p}\Delta\epsilon_r(y)\bar{f}_p(y)A_p(z) = 0 \tag{F.18}$$

Notice that (F.18) is an ordinary differential equation of $A_p(z)$ but parameterized in y. By multiply $\bar{f}_p^*(y)$ ('$*$' denotes complex conjugate) throughout equation (F.18) and integrate over $-\infty < y < \infty$, an average value of terms in y will be obtained, that is

$$\left(\int_{-\infty}^{\infty}\bar{f}_p(y)\bar{f}_p^*(y)\right)\frac{dA_p(z)}{dz} + j\frac{k_0^2}{2\bar{\xi}_p}\left(\int_{-\infty}^{\infty}\bar{f}_p(y)\Delta\epsilon_r(y)\bar{f}_p^*(y)\right)A_p(z) = 0 \tag{F.19}$$

or

$$\frac{dA_p(z)}{dz} + j\frac{k_0^2\Gamma_p}{2\bar{\xi}_p}A_p(z) = 0 \tag{F.20}$$

with

$$\Gamma_p = \frac{\int_{-\infty}^{\infty}\bar{f}_p(y)\Delta\epsilon_r(y)\bar{f}_p^*(y)dy}{\int_{-\infty}^{\infty}\bar{f}_p(y)\bar{f}_p^*(y)dy} \tag{F.21}$$

which is constant for each particular mode. The solution for equation (F.20) can be readily obtained

$$A_p(z) = ae^{-j\Delta\xi_p z} \tag{F.22}$$

and

$$\Delta\xi_p = \frac{k_0^2\Gamma_p}{2\bar{\xi}_p} \tag{F.23}$$

Substituting equation (F.23) back to equation (F.13) yields

$$E_p(y,z) \approx a\bar{f}_p(y)e^{-j(\bar{\xi}_p+\Delta\xi_p)z} \tag{F.24}$$

which indicates that the new propagation constant $\xi_p = \bar{\xi}_p + \Delta\xi_p$.

Appendix G

Figure of Merit M_2 in Acoustooptic Interaction, [32]

For a chosen material and AO device design, the amplitude of the perturbation of the refractive index Δn is determined by the loaded acoustic power. From equation (4.1) presented in Chapter 4, the index changing is related to the induced strain by photoelastic constant, i.e.

$$\Delta n = -\frac{n^3 p}{2} S \tag{G.1}$$

where p is phosoelastic constant of material and S is strain. In equation (G.1) the suffix notation is omitted for simplicity.

The power intensity carried by an elastic wave is

$$\frac{P_a}{\text{Vol}} = \frac{1}{2} c S^2 \tag{G.2}$$

with c being the stiffness constant of material and P_a/Vol being the acoustic power per unit volume. Since the acoustic power flux density, which is referred as acoustic intensity, is of more interest, it is expressed as

$$I_a = v \frac{P_a}{\text{Vol}} \tag{G.3}$$

Combining equation (G.1)$\sim$(G.3) yields

$$I_a = \frac{1}{2} \rho v^3 S^2 \tag{G.4}$$

or

$$s = \sqrt{\frac{2I_a}{\rho v^3}} \tag{G.5}$$

In deriving equation (G.4), the relation of $v^2 = c/\rho$ (Appendix A) has been used.

Substituting equation (G.5) into the AO diffraction efficiency of equation (3.34) and (3.45) in Chapter 3 yields

$$\eta = sin^2(\frac{\pi L}{\sqrt{2}\lambda_0 cos\theta}\sqrt{\frac{n^6 p^2}{\rho v^3} I_a}) \tag{G.6}$$

If defining a new constant M_2, i.e.

$$M_2 \equiv \frac{n^6 p^2}{\rho v^3} \tag{G.7}$$

equation (G.6) thus becomes

$$\eta = sin^2(\frac{\pi L}{\sqrt{2}\lambda_0 cos\theta}\sqrt{M_2 I_a}) \tag{G.8}$$

The figure of merit M_2 is a material constant which determines the inherent efficiency of diffraction, regardless of interaction geometry, and is called the figure of merit, [134].

In bulk AO device, the power carried in an acoustic beam is expressed in the form P_a/vA with $A = LH$ being the cross-section area and L is the width and H is the thickness of the acoustic beam. The diffraction efficiency (G.6) can thus be rewritten

$$\eta = sin^2(\frac{\pi}{\lambda_0 cos\theta}\sqrt{\frac{M_2 P_a L}{2H}}) \tag{G.9}$$

Appendix H

Publications

- Q. Meng, F. Causa, J. Sarma, S. Dupont, J.-C. Kastelik, V. Zhang, Modelling and design of surface acoustic waves in optical-quality multi-layer GaN structures, Semiconductor and Integrated Optoelectronics Conference, SIOE'2007, Cardiff, Wales, 3-4 April 2007

- S. Dupont, J.-C. Kastelik, V. Zhang, F. Causa, Q. Meng, J. Sarma, Design of III-Nitride multi-layer structures for optical and surface acoustic wave interaction, Session: PA17, Acoustics'08, Paris (France), June 29th - July 4th 2008

- Q. Meng, F. Causa, J. Sarma, Computations for the Design of an Integrated Surface Acoustic Wave Controlled Semiconductor Optical Source, (TuA2) 8th International Conference on Numerical Simulation of Optoelectronic Devices, NUSOD '08, University of Nottingham, UK, 1st-5th Sept 2008

- Q.Meng, F.Causa and J.Sarma, Computations for the Design of an Integrated Surface Acoustic Wave Controlled Semiconductor Optical Source, Opt. Quan. Elec., 40(14), 2008

- Q.Meng, F.Causa and J.Sarma, Beam Deflection in an Integrated SAW-controlled Semiconductor Optical Source, Semiconductor and Integrated Optoelectronics Conference, SIOE'2009, Cardiff, Wales, 6-8 April 2009